A Framework for Computing the Stability of Human Motion

Victor Shia

Electrical Engineering and Computer Sciences
University of California at Berkeley

Technical Report No. UCB/EECS-2017-16
http://www2.eecs.berkeley.edu/Pubs/TechRpts/2017/EECS-2017-16.html

May 1, 2017

A Framework for Computing the Stability of Human Motion

by

Victor Andrew Shia

A dissertation submitted in partial satisfaction of the

requirements for the degree of

Doctor of Philosophy

in

Engineering - Electrical Engineering and Computer Sciences

in the

Graduate Division

of the

University of California, Berkeley

Committee in charge:

Professor Ruzena Bajcsy, Chair
Professor Claire Jennifer Tomlin
Professor John Karl Hedrick

Spring 2016

A Framework for Computing the Stability of Human Motion

Abstract

A Framework for Computing the Stability of Human Motion

by

Victor Andrew Shia

Doctor of Philosophy in Engineering - Electrical Engineering and Computer Sciences

University of California, Berkeley

Professor Ruzena Bajcsy, Chair

Every year, 2.5 million people visit the emergency department accounting for $34 billion in hospital visits, stays and treatment. Financial considerations aside, falling once results in the fear of falling further increasing the likelihood of falling. For the past few decades, much work has gone into identifying those likely of falling or those who are stable by determining features that distinguish fallers from non-fallers. The holy grail of such an identification scheme would inform how much perturbation the subject can reject, which is also known as the basin of stability. The more perturbation that can be rejected, the larger the basin of stability is and the more stable the individual is. However, determining this basin of stability experimentally is an impractical task. Rather than performing perturbation experiments, recent advances in control theory and reachability analysis allow us to compute this basin of stability in simulation.

In this thesis, we present a personalized and automated framework for computing the basin of stability for human motion. To do this, we first develop a tool to compute the basin of stability for dynamical systems and apply this to human motion. The utility of this framework is illustrated on the Sit-to-Stand task, though it can handle more general motions such as gait. The framework is broken down into three components. First, a representative hybrid model is chosen for the standing motion. Second, a controller is constructed to track the motion using optimal control and PD control. Third, using recent advances in hybrid occupation measures, an outer-approximation of the basin of stability is computed. We study the Sit-to-Stand action of 15 subjects (10 young and 5 older) and the computed basin of stability can differentiate between less and more stable Sit-to-Stand strategies. The contributions are the first steps towards developing a numerical method for determining the basin of stability of human motion.

to my parents: my father, who passed away early in my graduate school program and was not able to see finish or get married, and my mother, who faithfully raised me and my two younger sisters.

Contents

Contents **ii**

List of Figures **iv**

List of Tables **vi**

1 Introduction **1**
1.1 State of the Art in Stability Analysis for Sit-to-Stand 4
1.2 Dynamical Systems Perspective - State of the Art 7
1.3 Contribution 10

2 Framework **11**
2.1 Preliminaries 12
2.2 Conceptual Framework 13
2.3 Implementable Framework for STS 21
2.4 Summary 27

3 Computational Tools for Stability **29**
3.1 Introduction 30
3.2 Preliminaries 30
3.3 Infinite Dimensional Linear Program 35
3.4 Numerical Implementation 41
3.5 Implementation and Examples 47
3.6 Conclusion 56

4 Experiment **57**
4.1 Experiments 58
4.2 STS Data 64
4.3 Results using an existing stability metric 67
4.4 Reachability results for IPM 74
4.5 Reachability results for DPM 83

5 Conclusion **94**

5.1 Conclusion 95
5.2 Future Work 96
5.3 Concluding Remarks 100

Bibliography **101**

List of Figures

1.1 Population of the Elderly over Time. 2
1.2 Unintentional Death by Falls among Adults over the Age of 65. 3
1.3 Sit-to-Stand Segmentation 4
1.4 Single Inverted Pendulum Model 5
1.5 Theoretical Basin of Stability for Single Inverted Pendulum 6
1.6 Pictorial Hybrid Systems for STS 8
1.7 An example of the BOS of an inverted pendulum swing-up controller 9

2.1 Conceptual Framework 12
2.2 Phases of Sit to Stand 14
2.3 Hybrid System Definition 15
2.4 Implementable Framework 21
2.5 Sit to Stand models 22
2.6 Conceptual and Implementable Framework 28

3.1 Pictorial view of occupation measures on a single trajectory for a system *without* input. 33
3.2 Pictorial view of initial, average occupation and final measures for a system *without* input. 34
3.3 Pictorial View of Hybrid Occupation Measures. 37
3.4 Rimless wheel system 47
3.5 BRS of the Rimless Wheel 48
3.6 Vehicle Model 49
3.7 RS of Vehicle Under Different Inputs 50
3.8 Value of $w(x)$ levelset 51
3.9 Schematic of the compass gait walker. 52
3.10 BRS of Compass Gait Limit Cycle 54
3.11 Sampled BRS of Compass Gait Limit Cycle 55

4.1 Momentum-Transfer vs Quasi-Static STS Motions. Angular velocity of the ankle joint is negligible between the two motions and not shown. 59
4.2 Experimental Setup 61

4.3 Motion Capture Marker Placement 62
4.4 Force Plate Data with a single STS action. 66
4.5 ROSv for All Subjects 68
4.6 ROSa for All Subjects 69
4.7 ROSv and ROSa for a Young Subject 72
4.8 ROSv and ROSa for an Older Subject 73
4.9 BOS for IPM model of Young Subject 79
4.10 BOS for IPM model of Older Subject 81
4.11 BOS for DPM model of Young Subject 89
4.12 BOS for DPM model of Older Subject 91

5.1 Hybrid Model for STS 96
5.2 Hybrid Model for STS with Friction 99

List of Tables

1.1 Various STS Stability Methods 5

4.1 Comparison between STS strategies 60
4.2 Data for each individual 63
4.3 All STS motions and speeds collected 63
4.4 Filenames for STS Data 64
4.5 Force Plate Data Structure 64
4.6 Inertial Measurement Unit Data Structure 65
4.7 ROSv for each STS action 70
4.8 ROSa for each STS action 71
4.9 Median of Computed BOS of each STS action for IPM 74
4.10 Maximum of Computed BOS of each STS action for IPM 75
4.11 Median of simulated BOS of each STS action for IPM 76
4.12 Maximum of simulated BOS of each STS action for IPM 77
4.13 Median of Computed BOS of each STS action for DPM 83
4.14 Maximum of Computed BOS of each STS action for DPM 84
4.15 Median of simulated BOS of each STS action for DPM 85
4.16 Maximum of simulated BOS of each STS action for DPM 86
4.17 Summary of comparison of the various metrics for Slow vs Fast, Quasi-static vs Momentum-Transfer using the median values. 92
4.18 Comparison of ROSv and ROSa vs the proposed method for subject ID 7. Expected results shown in green; unexpected results shown in red. 92
4.19 Comparison of ROSv and ROSa vs the proposed method for subject ID 11. Expected results shown in green; unexpected results shown in red. 93

Acknowledgments

First and foremost, I would like to thank my advisor, Prof. Ruzena Bajcsy, for taking me on as a graduate student in her lab. She provided me the freedom to choose my own projects while encouraging me to pursue interesting and hard problems and providing just enough guidance when I needed it. In her lab, I was able to learn how to do research: both theoretical and experimental and never had to worry about funding. She was patient with many of my failures and frustrations, helping me to endure them.

I would especially like to thank Ram Vasudevan who, in many ways, was my second advisor. Though he was only 4 years my senior, he guided me my entire time in graduate school while he himself was trying to graduate, working as a post-doc and began his professorship. He asked many tough questions, demanded excellence and pushed me beyond what I thought was my limit. Yet he also encouraged me when I was questioning my own ability to do research and taught me how to persevere, how to be clear in presentation and writing, and how to conduct research. He gave me the initial idea for my masters and doctoral theses and I would not have finished without his guidance.

I would also like to thank the members of my qualifying exam committee, Claire Tomlin, Bob Full, and J. Karl Hedrick. The guidance they provided and the time preparing for the exam helped clarify the problems I focused on for this thesis.

I also thank many of the collaborators who have helped me during my time in graduate school: Robert Matthew, Gregorij Kurillo, Allen Yang, Katherine Driggs-Campbell, Aaron Bestick, Daniel Calderone, Mo Chen, Jaime Fisac, and Daniel Aranki. Much of the work that I've done resulted from discussions with Robert. We bounced ideas off each other throughout the years, shared frustrations, and, somehow through it all, were able to finish together.

I would also like to acknowledge the administrative staff in my lab: Jessica Gamble and Mary Stewart, both who have helped me tremendously with logistic and technical problems.

I'm forever grateful for my parent's loving support, allowing me to "chose" my own path and not forcing me to pursue their own dreams for me. This allowed me to grow into a person who loved to learn yet and not burn out in a tough academic environment. As much as I tried to avoid being like my father who was always very entrepreneurial and unafraid of failure, through this graduate program, I've found that I'm more like him than I expected.

I'm thankful to Edna Miao, my wife, who bore with me throughout the last 2 years of my program, patiently waiting for me to finish and being willing to go through this crazy thing called life together.

Finally, I would like to thank God, who saved me from my sins and who gave me an eternal purpose when He called me to follow him. My life trajectory has completely changed since then and I look forward to what He has in store for me in the future.

Chapter 1

Introduction

According to the United States Centers for Disease Control and Prevention (CDC), "each year, millions of older people - those 65 and older - fall." In fact, one out of three older people fall each year, but less than half inform their doctor. Furthermore, falling once doubles the likelihood of a repeat fall [1]. With the ever-growing population of elderly individuals over the age of 65 shown in Figure 1.1 and the increasing rate of fall-related fatalities shown in Figure 1.2, this is an ever increasing issue for the nation's population [2].

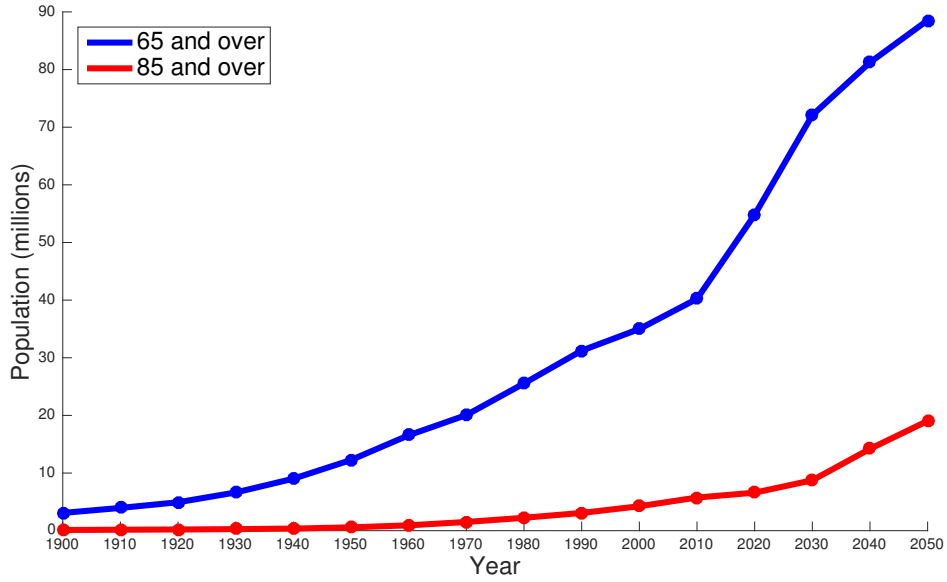

Figure 1.1: Population of the Elderly over Time.

In 2015, the CDC published the following statistics:

- Twenty percent of falls cause serious injuries such as broken bones or head trauma.
- Fall injuries account for 2.5 million emergency department visits annually.
- Over 700k patients annually are hospitalized due to a fall injury.
- Over 95% of hip fractures are caused by falling, usually by falling sideways.
- The annual cost of fall injuries is approximately $34 billion.

While most falls do not result in injuries, the fear of falling leading to a decrease in exercise, increasing the likelihood of falling and resulting in an unfortunate positive feedback cycle. Most falls are a combination of risks factors which include:

- Lower body weakness
- Medicine use
- Walking and balance difficulties
- Vision issues

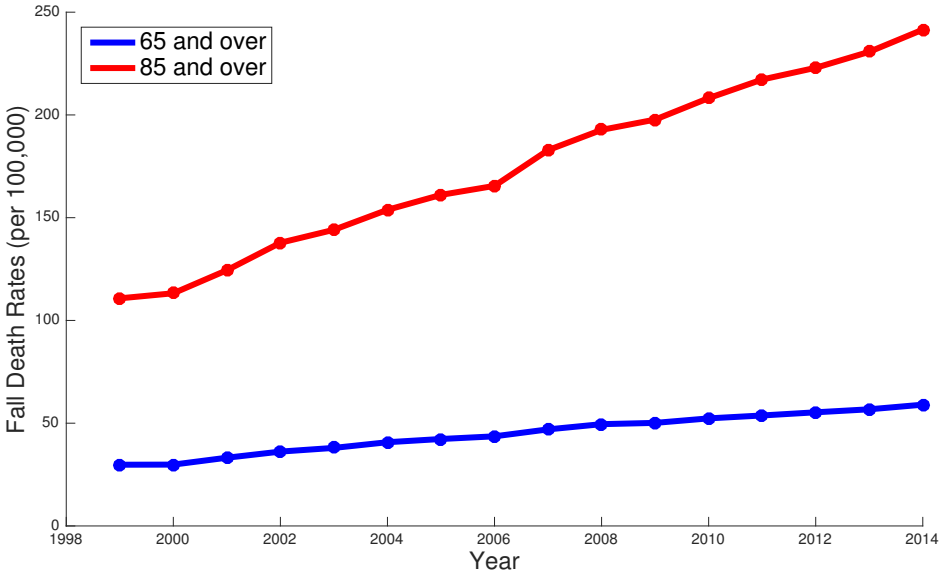

Figure 1.2: Unintentional Death by Falls among Adults over the Age of 65.

- Dizziness/Vertigo
- Foot pain
- Vitamin D deficiency
- Home hazards

To reduce the risk of falling, identification and early-treatment of those at-risk of falling is key. For the past two decades, much research has been conducted among the clinical and biomechanics communities to identify those likely for falling down. If at-risk individuals can be identified early, preventative measures such as medicine, environment change, physical therapy, strength training exercises, prosthesis or exoskeletons can be provided to reduce the risk of falls [3, 4]. In addition, targeted deployment could become feasible with the development of an automated test that identified those at risk while characterizing the specific deficiencies that increased their likelihood of falls. Two types of human motion commonly studied are Sit-to-Stand motions (STS) and gait. While the presented framework is general for all both motions, in this thesis we focus on Sit-to-Stand motions.

Sit-to-Stand is one of the most basic human motions and a precursor to many activities of daily living (ADL) tasks: tasks which the medical community has deemed essential for daily living. These tasks include walking, basic hygiene, bathing/showering, dressing, and self-feeding. According to Lord, et al., risk factors for falling during standing include: medicine use, previous stroke, reduced ability to rise from a chair, slow reaction time, poor vision, and impaired physical function[5]. Intervention to improve STS stability include reduction of medication, balance and gait training, strength training, walkers and exoskeletons [6, 7]. The STS motion can be segmented into two phases: a sitting portion and standing portion shown in Figure 1.3 [8] and it is hypothesized that falling occurs between the transition of these two phases [9].

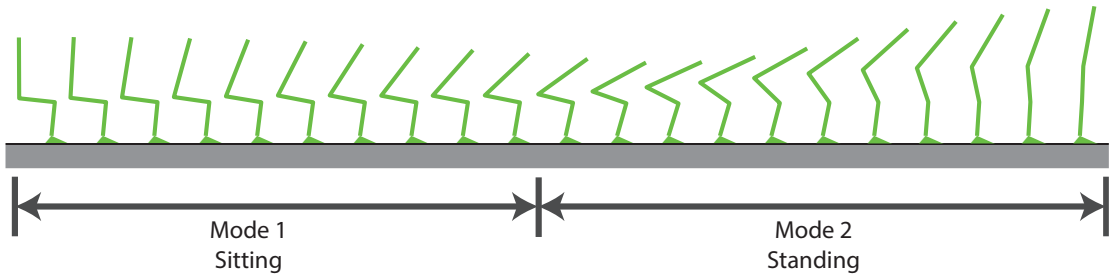

Figure 1.3: One type of sit-to-stand segmentation

Due to the large health, economic and societal impact of falling, many measures have been proposed and tested to identify individuals who are at risk of falling. Researchers have identified the measurement of the **basin of stability** (BOS) as the most direct way to characterize the likelihood of falling [10]. The **basin of stability** denotes the range possible of perturbations or disturbances that a subject can experience and still complete the desired motion. In fact, the calculation of an individual and motion-specific BOS has the benefit of identifying the specific deficiencies that lead to stumbles, which can both aid the individual and inform intervention selection. Unfortunately the computation of the BOS is challenging since it requires measuring the effect of arbitrary disturbances to a nonlinear system. For example, an empirical experiment would require exhaustive perturbation of an individual throughout a locomotor pattern, which is practically infeasible and potentially harmful. Due to the difficulty of computing the BOS, several methods have been proposed which transform a STS motion to a single feature and perform regression analysis to determine a patient's stability.

1.1 State of the Art in Stability Analysis for Sit-to-Stand

Due to the importance of STS maneuvers in maintaining quality of life, and the impossibility of testing all possible perturbations, a variety of methods to characterize an individual's likelihood of falling while performing STS have been proposed. These methods are summarized in Table 1.1.

An example of the model-based method to determine stability was developed in 1997 by Pai et al and is shown in Figure 1.5 [16]. The position (with respect to the heel) and forward velocity of the center of mass (COM)[1] is recorded when the subject stands up from the chair. If the subject's placement on the graph lies within the gray zone, it is theoretically possible to stand up successfully given the subject's momentum and muscle strength limits.

[1]Position is normalized to 1 unit by the subject's foot length. Forward velocity is normalized to 1 unit/second pendulum length per second.

Methods	Summary	References
BERG Balance Test	A battery of functional tests with a single number that determines the likelihood of falling.	[11]
Five Times Sit-to-Stand	Relates amount of time to stand up and sit down 5 times to likelihood of falling.	[12]
Stops Walking When Talking	Relates the amount of attention a person requires to perform an action with a likelihood of falling.	[13]
Timed Up & Go	Correlates a likelihood of falling with the the amount of time it takes to stand up.	[14, 15]
Model based methods	Uses a single inverted pendulum to determine the set of feasible initial positions or positions and velocities that can lead to standing up.	[16, 17, 18, 8, 19, 20]

Table 1.1: Various STS Stability Methods

However, if the subject's placement on the graph lies outside the gray zone, he either will either need to step forward or backward to avoid falling. The gray region is known as the feasible stability region.

These methods generally summarize STS motions using a single feature and perform versions of regression analysis to estimate a patient's stability. In doing so, they forfeit the ability to characterize an individual's specific deficiencies that limit their STS ability. More troublingly, according to several studies, the ability of these clinical tests to distinguish between stable and unstable patients is unclear [13, 21, 22, 23, 24].

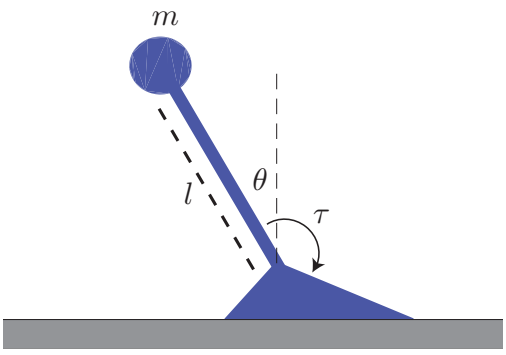

Figure 1.4: Single Inverted Pendulum Model

This leads us to determine that the search for an informative sit to stand stability metric is still an open question.

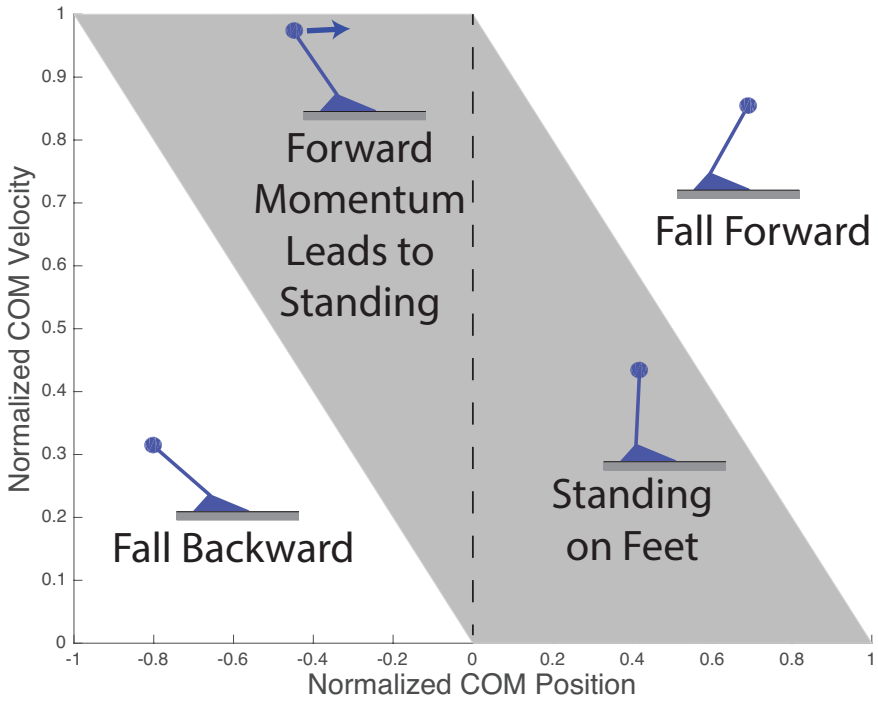

Figure 1.5: Theoretical basin of stability for single inverted pendulum. On the X-axis is the normalized center of mass (COM) position. On the Y-axis is the normalized COM forward velocity. The gray region denotes the theoretically possible BOS. If the subject's COM begins in the gray region, then it as long as the subject has enough strength, he should be able to stand up and prevent himself from falling forward or backward.

1.2 Dynamical Systems Perspective - State of the Art

The dynamical systems community has long considered the problem of computing the stability or BOS to verify the correct operation of a system. To begin, we describe continuous dynamical systems then move to hybrid dynamical systems, which this thesis will be based on.

Continuous dynamical systems are systems whose evolution through time t can be described via a differential equation:

$$\dot{x}(t) = f(t, x, u) \tag{1.1}$$

where x is the state of the system and u is an input to the system.

When modeled via a differential equation, the performance of a dynamical system can be predicted and robustness guarantees can be provided. In particular, engineers have long sought to understand the behavior of dynamical systems after arbitrary perturbation and realized that direct simulation provided only limited insight. To address this issue, the controls community has developed numerous methods to determine stability of dynamical systems. In the 1960s, Lyapunov theory emerged as the prominent analytical method to determine the stability of systems [25]. If a function that satisfies the Lyapunov criteria can be found for a system, the system is said to be Lyapunov stable. In addition, further criteria can guarantee that the system is either asymptotically or exponentially stable locally or globally. This can be used to find a system's basin of stability, which is traditionally known as the system's region of attraction or reachable set.

Methods to compute the BOS for continuous systems include Lyapunov-based techniques [26], support functions [27, 28], Ellipsoidal methods [29, 30], barrier certificates [31], Hamilton-Jacobi based methods [32, 33], and occupation measures [34, 35]. Lyapunov-based methods search for functions whose sub-level sets satisfy Lyapunov's criterion [25]. The construction of such a Lyapunov function is possible for polynomial dynamical systems using semidefinite programming [36, 26, 37], but requires solving a bilinear optimization problem which can be challenging to apply in practice. Support functions describe the target set using an intersection of hyper-planes. By propagating these hyper-planes through the dynamics, the intersection of the hyper-planes through time results in the BOS. Ellipsoidal methods cover the inside/outside of the target set using an union/intersection of ellipses. By propagating these ellipses through the dynamics, the union/intersection of the hyper-planes through time results in the inner or outer-approximation of the BOS. Barrier methods search for functions which can separate a safe region from unsafe region. Hamilton-Jacobi based methods discretize the state space and use dynamic programming on a discretized nonlinear partial differential equation to determine the set of states that belong to a BOS. Though this method is able to tractably compute the BOS for dynamical systems with special structure [38], due to the curse of dimensionality, it is only able to accurately compute the BOS for general systems with less than 5 states. Occupation measures model the target set using probability densities and propagate these densities in time via Liouville's equation. While

occupation measures also suffer from the curse of dimensionality, it has been able to compute an outer-approximation to the BOS for systems with up to 8 states.

To deal with systems with discrete modes or phases and discrete transitions, such as phases and transitions in STS or gait, the field of hybrid systems emerged in the 1990s [39, 40]. Hybrid dynamical systems are systems whose evolution through time t can be described via distinct differential equations depending on the discrete state:

$$\dot{x}(t) = f_j(t, x, u) \tag{1.2}$$

where x is the state space of the system, u is the continuous input to the system, and j is the discrete state of the system[2,3]. Examples of hybrid systems include: HVAC and energy systems [41], air traffic control [42, 43], vehicle dynamics [44, 45, 46], and gait [47, 48].

A hybrid model of the sit to stand behavior is shown in Figure 1.6 where mode 1 describes the dynamics when the subject is sitting and mode 2 when the subject is standing. The point of transition between two modes is called the guard. For STS motion, the guard is the point when the subject changes from sitting to standing.

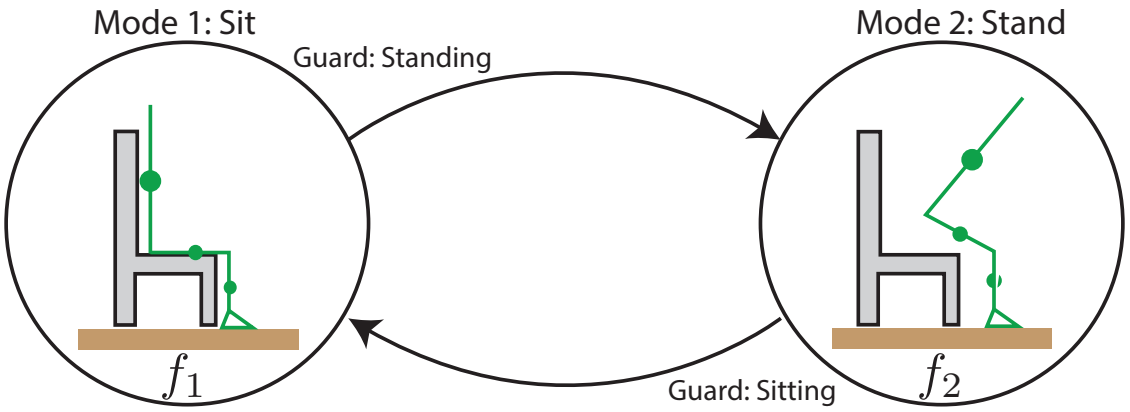

Figure 1.6: Pictorial Hybrid Systems for STS

Unfortunately, stability results from continuous dynamical systems do not easily extend to hybrid dynamical systems [49]. For example, a hybrid system, consisting of two independently stable modes, when combined may not be stable. As such, a new field studying the stability of hybrid systems emerged [50, 51, 52, 53, 54, 55, 56, 57, 58, 59]. In addition, extensions to the computation of BOS of hybrid systems exist for Lyapunov functions [60, 61, 37, 62, 63], support functions [64], ellipsoidal methods [65], barrier certificates [66] and Hamilton-Jacobi based-methods [43, 67].

Recently, we have developed a method based on occupation measures to analytically compute the BOS for polynomial dynamical systems and successfully applied it to synthesize safe robotic motion for systems with up to eight states [34, 68]. We extend this method to

[2]Note that a hybrid dynamical system with one mode is equivalent to a continuous dynamical system.
[3]Hybrid systems will be defined mathematically in Chapter 2.

study the BOS for hybrid polynomial dynamical systems in [69]. This method, which relies on convex optimization and is described in Chapter 3, is able to tractably outer approximate the BOS of a system without relying upon exhaustive perturbative experiments or simulation. For example, the computed BOS of a single inverted pendulum with a swing-up PD controller is shown in Figure 1.7.

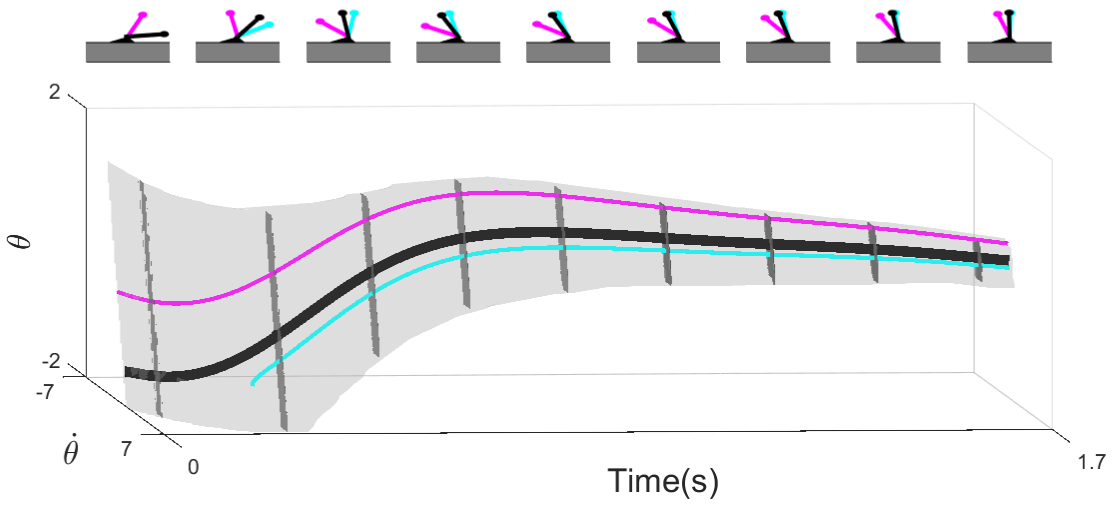

Figure 1.7: An example of the BOS of an inverted pendulum swing-up controller. The top row illustrates a nominal (black) and perturbed (magenta and cyan) swing up trajectory for the inverted pendulum. The bottom row illustrates the BOS of the nominal controller (gray), the nominal trajectory (black), and the perturbed trajectory (orange) in the configuration space of the inverted pendulum. Notice that despite being perturbed at 0 and 0.16 seconds, the magenta and cyan trajectories are able to arrive at the up-right configuration since it remains inside of the basin of stability of the nominal trajectory. The goal of this paper is to compute this basin of stability of an individual's specific locomotion from observations.

1.3 Contribution

While the work here is general to study any locomotor motion, as a proof of concept, we demonstrate its utility on the STS motion. The contributions of this thesis are below:

- In Chapter 2, we propose a framework to compute the basin of stability for one's motion. First, we present the conceptual framework utilizing optimal control, feedback control synthesis, and occupation measures. Second, we present a specific implementation of the framework utilizing collocation, LQR, and a modification of occupation measures.

- In Chapter 3, we develop an analytical method called occupation measures to compute the backward reachable set (BRS) or basin of stability (BOS) of a dynamical system. We begin with developing the intuition and theory of using probability densities to propagate dynamics via Liouville's equation resulting in an infinite dimensional *linear* program. We then show how to relax this infinite dimensional program to a finite dimensional semi-definite program, amenable to convex optimization algorithms. Lastly, we show its utility on 3 systems: a rimless wheel walker, a vehicle with a hybrid tire friction model, and a compass gait walker.

- In Chapter 4, we describe the experiment protocol to collect data on various Sit-to-Stand actions for 15 subjects: 10 subjects between the ages of 20-50 and 5 subjects over the age of 50. This dataset consists of motion capture data (accurate to 1mm), kinect skeletal data, force platform data (with linear and rotational forces in 3D), and accelerometry data of the lower leg, upper leg and upper body.

- Finally, we analyze the BOS of various STS actions and show that the BOS of stable actions are larger than not-as-stable actions. Comparing this to the only other model-based stability method for STS, we show that the proposed method better distinguishes stable from not-as-stable actions.

- We conclude with many ideas for future work to bring the proposed method into greater acceptance by both the biomechanics and clinical communities.

By providing computational tools to provide a quantitative approach to studying one's basin of stability, we hope to improve the work of identifying and treating patients with a high-risk of falling, enabling them to have a better quality of life.

Chapter 2

Framework

In this chapter, we describe the framework used to compute the basin of stability for motion. First, we describe hybrid systems and illustrate how locomotion can be modeled using this approach. Next, we present the conceptual framework depicted in Figure 2.1. We conclude with the implementation of the framework.

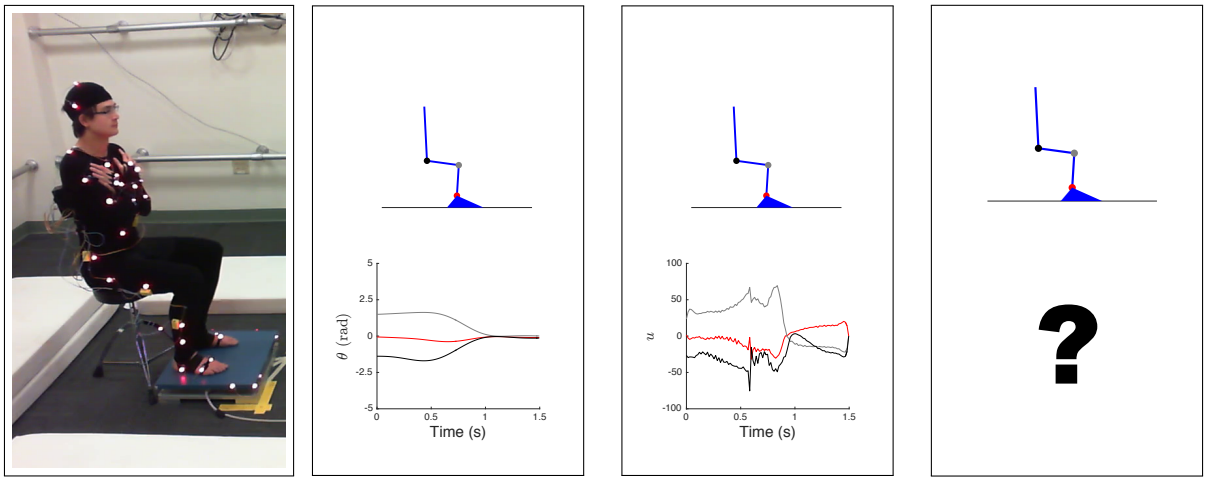

Data Collection Modeling Input ID Compute BOS

Figure 2.1: Conceptual Framework

2.1 Preliminaries

Given an element $x \in \mathbb{R}^n$, let $[x]_i$ denote the (i)–th component of x. We use the same convention for elements belonging to any multidimensional vector space. Let $\mathbb{N}$ denote the non-negative integers, and $\mathbb{N}^n_k$ refer to those $\alpha \in \mathbb{N}^n$ with $|\alpha|_1 = \sum_{i=1}^n [\alpha]_i \leq k$. Let $\mathbb{R}[y]$ denote the ring of real polynomials in the variable y. For a compact set $X \subset \mathbb{R}^n$, let $\mathcal{M}(X)$ denote the space of signed Radon measures supported on X. The elements of $\mathcal{M}(X)$ can be identified with linear functionals acting on the space of continuous functions $C(X)$, that is, as elements of the dual space $C(X)'$ [70, Corollary 7.18]. The duality pairing of a measure $\mu \in \mathcal{M}(X)$ on a test function $v \in C(X)$ is:

$$\langle \mu, v \rangle = \int_X v(x) d\mu(x). \tag{2.1}$$

Let $C^1(X, \mathbb{R})$ be the space of continuously differentiable functions over X to $\mathbb{R}$; $L^2(X, \mathbb{R})$ be the space of square integrable functions over X to $\mathbb{R}$ such that $\int_X \|f(x)\|^2 dx < \infty$; and $\mathbb{R}_d[x]$ be the set of polynomials in X with maximum total degree d. In addition, let $\text{spt}(\mu)$ denote the support of a measure μ and λ_n denote the Lebesgue measure on $\mathbb{R}^n$. Given $n \in \mathbb{N}$ and $D \subset \mathbb{R}^n$, ∂D denotes the boundary of D. Recall that given a collection of sets $\{S_\alpha\}_{\alpha \in \mathcal{A}}$,

Algorithm 1 Computing the Reachable Set for STS

1: Given: observations $x_{\text{obs}}(t)$ of the motion
2: Choose a model for the motion.
3: Run optimal control to find $u_{\text{obs}}(t)$, the input that tracks the motion.
4: Construct controller to track $x_{\text{obs}}(t)$.
5: Compute the backwards reachable set of the controller.

the *disjoint union* of this collection is $\coprod_{\alpha\in\mathcal{A}} S_\alpha = \bigcup_{\alpha\in\mathcal{A}} S_\alpha \times \{\alpha\}$. Throughout the thesis we abuse notation and say that given $\bar{\alpha} \in \mathcal{A}$ and $x \in S_{\bar{\alpha}}$, then $x \in \coprod_{\alpha\in\mathcal{A}} S_\alpha$, even though we should write $\iota_{\bar{\alpha}}(x) \in \coprod_{\alpha\in\mathcal{A}} S_\alpha$, where $\iota_{\bar{\alpha}} \colon S_{\bar{\alpha}} \to \coprod_{\alpha\in\mathcal{A}} S_\alpha$ is the *canonical identification* $\iota_{\bar{\alpha}}(x) = (x, \bar{\alpha})$.

2.2 Conceptual Framework

This section presents the framework to compute the BOS of an individual's locomotor pattern given observations. This section is intended to provide a high-level overview of the framework composed of modular pieces, each which could be an entire PhD thesis in of themselves. The approach is summarized in Algorithm 1[1]. These steps are described abstractly at first in this section to ensure straightforward generalization to arbitrary locomotor patterns.

Individualized Hybrid Model

The first component of the framework is to construct a representative model of the desired action. There are various levels of individualized models ranging from simple models, known as template models, to complex models, know as anchor models, each with different use cases [71]. Template models are simple models that track limited and relevant features that are used to explain the action. An example of a template model for STS is an inverted pendulum with the mass placed at the subject's center of mass [16]. Anchor models are complex model which describe the real action with as much detail as possible. An example of an anchor model for the human body can be found in OpenSIM [72]. For example, OpenSIM has been used to find the muscle excitations for gait. Due to their complexity, current stability tools are unable to analyze anchor models. For this work, we use template models for modeling STS.

Therefore, we consider control affine systems which is a special case of the dynamical

[1]The framework MATLAB code is available at `www.w3id.org/people/vshia/jrsi/`

equations defined as:

$$\begin{aligned} \dot{x}(t) &= f(t,x) + g(t,x)u(t,x) \\ x &\in [\underline{x}, \overline{x}] \subset \mathbb{R}^n \\ u &\in [\underline{u}, \overline{u}] \subset \mathbb{R}^m \end{aligned} \tag{2.2}$$

where $X = [\underline{x}, \overline{x}] \subset \mathbb{R}^n$ represents the state space of the model, $f \in C^1([0,T] \times \mathbb{R}^n, \mathbb{R}^n)$ and $g \in C^1([0,T] \times \mathbb{R}^n, \mathbb{R}^m)$ describe how the input $u \in L^2([0,T] \times \mathbb{R}^n, \mathbb{R}^m)$ affect the dynamics and $\underline{u}, \overline{u} \in \mathbb{R}^m$ represent input bounds. As each individual is different, $\underline{x}$, $\overline{x}$, $\underline{u}$ and $\overline{u}$ are distinct for each individual and must be identified as described in further detail in Section 4.1. While the dynamics vary due to individual specific parameters of the model (e.g. mass, limb length, moment of inertia, etc.), we refer to the dynamics simply as f and g for brevity.

Many actions such as STS undergo various phases also known as modes. Since each phase contain different physical constraints, the range of possible actions may change in each phase. These phases and transitions can be modeled using the hybrid system construction allowing these actions to be analyzed with the available methods in control theory. Sit to stand up can be described with 2 modes: mode 1 when the subject is sitting on the chair and mode 2 when the subject is off the chair, shown in Figure 2.2 [8]. These modes can be described using a directed graph with each mode represented by a vertex of the graph and each mode containing a vector field governing the evolution of trajectories in that mode.

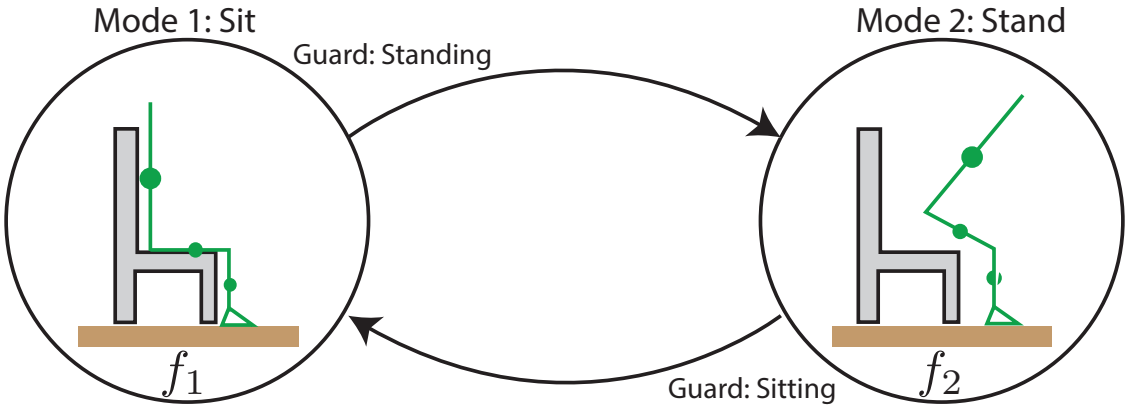

Figure 2.2: Phases of Sit to Stand

Here we formalize the notion of a hybrid system with control affine dynamics. First, let $h_{X_{j_i}}, h_{U_i}, h_{(j',j)} \in \mathbb{R}[x]$ be polynomials which describe the state space domain, input domain, and switching surface, respectively.

Autonomous Hybrid System

Definition 1: *A* controlled autonomous hybrid system *is a tuple* $\mathcal{H} = (V, E, \mathcal{D}, U, \mathcal{F}, \mathcal{S}, \mathcal{R})$ *s where:*

- *V is a finite set indexing the discrete states of $\mathcal{H}$;*

- $E \subset V \times V$ *is a set of edges, forming a directed graph structure over* V*;*
- $\mathcal{D} = \coprod_{j \in V} X_j$ *is a disjoint union of domains, where* $X_j = \left\{x \in \mathbb{R}^{n_j} \mid h_{X_{j_i}}(x) \geq 0, h_{X_{j_i}} \in \mathbb{R}[x], \forall i = \{1, \ldots, n_{X_j}\}\right\}$ *is a compact subset where* $n_{X_j} \in \mathbb{N}$*;*
- $U = \{u \in \mathbb{R}^m \mid h_{U_i}(u) \geq 0, h_{U_i} \in \mathbb{R}[u], \forall i \in \{1, \ldots, n_U\}\}$ *is a compact, convex subset which describes the range space of the control inputs where* $m \in \mathbb{N}$*;*
- $\mathcal{F} = \{(f_j, g_j)\}_{j \in V}$ *is a set of control affine systems, where* $f_j \colon \mathbb{R} \times X_j \to \mathbb{R}^{n_j}$*,* $g_j \colon \mathbb{R} \times X_j \to \mathbb{R}^{n_j \times m}$*, for* $t \in \mathbb{R}, x \in X_j$*, and* $u \in U$*,* $f_j(t, x) + g_j(t, x)u$ *is a tangent vector on* X_j *at* x*, and* $f, g \in \mathbb{R}[t, x]$*;*
- $\mathcal{S} = \coprod_{e \in E} S_e$ *is a disjoint union of the guards, where each* $S_{(j',j)} = \left\{x \in \partial X_j \mid h_{(j',j)_i}(x) = 0, h_{(j',j)_i} \in \mathbb{R}[x], \forall i = \{1, \ldots, n_{(j',j)}\}\right\}$ *is a compact, co-dimension* 1 *guard that defines a transition from domain* $j \in V$ *to domain* $j' \in V$ *and* $S_{(j',j)} \cap S_{(k',j)} = \emptyset$*,* $\forall (j', j), (k', j) \in E$ *when* $k' \neq j'$*;*
- $\mathcal{R} = \{R_e\}_{e \in E}$ *is a set of reset maps, where each* $R_{(j',j)} \colon S_{(j',j)} \to X_{j'}$ *defines the transition from guard* $S_{(j',j)}$ *to* $X_{j'}$*,* $R_{(j',j)} \in \mathbb{R}[x]$ *where* $x \in X_j$*, and* $R_{(j',j)}$ *is an injective, continuously differentiable function whose Jacobian is nonzero for every* $x \in S_{(j',j)}$*.*

Note that X_j and U are the 0 super-levelsets of polynomial functions $h_{X_{j_i}}$ and h_{U_i}. Similarly, $\mathcal{S}$ is the 0-levelset of the polynomial functions $h_{(j',j)}$. These sets are also called semi-algebraic sets. For convenience, we refer to controlled hybrid systems as just hybrid systems.

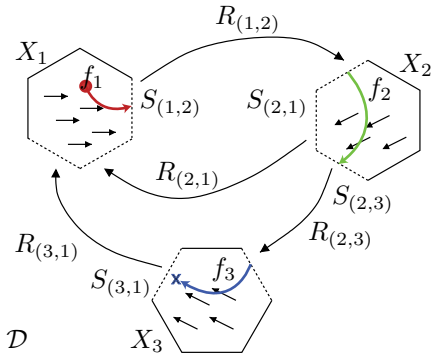

Figure 2.3: Hybrid System Definition

Next, we define an *execution* of a hybrid system via construction in Algorithm 2. This definition agrees with the traditional intuition about executions of hybrid systems, which describes an execution as evolving as a dynamical system until a guard is reached, at which point a discrete transition occurs to a new domain using a reset map, and evolution continues again as a dynamical system.

Hybrid systems can suffer from Zeno executions, i.e. executions that undergo an infinite number of discrete transitions in a finite amount of time. Since the state of the trajectory after the Zeno occurs maybe undefined, we do not consider hybrid systems with Zeno executions:

Assumption 1: *$\mathcal{H}$ has no Zeno execution.*

Algorithm 2 Execution of Hybrid System $\mathcal{H}$

Require: $t = 0$, $j \in V$, $(x_0, j) \in \mathcal{D}$, and $u : \mathbb{R} \to U$ Lebesgue measurable.

Set $x(0) = x_0$.
loop
  Let $\gamma\colon I \to X_j$ be an absolutely continuous function[a] such that:
    1. $\dot{\gamma}(s) = f_j(s, \gamma(s)) + g_j(s, \gamma(s))u(s)$ for almost every $s \in I$ with respect to the Lebesgue measure on $I \subset [0, \infty]$,
    2. $\gamma(t) = x(t)$, and
    3. for any other $\tilde{\gamma}\colon \tilde{I} \to X_j$ satisfying (i) and (ii) $\tilde{I} \subset I$.
  Let $t' = \sup I$ and $x(s) = \gamma(s)$ for each $s \in [t, t')$[b].
  if $t' = \infty$, **or** $\nexists (j', j) \in E$ such that $\gamma(t') \in S_{(j',j)}$ **then**
    Stop.
  end if
  Let $(j', j) \in E$ be such that $\gamma(t') \in S_{(j',j)}$.
  Set $x(t') = R_{(j',j)}(\gamma(t'))$, $t = t'$, and $j = j'$.
end loop

[a] Note that the existence of a curve satisfying conditions (i),(ii), and (iii) follows from [73, Theorem 10.1.4]

[b] Note if $t' < \infty$, then $\gamma(t') \in \partial X_j$. [73, Theorem 10.1.12]

Figure 2.3 shows an example hybrid system that:

1. starts with the red circle in X_1 and follows the red trajectory arriving at $S_{(1,2)}$
2. undergoes reset $R_{(1,2)}$ to X_2 and follows the green trajectory arriving at $S_{(2,3)}$
3. undergoes reset $R_{(2,3)}$ to X_3 and follows the blue trajectory until final time T.

Collecting Observations

After selecting a model, high dimensional observations of the action to analyze are collected from different sources ranging from motion capture [74, 75] to the Kinect [76]. These obser-

vations are then reduced to the features required by the model. The domain bounds are the minimum and maximum observed values from the data.

Identifying an Input from Observations

After selecting a model, the input, $u_{\text{obs}} : [0, T] \to \mathbb{R}^m$ that generates the given observations must be constructed. There are two methods for determining the input for the observed motion: inverse dynamics and optimal control.

Inverse dynamics is the simplest method to determine input forces to a dynamical system. Inverse dynamics uses the observed variables $x_{\text{obs}} : [0, T] \to X$ to estimate $\dot{x}_{\text{obs}} : [0, T] \to \mathbb{R}^n$. For continuous systems, with a known $(x_{\text{obs}}(t), \dot{x}_{\text{obs}}(t))$, $u_{\text{obs}}(t)$ can be defined as:

$$u_{\text{obs}}(t) = g^{\dagger}(t, x_{\text{obs}}(t)) \left(\dot{x}_{\text{obs}}(t) - f(t, x_{\text{obs}}(t))\right) \tag{2.3}$$

where $g^{\dagger}$ is the Moore-Penrose inverse of g. For hybrid systems, this method requires us to know which mode the subject is in for all time.

Optimal control calculates $u_{\text{obs}}(t)$ via optimization. For continuous systems, the optimization can be written as:

$$\begin{aligned} \inf_{u_{\text{obs}} \in L^2([0,T],\mathbb{R}^m)} \quad & \int_0^T \|x(t) - x_{\text{obs}}(t)\|_2^2 dt && \\ \text{s.t.} \quad & \dot{x}(t) = f(t, x) + g(t, x) u_{\text{obs}}(t) && \forall t \in [0, T] \\ & x(t) \in X && \forall t \in [0, T] \\ & u_{obs}(t) \in [\underline{u}, \overline{u}] && \forall t \in [0, T] \end{aligned} \tag{2.4}$$

The solution to this problem is a feedforward open loop control input u_{obs} that minimizes the L^2 error between the state trajectory and the observed trajectory.

Inverse dynamics and optimal control theoretically return identical $u_{\text{obs}}(t)$. However, in practice, they do not. While inverse dynamics is computationally very fast, due to experimental error resulting from the differentiation in $x_{\text{obs}}(t)$, it often is dynamically inconsistent which means that forward integration of the dynamics with $u_{\text{obs}}(t)$ does not result in $x_{\text{obs}}(t)$. To address this issue, researchers have used a combination of least squares, filtering, and optimization [77, 72]. On the other hand, optimal control results in a dynamically consistent u_{obs} but requires running an optimization algorithm and as a result is slower. Many algorithms have been proposed to solve the optimal control problem from calculus of variations, dynamic programming, Pontryagin's minimum principle [78], and nonlinear programming [79]. Since the inverse kinematic solution is more susceptible to noise in $x_{\text{obs}}(t)$, we use optimal control to compute $u_{\text{obs}}(t)$, the nominal input generating $x_{\text{obs}}(t)$.

Due to the discrete transitions for hybrid systems, optimal control for hybrid systems does not extend naturally from continuous system optimal control. If the transition sequence and times are known, Equation 2.4 can independently be run each mode. If the transition

sequence is not known, algorithms such as [80, 81, 82] can be used. As there are many formulations for optimal control of hybrid systems, for this section, we simply assume that the switching sequence and transition times are known and Equation 2.4 is run for each mode to obtain $u_{\text{obs},j}(t)$, the optimal controller that tracks $x_{\text{obs}}(t)$ in mode j.

Feedback Controller Design

Neuroscientists, psychologists, motor control researchers and biomechanists have observed that the nominal trajectories followed by humans during locomotor patterns are robust to small perturbations [83, 84, 85, 86, 87]. This robustness which is conferred by some feedback about the nominal control input or goal but the specific strategy that endows such robustness remains unclear.

Flash and Hogan, for example, showed that subjects minimize the square of jerk during reaching tasks [83]. Liu and Todorov showed that for endpoint reaching tasks, subjects utilize a time-varying Proportional Derivative (PD) control to reach a specified endpoint [88]. For the lower body, Dingwell et al. tracked the evolution of step width and found that subjects tended to correct deviations with just a proportional controller [89, 90].

To imbue the nominal control input that is identified by the optimal control algorithm in Section 2.2 with this feedback robustness and to measure the BOS, the following assumptions are made:

Assumption 2: *For each distinct locomotion action, humans utilize a feedforward control law with corresponding feedback. To perform a different action, the subject switches control laws.*

Assumption 2 states that for a particular action, such as standing up slowly, the subject follows a combination of feedforward and feedback control laws. If the subject decides to stand up differently, the subject follows a different control law. If a specific control law is not able to take a subject to standing after perturbation, a subject must switch control laws. The inability to switch control laws fast enough during an unexpected disturbance correlates with a likelihood of falling [9].

Assumption 3: *While performing a specific action, the subject utilizes a PD feedback around a nominal trajectory, x_{obs}, to correct deviations in the trajectory.*

According to Assumption 3 the feedback control law is:

$$\begin{aligned} u_j(t,x) &= u_{\text{obs},j}(t) + K_j(x(t) - x_{\text{obs}}(t)) \\ &= u_{\text{obs},j}(t) + u_{cc,j}(t,x) \end{aligned} \tag{2.5}$$

where for each mode j, K_j is the controller gain acting on the states and observed states and $u_{cc,j}(t,x)$ represents the general form of the controller correcting for deviations in the nominal trajectory. Note, the method presented to estimate the BOS, which is described in Section 2.2, cope with more general nonlinear feedback control inputs; however, as described earlier, the existing literature suggests that humans apply only linear feedback [89, 90].

Of concern is that the feedback controller would enforce the desired trajectory too rigidly causing the system to oscillate about the desired trajectory. With small enough gains, this can be avoided. For example, consider the system in Figure 1.7. The two perturbed trajectories in magenta and cyan do not oscillate about the desired trajectory.

Assumption 4: *The torque limits are constant throughout the motion.*

As humans do not have the ability to apply arbitrary torque to any joint, torque limits $[\underline{u}, \overline{u}]$, which are individual-specific, are set to the minimum and maximum of u_{obs} generated from the optimal control. Assumption 4 results in an outer-approximation of the BOS as the maximum torque limit will not be applicable at every instance in time.

Computing the Basin of Stability

Given a model, input bounds, and feedback control input that tracks x_{obs}, the BOS can be formally defined as follows: *the BOS is the set of states as a function of time that can be driven by the feedback control input to a target configuration, $X_T \subset X$, by time T via the dynamical system $\mathcal{H}$.* The target set X_T in the case of STS corresponds to the set of states where the subject is standing. The optimization algorithm to compute the BOS is shown in D and describe in depth in Chapter 3.

$$
\begin{aligned}
d^\star = \inf_{\substack{w_j \in C^1(\mathbb{R}^n, \mathbb{R}^n) \\ v_j \in C^1([0,T]\times\mathbb{R}^n, \mathbb{R}^n) \\ p \in \mathbb{R}}} \quad & \sum_{j\in\mathcal{J}} \int_{X_j} w_j(x) d\lambda_{n_j}(x) && (D) \\
\text{s.t.} \quad & \frac{\partial v_j(t,x)}{\partial x}\left(f_j(t,x) + g_j(t,x)u_j(t,x)\right) \\
& \qquad + \frac{\partial v_j}{\partial t} \le 0 && \forall (t,x,j) \in [0,T]\times\mathcal{D} \\
& w_j(x) \ge v_j(0,x) + p + 1 && \forall (x,j) \in \mathcal{D}, \\
& w_j(x) \ge 0 && \forall (x,j) \in \mathcal{D} \\
& v_j(T,x) \ge -p && \forall (x,j) \in X_T \\
& v_j(t,x) \ge v_{j'}(t, R_{(j',j)}(x)) && \forall (t,(x,(j',j))) \in [0,T]\times\mathcal{S}
\end{aligned}
$$

where v, w are continuously differentiable polynomials.

To understand the relationship between the solution, w_j and v_j, to this optimization problem and the BOS notice that $w_j(x) \ge p$ and $v_j(0,x) \ge 0$ for points that belong in the BOS:

Theorem 1: *For every $j \in \mathcal{J}$, $\mathcal{X}_j \subset \{x_0 \in X_j | w_j(x) \ge 1\}$ for any feasible w_j of D.*

Proof. Consider a feasible (v, w) in D. Given any $(x_0, j_0) \in \mathcal{X}$, there exists a u such that $u(t) \in U$ for all $t \in [0,T]$ and $x(T) \in X_T$ where $x : [0,T] \to \mathcal{D}$ is generated via Algorithm 2. Let $\{\tau_i\}_{i=0}^n \subset [0,T]$ be the strictly monotonic and finite sequence of transition times of the

trajectory (which exists by Assumption 1) with $\tau_0 = 0$ and $\tau_n = T$ and $\{j_i\}_{i=0}^n \subset \mathcal{J}$ be the sequence of visited modes. Due to D's constraints:

$$\begin{aligned}
-p \leq v_{j_n}(T, x(T)) &= v_{j_{n-1}}(\tau_{n-1}, R_{(j_n, j_{n-1})}(x(\tau_{n-1})))+ \\
&\int_{\tau_{n-1}}^{\tau_n} \mathcal{L}_{j_n} v_{j_n}(t, x(t), u(t))dt \\
&\leq v_{j_{n-1}}(\tau_{n-1}^-, x(\tau_{n-1}^-)) \\
&= v_{j_{n-2}}(\tau_{n-2}, R_{(j_{n-1}, j_{n-2})}(x(\tau_{n-2})))+ \\
&\int_{\tau_{n-2}}^{\tau_{n-1}} \mathcal{L}_{j_{n-1}} v_{j_{n-1}}(t, x(t), u(t))dt \\
&... \\
&\leq v_{j_0}(0, x_0) \leq w_{j_0}(x_0) - p - 1,
\end{aligned}$$

which proves the first statement since (x_0, j_0) was arbitrary. The second result follows from a straightforward extension to [34, Theorem 3] □

Therefore, the $\bigcup_{j \in V}\{x \in X_j | v_j(0, x) \geq 0\}$ levelset represents the BOS of the system at time $t = 0$. Furthermore, the $\bigcup_{j \in V}\{(t, x) \in [0, T] \times X_j | v_j(t, x) \geq 0\}$ levelset represents the BOS of the system for all time. In Figure 1.7, for example, the light gray region denotes the $v(t, x) \geq 0$ level set with the dark gray region denoting different time slices of the $v(t, x) \geq 0$ level set. Formal proofs for this will be given in Chapter 3. After computing $w(x)$ and $v(t, x)$, points in the domain $[0, T] \times X$ that exceed input bounds $[\underline{u}, \overline{u}]$ are excluded manually.

2.3 Implementable Framework for STS

In this section, we describe the implementation of framework presented in Section 2.2. A visual representation of the framework is shown in Figure 2.4. Note that there are slight differences from the conceptual framework in the hybrid system and BOS computation used. The reasons for these will be discussed in the relevant sections.

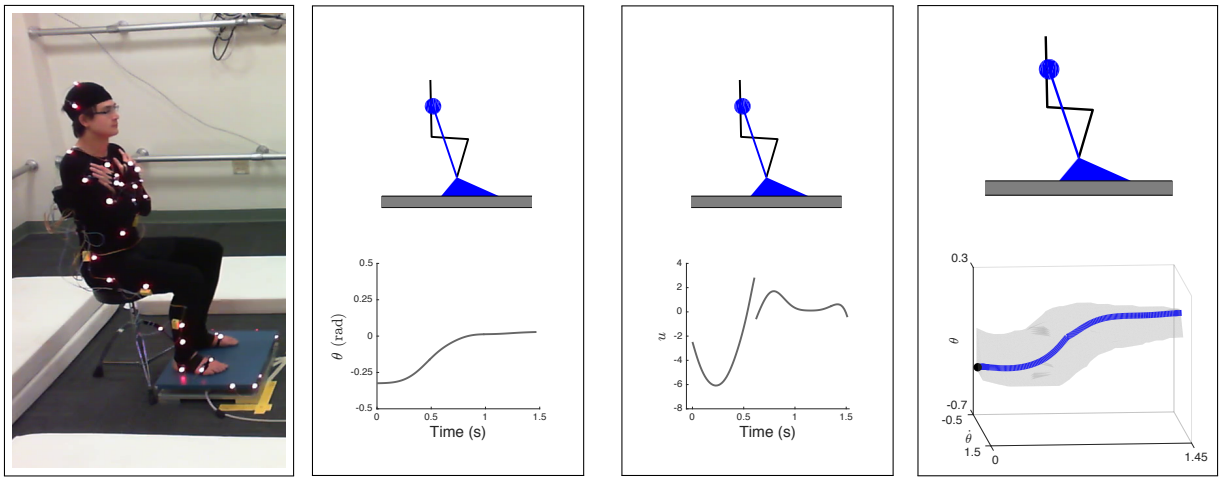

Data Collection Modeling Input ID Compute BOS

Figure 2.4: Implementable Framework

Individualized Hybrid Model

We consider two models to represent an individual's STS action: a single inverted pendulum model (IPM), shown in Figure 2.5a, and a double inverted pendulum (DPM), shown in Figure 2.5b. Pai and Patton first used the IPM to determine the feasible states in which balance could be obtained [16]. Most recently, the IPM has been used to determine the feasible COM velocities and accelerations at seat-off (when the subject leaves the chair) that lead to balance [91, 20].

The IPM model consists of an inverted pendulum attached to a fixed foot on the ground. Let $[\theta, \dot{\theta}]^T$ represent the angle (with respect to the vertical) and angular velocity of the pendulum, which is the state space X of the IPM, and u represent the actuation at the ankle. The dynamics of the IPM are

$$\begin{aligned} \ddot{\theta} &= f(t, \theta, \dot{\theta}) + g(t, \theta, \dot{\theta})u \\ &= \frac{g}{l}\sin(\theta) + \frac{1}{ml^2}u \end{aligned} \tag{2.7}$$

where g is gravity, m is the mass and l is the length of the pendulum, and u is the exogenous input. To fit the observed data from motion capture to the IPM, we set g to be gravity,

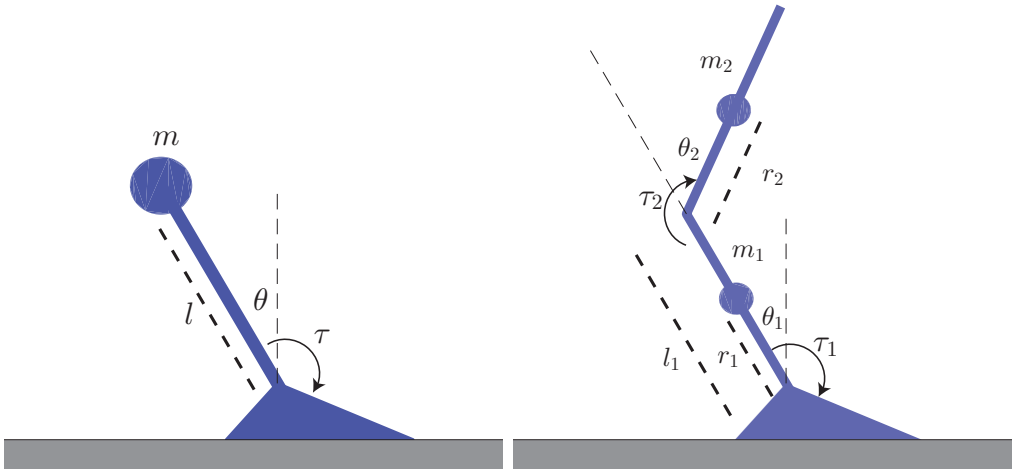

(a) Inverted Pendulum Model (b) Double Pendulum Model

Figure 2.5: STS models

m as the subject's mass, l as the average distance from the subject's ankle to the subject's COM[2], and θ as the angle from the ankle to the subject's COM.

The DPM consists of a double inverted pendulum attached to a fixed foot on the ground. Let $\theta = [\theta_1, \theta_2]^T$ and $[\theta_1, \theta_2, \dot{\theta}_1, \dot{\theta}_2]^T$ represent the state space X of the DPM and $\boldsymbol{u} = [u_1, u_2]^T$ represent the ankle and hip actuation. The dynamics of the DPM are standard double pendulum dynamics are:

$$M(\theta, \dot{\theta})\ddot{\theta} + C(\theta, \dot{\theta})\dot{\theta} + N(\theta) = \boldsymbol{u} \tag{2.8}$$

where

$$M(\theta, \dot{\theta}) = \begin{bmatrix} m_1 r_1^2 + m_2 r_2^2 + l_1 m_2 \left(l_1 + 2 r_2 \cos(\theta_2)\right) & m_2 r_2 (l_1 \cos(\theta_2) + r_2) \\ m_2 r_2 (l_1 \cos(\theta_2) + r_2) & m_2 r_2^2 \end{bmatrix} \tag{2.9}$$

$$C(\theta, \dot{\theta}) = \begin{bmatrix} -l_1 m_2 r_2 \sin(\theta_2)\dot{\theta}_2 & -l_1 m_2 r_2 \sin(\theta_2)(\dot{\theta}_1 + \dot{\theta}_2) \\ l_1 m_2 r_2 \sin(\theta_2)\dot{\theta}_1 & 0 \end{bmatrix} \tag{2.10}$$

$$N(\theta) = \begin{bmatrix} -g m_1 r_1 \sin(\theta_1) + g m_2 \left(-l_1 \sin(\theta_1) - r_2 \sin(\theta_1 + \theta_2)\right) \\ -g m_2 r_2 \sin(\theta_1 + \theta_2) \end{bmatrix} \tag{2.11}$$

where M represents the mass matrix, C represents the coriolis and centrifugal matrix, N represents the potential matrix, g is gravity, and $\boldsymbol{u} \in \mathbb{R}^2$ represents the external input. To fit the observed data from motion capture to the DPM, we set m_1 as the mass of the subject's lower body (calf and thigh), m_2 as the mass of the subject's upper body, l_1 as the average length from the ankle of the subject's ankle to hip, r_1 as the average length to the

[2]Fuijimoto notes that the length of the COM does not affect the results significantly [20].

COM of the lower body, and r_2 as the average length from the hip to the COM of the upper body. θ_1 represents the angle from the subject's ankle to hip and θ_2 represents the angle of the subject's hip to upper body.

The dynamics for the double pendulum can be represented in control affine form as:

$$\begin{aligned}\ddot{\theta} &= M^{-1}(\theta,\dot{\theta})(-C(\theta,\dot{\theta})\dot{\theta} - N(\theta)) + M^{-1}(\theta,\dot{\theta})\boldsymbol{u} \\ &= f(t,\theta,\dot{\theta}) + g(t,\theta,\dot{\theta})\boldsymbol{u}\end{aligned} \tag{2.12}$$

For both models, masses and the COM positions of each individual limb were computed using tabulated values found in [92] and the COM for each model was calculated using the weighted average of each limb's COM.

To model this action using hybrid systems, the transition can be defined when the subject lifts off the chair. However, due to the lack of a knee joint, this event is lost in both the IPM and DPM models. For this work, we ignore this hybrid transition and nature of the STS motion. Due to numerical issues (elucidated later), we treat the STS motion using 3 modes where transitions occur at a fixed time. This is traditionally known as a switched hybrid system defined below:

Definition 2: *A* switched switched hybrid system *is a tuple* $\mathcal{H}_{switch} = (V, \mathcal{D}, U, \mathcal{F}, \mathcal{T})$ *where:*

- V *is a finite set indexing the discrete states of* $\mathcal{H}_{switch}$ *with* $\|V\|$ *as the cardinality of* V*;*
- $\mathcal{D} = \coprod_{j\in V} X_j$ *is a disjoint union of domains, where* $X_j = \left\{x \in \mathbb{R}^{n_j} \mid h_{X_{j_i}}(x) \geq 0, h_{X_{j_i}} \in \mathbb{R}[x], \forall i = \{1,\dots,n_{X_j}\}\right\}$ *is a compact subset where* $n_j \in \mathbb{N}$*;*
- $U = \{u \in \mathbb{R}^m \mid h_{U_i} \geq 0, h_{U_i} \in \mathbb{R}[u], \forall i \in \{1,\dots,n_U\}\}$ *is a compact, convex subset which describes the range space of the control inputs where* $m \in \mathbb{N}$*;*
- $\mathcal{F} = \{(f_j, g_j)\}_{j\in V}$ *is a set of control affine systems, where* $f_j \colon \mathbb{R} \times X_j \to \mathbb{R}^{n_j}$, $g_j \colon \mathbb{R} \times X_j \to \mathbb{R}^{n_j}$, *for* $t \in \mathbb{R}, x \in X_j$, *and* $u \in U$, $f(t,x) + g(t,x)u$ *is a tangent vector on* X_j *at* x, *and* $f, g \in \mathbb{R}[t,x]$*;*
- $\mathcal{T} = \bigcup_{i=0}^{\|V\|-1}[\tau_i, \tau_{i+1}]$ *is a union of the time intervals where* $\mathcal{T} = [0,T]$ *and* τ_{i+1} *denotes the switching time from mode* i *to* $i+1$ *with* $\tau_0 = 0$ *and* $\tau_{\|V\|} = T$*;*

A switched hybrid system can be thought of an autonomous hybrid system with a known switching sequence, a guard on time and an identity reset map. As the switching sequence is known, without loss of generality, the sequence of modes traversed can be defined as $\{0, 1, \dots, \|V\| - 1\}$.

Collecting Observations

We obtain detailed observations consisting of 43 markers on the body for the STS motion using the PhaseSpace Impulse X2 system [93]. Using Recap2, the markers are processed to obtain a skeletal model [74]. Afterwards, the joint angles are processed to project the skeleton down to the IPM and DPM model. The full experimental protocol for collecting data can be found in Chapter 4.

Identifying an Input from Observations

For optimal control we utilize collocation of polynomial with forward Euler [94] to transform the optimal control problem in Equation 2.4 into a nonlinear optimization program. Collocation discretizes the dynamics *in time* and enforces the equality:

$$x_{k+1} = x_k + \Big(f(t, x_k) + g(t, x_k)u_k\Big)t_s \tag{2.13}$$

for all k, x_k and u_k where t_s is the integration timestep[3]. The full optimal control algorithm is presented in Equation 2.14.

$$\begin{aligned} \inf_{\{x_k\}_{k=0}^N, \{u_k\}_{k=0}^N} \quad & \|x_k - x_{\text{obs}}(kt_s)\|_2^2 \\ \text{s.t.} \quad & x_{k+1} = x_k + \left(f_{j(k)}(kt_s, x_k) + g_{j(k)}(kt_s, x_k)u_k\right) t_s, \quad \forall k = \{0, \ldots, N-1\} \end{aligned} \tag{2.14}$$

where $j(k)$ is a monotonic function denoting the mode at timestep k, t_s denotes the timestep and N denotes the number of timesteps such that $t_s = T/(N-1)$.

However, due to requirements of our algorithm (elucidated later), polynomial inputs are required and the collocation algorithm used is shown below:

$$\begin{aligned} \inf_{\{x_k\}_{k=0}^N, \{u_{i,j}\}_{i,j=0}^{d,\|V\|}} \quad & \|x_k - x_{\text{obs}}(kt_s)\|_2^2 \\ \text{s.t.} \quad & x_{k+1} = x_k + \Bigg(f_{j(k)}(kt_s, x_k) \\ & \qquad + g_{j(k)}(kt_s, x_k) \left(\sum_{i=0}^{d} u_{i,j(k)} (kt_s)^i \right) \Bigg) t_s \\ & \forall k = \{0, \ldots, N-1\} \end{aligned} \tag{2.15}$$

where $j(k)$ is a monotonic function denoting the mode at timestep k, t_s denotes the timestep, N denotes the number of timesteps such that $t_s = T/(N-1)$, and d denotes the degree of

[3]Note that collocation methods exist with higher order methods such as Runge-Kutta which increases the accuracy of u_{obs}.

the input. For the rest of the paper, we refer to the nominal input in mode j generated by the optimal control as $u_{\text{obs},j}(t)$ where:

$$u_{\text{obs},j}(t) = \sum_{i=0}^{d} u_{i,j} t^i \tag{2.16}$$

Feedback Controller Design

To determine the feedback gain K_j for each mode j, the Linear Quadratic Regulator (LQR) algorithm in Equation 2.17 is applied to determine the optimal state feedback law $u(t)$ that minimizes a quadratic cost.

$$\begin{aligned} \min_{u_{cc,j} \in L^2([0,T])} \frac{1}{2} \int_{T_j} \Big(& (x(t) - x_{\text{obs}}(t))^T Q (x(t) - x_{\text{obs}}(t)) \\ & + u_{cc,j}(t)^T R u_{cc,j}(t) \Big) dt \\ \text{s.t.} \quad & \dot{x}(t) = A_j x(t) + B_j (u_{\text{obs},j}(t) + u_{cc,j}(t,x)) \end{aligned} \tag{2.17}$$

By selecting $Q = I$ and $R = 0.01I$ where I is the identity matrix of appropriate dimension, the resulting controller is designed to minimize the Q-weighted l_2 error of $x(t)$ from $x_{\text{obs}}(t)$. A_j and B_j are obtained via small-angle approximations of f_j and g_j.

The complete controller for each mode j is written as:

$$\begin{aligned} u_j(t,x) &= u_{\text{obs},j}(t) + K_j(x(t) - x_{\text{obs}}(t)) \\ &= u_{\text{obs},j}(t) + u_{cc,j}(t,x) \end{aligned} \tag{2.18}$$

For linear systems, the LQR problem has a closed form solution provided by the Algebraic Ricatti Equation and the optimal controller is a linear state feedback law [95].

Computing the Basin of Stability

Due to numerical reasons, a modified optimization algorithm inspired by [34] to compute this BOS is presented:

$$\inf_{v_j \in C^1(T_j \times \mathbb{R}^n, \mathbb{R}^n)} \quad \sum_{j \in V} \int_{T_j \times X_j} v_j(t,x) dt dx \qquad (D')$$

$$\begin{aligned} \text{s.t.} \quad & \frac{\partial v_j(t,x)}{\partial x} \Big(f_j(t,x) + g_j(t,x) u_j(t,x) \Big) + \frac{\partial v_j}{\partial t} \leq 0 && \forall (t,x) \in T_j \times X_j && \text{(2.19a)} \\ & v_j(\tau_j, x) \geq v_{j+1}(\tau_j, x) && \forall x \in X_j && \text{(2.19b)} \\ & v_j(t,x) \geq 0 && \forall (t,x) \in T_j \times X_j && \text{(2.19c)} \\ & v_{\|V\|-1}(T,x) \geq \alpha && \forall x \in X_T && \text{(2.19d)} \end{aligned}$$

where $\alpha \in \mathbb{R}$ with $\alpha > 0$ is a parameter that can be selected by the use, and $\|V\| - 1$ is the final mode. After computing $v_j(t,x)$, points in the domain $T_j \times X_j$ that exceed input bounds $[\underline{u}, \overline{u}]$ are excluded manually via masking.

To understand the relationship between the solution, v_j, to this optimization problem and the BOS notice that $v_j(t,x) \geq \alpha$ for points that belong on the BOS:

Lemma 2: *If v_j is a solution to (D), then $v_j(0,\cdot) \geq \alpha$ on the BOS.*

Proof. Since $\frac{\partial v_j(t,x)}{\partial x}\left(f_j(t,x) + g_j(t,x)u(t,x)\right) + \frac{\partial v_j}{\partial t} \leq 0$ on $T_j \times X_j$ and $v_{\|V\|-1}(T,\cdot) \geq \alpha$ on X_T, we have $x(t) \in X$ and $x(T) \in X_T$.

$$\begin{aligned}
\alpha &\leq v_{\|V\|-1}(T, x(T)) \\
&= v_{\|V\|-1}(t_{\|V\|-1}, x) + \int_{T_{\|V\|-1}} \left(\frac{\partial v_{\|V\|-1}(t,x)}{\partial x}\left(f_{\|V\|-1}(t,x)\right) \right. \\
&\qquad \left. + \frac{\partial v_{\|V\|-1}(t,x)}{\partial x}\left(g_{\|V\|-1}(t,x)u(t,x)\right) + \frac{\partial v_{\|V\|-1}}{\partial t} \right) dt \qquad (2.20) \\
&\leq v_{\|V\|-1}(\tau_{\|V\|-1}, x) \\
&\dots \\
&\leq v_0(0,x)
\end{aligned}$$

□

Therefore, the BOS at $t = 0$ is given by the levelset defined by $\{x \in \mathcal{D} \,|\, v_0(0,x) \geq 0\}$. In fact, the BOS in mode j is given by the levelset defined by $\{(t,x) \in [0,T] \times \mathcal{D} \,|\, v_j(t,x) \geq 0\}$. To solve (D') numerically, $v_j(t,x)$ and the dynamics are assumed to be polynomial and the state space and target set are assumed to be semialgebraic sets. Using the S-procedure, positivity constraints are converted to sum-of-squares constraint [36]. This optimization program constructs an outer approximation to the BOS [69]. This method requires polynomial dynamics and inputs. Instead of using a high degree polynomial to model the input, the input is partitioned into three, resulting in the 3 mode switched system mentioned earlier. More details are given in Chapter 3.

2.4 Summary

In this chapter, a conceptual framework for studying the basin of stability of human locomotion is presented followed by an implementable framework for specifically analyzing a subject's sit-to-stand motion. A summary showing the differences between the conceptual and implementable framework is shown in Figure 2.1. Further details regarding the basin of stability calculation are provided in Chapter 3 with experimental results in Chapter 4.

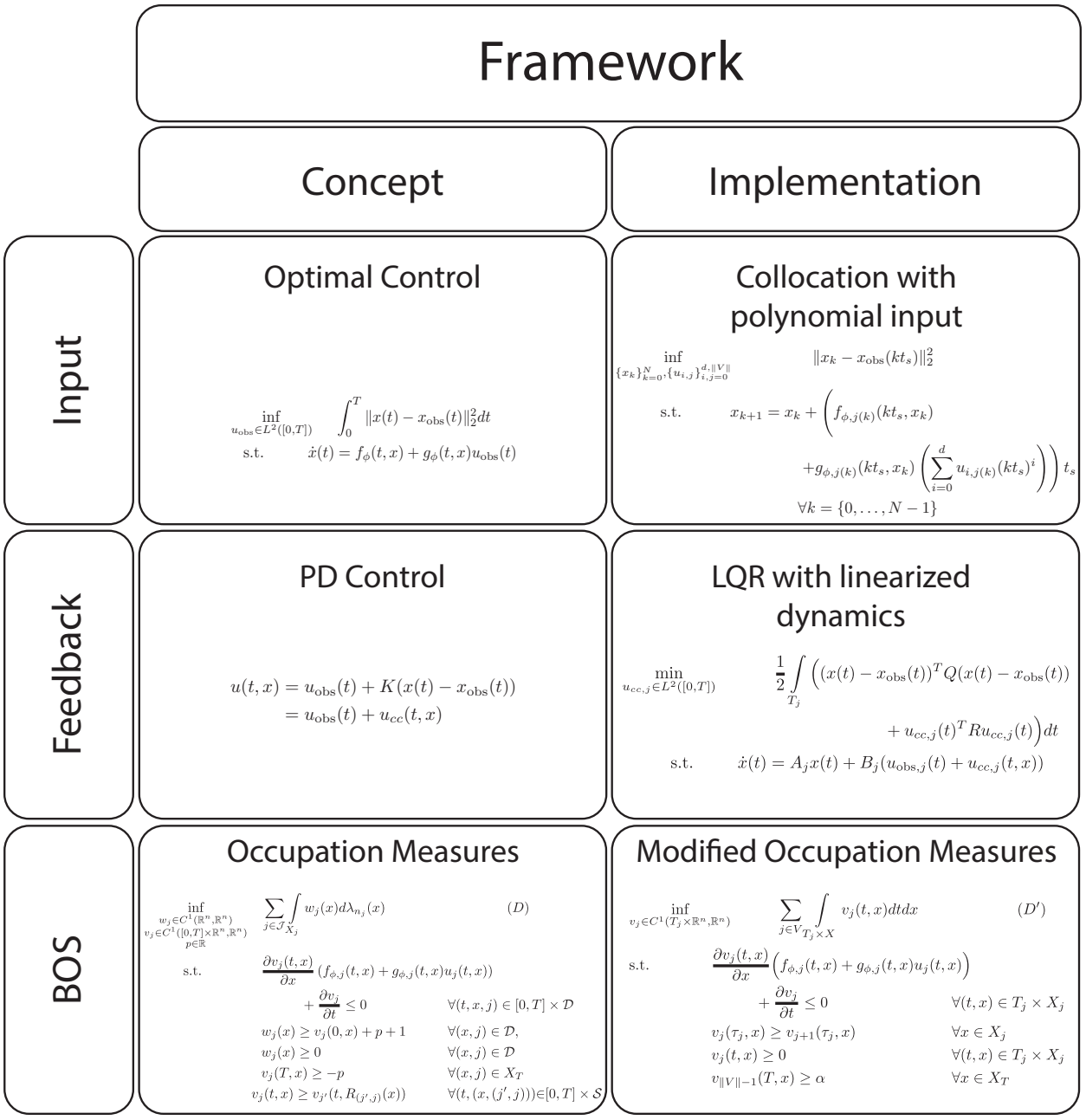

Figure 2.6: Conceptual and Implementable Framework

Chapter 3

Computational Tools for Stability

3.1 Introduction

Hybrid systems have been widely adopted as a modeling tool due to their expressive power while describing the dynamics of systems undergoing continuous and discrete transitions simultaneously. Consequently, the development of computationally tractable algorithms for reachability analysis is critical not only for verifying safe system behavior, but also due to its applicability during incremental control design [96]. This chapters presents a numerical approach to construct the set of points that reach a given target set at a specified finite time for controlled polynomial hybrid systems.

Many algorithms have been proposed to compute this *backwards reachable set* (BRS) for a hybrid system. The most popular of such techniques rely either upon the linearity of the distinct subsystems of the hybrid system under investigation [97, 98], the Hamilton-Jacobi-Bellman Equation [32], or Lyapunov-type analysis [62, 99, 100]. Though the Hamilton-Jacobi-Bellman based methods work even in the presence of general nonlinear dynamics, they rely upon state-space discretization which can restrict their applicability to systems of low dimensionality. In contrast, Lyapunov based methods can be applied to higher dimensional systems. These approaches rely on checking Lyapunov's criteria for stability using sums-of-squares (SOS) programming which are formulated as semi-algebraic constraints and casted as SOS constraints using the S-procedure. However, constructing these Lyapunov functions requires solving a nonconvex bilinear program that is solved using some form of alternation, which is not guaranteed to converge to global or even local optima and requires feasible initialization.

In this chapter, we address these issues by presenting a convex approach to computing the BRS of a semialgebraic target set for a controlled polynomial hybrid system in the presence of semialgebraic state and input constraints. Our approach is inspired by the method presented in [34], which describes a framework based on *occupation measures* for computing the BRS for classical polynomial dynamical systems. The contributions in this chapter are three–fold. First, in Section 3.2, we formulate the determination of the BRS as an infinite dimensional linear program (LP) over the space of nonnegative measures. The target set in this formulation can in fact be divided amongst the distinct subsystems of the hybrid system. Second, in Section 3.4, we construct a sequence of finite dimensional relaxations to our infinite dimensional LP in terms of semidefinite programs (SDP)s. Finally, in Section 3.4, we prove that each solution to the sequence of SDPs is an *outer approximation* to the largest possible BRS with asymptotically vanishing conservatism. In Section 3.5, we demonstrate the performance of our approach on 3 examples.

3.2 Preliminaries

In this section, we formalize our problem of interest, construct an infinite dimensional LP, and note that the solution of this LP is equivalent to solving our problem of interest. We make substantial use of measure theory, and the unfamiliar reader may wish to consult [70]

for an introduction.

Problem Statement

Next, we describe the target set whose BRS we are interested in computing. First, we define the projection of the target set in each mode $j \in \mathcal{J}$:

$$X_{T_j} = \left\{ x \in X_j \,|\, h_{T_{j_i}}(x) \geq 0, h_{T_{j_i}} \in \mathbb{R}[x], \forall i = \{1, \ldots, n_{T_j}\} \right\} \tag{3.1}$$

where X_{T_j} is the semi-algebraic set given by the polynomial functions $h_{T_{j_i}}$. The *target set* is then defined as:

$$X_T = \coprod_{j \in \mathcal{J}} X_{T_j}. \tag{3.2}$$

Given a finite final time $T > 0$, our goal is to compute the time–limited BRS of X_T for hybrid dynamical system defined in Definition 1 which is defined as:

$$\begin{aligned} \mathcal{X} = \Big\{ & (x_0, j) \in \mathcal{D} \mid \exists u : [0, T] \to U \text{ Lebesgue measurable} \\ & \text{s.t. } x : [0, T] \to \mathcal{D} \text{ defined via Algorithm 2,} \\ & x(0) = x_0 \in X_j, x(T) \in X_T \Big\}. \end{aligned} \tag{3.3}$$

We denote the projection of $\mathcal{X}$ in each mode j as:

$$\mathcal{X}_j = \left\{ x_0 \in X_j \mid (x_0, j) \in \mathcal{X} \right\} \tag{3.4}$$

We make the following assumption to solve this problem:
Assumption 5: *X_{T_j} is compact for all $j \in \mathcal{J}$.*

Liouville's Equation

Liouville's equation is an partial differential equation in classical statistical and Hamiltonian mechanics concerning the conservation of probability density through dynamics. It is the analogue of the conservation of mass via dynamics for probability densities. In this section, we first show how to define a measure along a system trajectory (via the idea of occupation measures), then define a measure along a *set* of system trajectories, and show how Liouville's equation "falls" out of the derivation.

We compute $\mathcal{X}$ by defining measures over $[0, T] \times X_j$ for each $j \in \mathcal{J}$ whose supports' model the evolution of *families of trajectories* in each mode. An initial condition and its relationship with respect to the terminal set can be understood via Algorithm 2, but the relationship between a family of trajectories and the terminal set is best understood differently. To

appreciate this distinct perspective, first define the linear operator $\mathcal{L}_j : C^1\big([0,T] \times X_j\big) \to C\big([0,T] \times X_j \times U\big)$ on a test function v as:

$$\mathcal{L}_j v = \frac{\partial v}{\partial t} + \sum_{i=1}^{n_j} \frac{\partial v}{\partial x_i}\Big([f(t,x)]_i + [g(t,x)u(t)]_i\Big), \tag{3.5}$$

and its adjoint operator $\mathcal{L}_j' : C\big([0,T] \times X_j \times U\big)' \to C^1\big([0,T] \times X_j\big)'$ by the adjoint relation:

$$\langle \mathcal{L}_j' \mu, v\rangle = \langle \mu, \mathcal{L}_j v\rangle = \int\limits_{[0,T]\times X_j \times U} \mathcal{L}_j v(t,x,u) d\mu(t,x,u) \tag{3.6}$$

for all $\mu \in \mathcal{M}\big([0,T] \times X_j \times U\big)$ and $v \in C^1\big([0,T] \times X_j\big)$.

Using this operator, we can understand the evolution of any test function $v \in C^1\big([0,T] \times X_j\big)$ in X_j. To make this explicit, consider the evolution of a point $x_{\tau_i} \in X_j$ beginning at time $\tau_i \in [0,T]$ under the control input $u(\cdot|\tau_i, x_{\tau_i})$ according to Algorithm 2, which we denote by $x(\cdot|\tau_i, x_{\tau_i})$. Define the first hitting time of a guard in X_j as:

$$\begin{aligned}\tau_f(\tau_i, x_{\tau_i}) = \min\Big\{T, \inf\{\tau \geq \tau_i \mid \exists i \in \mathcal{J} \text{ s.t.} \\ x(\tau|\tau_i, x_{\tau_i}) \in G_{i,j}\}\Big\}.\end{aligned} \tag{3.7}$$

It follows from Equation (3.5) that:

$$\begin{aligned} v(\tau_f, x(\tau_f|\tau_i, x_{\tau_i})) - v(\tau_i, x_{\tau_i}) &= \int_{\tau_i}^{\tau_f} \frac{d}{dt} v(t, x(t|\tau_i, x_{\tau_i}))dt &(3.8)\\ &= \int_{\tau_i}^{\tau_f} \mathcal{L}_j v(t, x(t|\tau_i, x_{\tau_i}), u(t|\tau_i, x_{\tau_i}))dt, &(3.9)\end{aligned}$$

where we have suppressed the dependence on τ_i and x_{τ_i} in τ_f. A standard approach to determining the BRS of a system imposes Lyapunov conditions on the test functions and their derivatives. However, this results in nonconvex bilinear matrix inequalities. Instead we examine conditions on the space of measures–the dual to the space of continuous functions–in order to arrive at a convex formulation.

To do this, we begin by defining an *occupation measure*:

$$\mu(A \times B \times C|\tau_i, x_{\tau_i}) = \int_0^T I_{A\times B\times C}\left(t, x(t|\tau_i, x_{\tau_i}), u(t|\tau_i, x_{\tau_i})\right) dt, \tag{3.10}$$

for all subsets $A \times B \times C$ in the Borel σ-algebra of $[0,T] \times X_j \times U$, where $I_{A\times B\times C}(\cdot)$ denotes the indicator function on a set $A \times B \times C$. As a result of its definition, the occupation measure of a set $A \times B \times C$ quantifies the amount of time the graph of a solution and its associated control, $(t, x(t|\tau_i, x_{\tau_i}), u(t|\tau_i, x_{\tau_i}))$, spends in $A \times B \times C$. For example, Figure 3.1 shows the occupation measure for two sets: $A_1 \times B_1$ and $A_2 \times B_2$ for a trajectory $x(t|x_0)$

beginning at x_0[1]. Since the trajectory $x(t|x_0)$ goes through $A_1 \times B_1$, the occupation measure $\mu(A_1 \times B_1|x_0)$ is non-zero. Conversely, since the trajectory $x(t|x_0)$ does not go through $A_2 \times B_2$, the occupation measure $\mu(A_2 \times B_2|x_0)$ is zero.

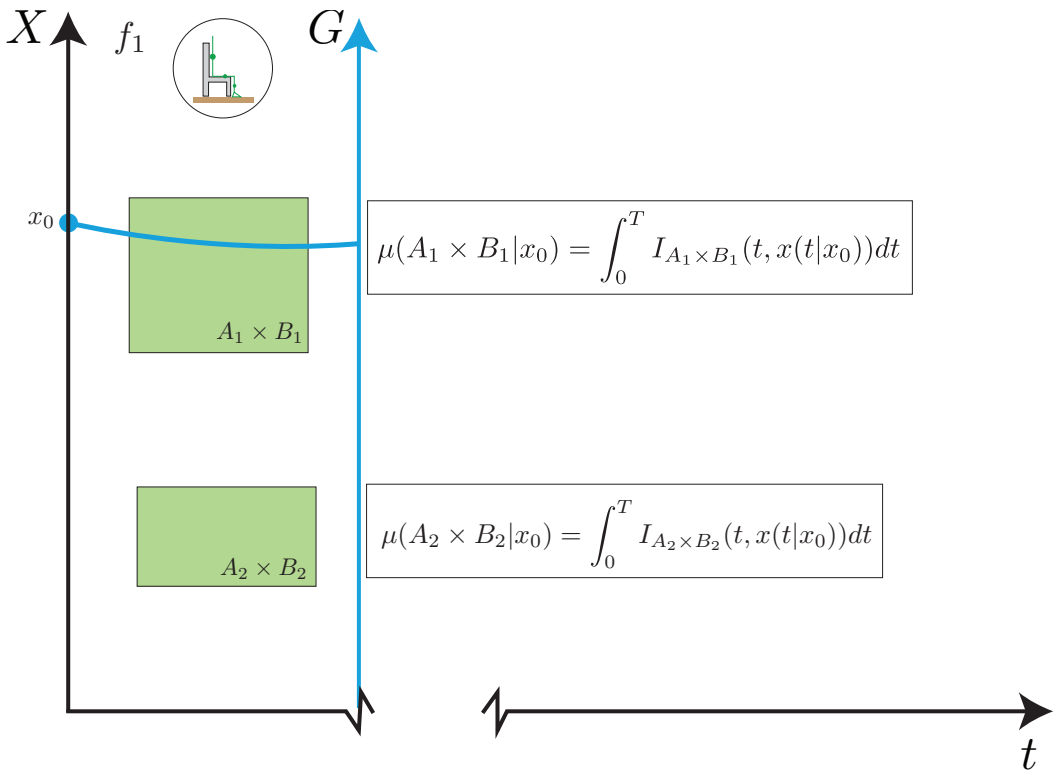

Figure 3.1: Pictorial view of occupation measures on a single trajectory for a system *without* input.

For any measurable function $h : [0, T] \times X_j \times U \to \mathbb{R}$ an occupation measure by construction satisfies the following property:

$$\int_0^T h(t, x(t|\tau_i, x_{\tau_i}), u(t|\tau_i, x_{\tau_i}))dt = \int_{[0,T]\times X_j \times U} h(t, x, u)d\mu(t, x, u|\tau_i, x_{\tau_i}) \tag{3.11}$$

As a result, Equation (3.9) then becomes:

$$v(\tau_f, x(\tau_f|\tau_i, x_{\tau_i})) - v(\tau_i, x_{\tau_i}) = \int_{[0,T]\times X_j \times U} \mathcal{L}_j v(t, x, u)d\mu(t, x|\tau_i, x_{\tau_i}). \tag{3.12}$$

If the initial state whose evolution was of interest was not just a single point at a specific time, but was a family of points each beginning at distinct times, then we could define an

[1]For simplicity, the system has no input and hence, no set C.

initial measure, $\mu_i \in \mathcal{M}([0,T] \times X_j)$, whose support coincided with this family of points and their initialization times. We could then define an *average occupation measure* shown in Figure 3.2, $\mu \in \mathcal{M}([0,T] \times X_j \times U)$ by:

$$\mu(A \times B \times C) = \int_X \mu(A \times B \times C | \tau_i, x_{\tau_i}) d\mu_i(\tau_i, x_{\tau_i}), \tag{3.13}$$

and a *final measure*, $\mu_f \in \mathcal{M}([0,T] \times X_j)$ by:

$$\mu_f(A \times B) = \int_{[0,T] \times X_j} I_{A \times B}(\tau_f(\tau_i, x_{\tau_i}), x(\tau_f | \tau_i, x_{\tau_i})) d\mu_i(\tau_i, x_{\tau_i}). \tag{3.14}$$

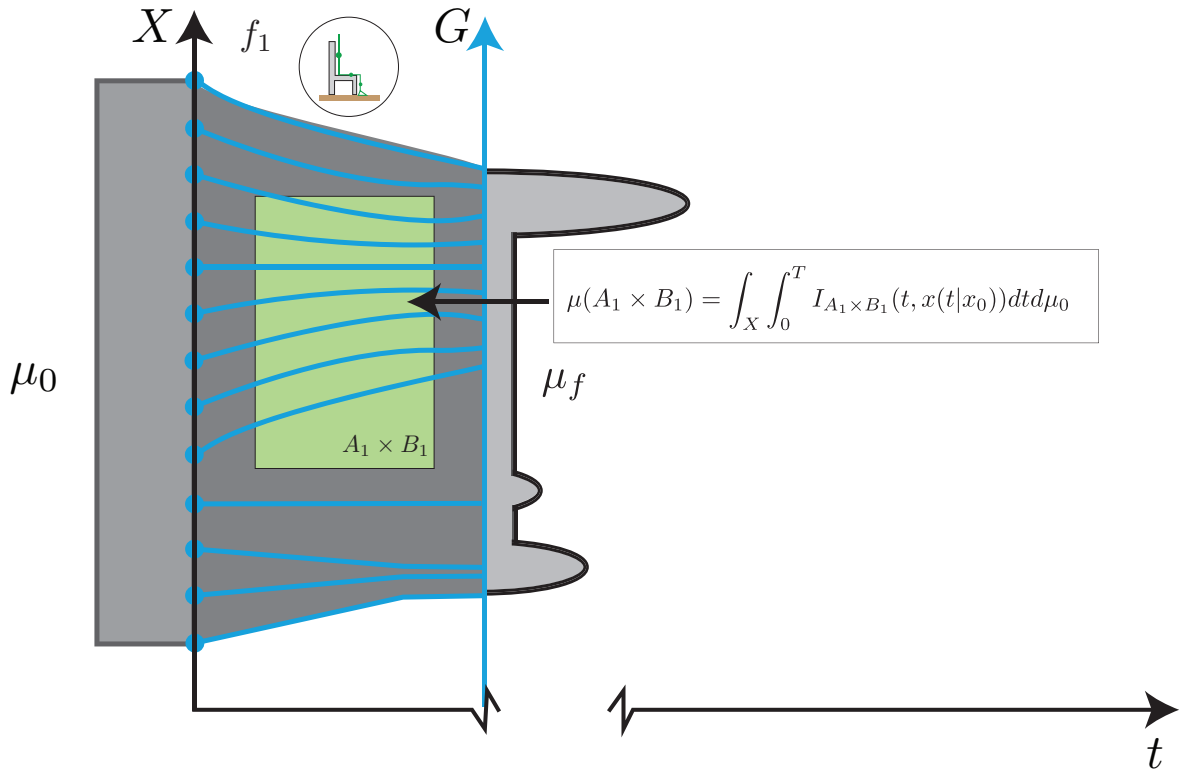

Figure 3.2: Pictorial view of initial, average occupation and final measures for a system *without* input.

Integrating with respect to μ_i, introducing the average occupation measure and final measure, and using the property defined in Equation (3.11), Equation (3.12) becomes:

$$\langle \mu_f, v \rangle - \langle \mu_i, v \rangle = \langle \mu, \mathcal{L}_j v \rangle, \quad \forall v \in C^1([0,T] \times X_j). \tag{3.15}$$

The support of μ models the flow of trajectories beginning in the support of μ_i, and the support of μ_f represents the distribution of states at some final time after being transported along system trajectories from the initial measure.

Notice that Equation (3.15) is linear in its measure components. Since Equation (3.15) must hold for all test functions, we obtain a linear operator equation:

$$\mu_f - \mu_i = \mathcal{L}'_j \mu, \tag{3.16}$$

called Liouville's Equation, which is a classical result in statistical physics that describes the evolution of a density of particles within a fluid [101]. The occupation measures μ_i, μ and μ_f, along with Liouville's equation allow us to reason about *families* of trajectories of a classical dynamical system. This equation is satisfied by families of trajectories generated according to Algorithm 2 starting from the initial distribution μ_i. The converse statement is true for control affine systems with a convex admissible control set, as we have assumed. We refer the reader to [34, Appendix A] for an extended discussion of Liouville's Equation. Extending the applicability of this result to hybrid systems requires careful modification and selection of the initial and final measures.

3.3 Infinite Dimensional Linear Program

In this section, we derive an infinite-dimensional LP characterization of the BRS of X_T. The basic idea is to introduce and then maximize the mass of initial occupation measures defined just at $t = 0$ in each of the hybrid modes, denoted μ_0^j, under the constraint that it is dominated by the Lebesgue measure, i.e., $\lambda \geq \mu_i^j$. System dynamics in each mode are captured by Liouville's Equation (3.16) on each mode and state and terminal constraints are handled by suitable constraints on the support of the measures. To describe all trajectories of a hybrid system, two modifications are required.

First, trajectories arriving at a guard in each mode must be detected. By splitting the final measure in each mode into two types of measures this detection can be accomplished:

$$\mu_f^j = \mu_T^j + \sum_{(j',j)\in\Gamma} \mu^{S_{(j',j)}} \tag{3.17}$$

with $\mu_T^j \in \mathcal{M}(\{T\} \times X_{T_j})$ and $\mu^{S_{(j',j)}} \in \mathcal{M}([0,T] \times S_{(j',j)})$. Second, once trajectories arriving at a guard, $S_{(j',j)}$, are detected they must be re-initialized after the application of the reset map, $R_{(j',j)}$, in mode $j' \in \mathcal{J}$. To accomplish this task, the mass of the occupation measure at each guard at each time between $[0,T]$ must be transferred exactly to the new domain after resetting:

Lemma 3: *Let $\mathcal{H}$ be a controlled polynomial hybrid system as in Definition 1 and $\mu^{S_{(j',j)}} \in \mathcal{M}([0,T] \times S_{(j',j)})$. Let $\sigma \in \mathcal{M}([0,T] \times R_{(j',j)}(S_{(j',j)}))$ be such that:*

$$\langle \sigma, v \rangle = \langle R^*_{(j',j)} \mu^{S_{(j',j)}}, v \rangle \quad \forall v \in C([0,T] \times X_{j'}), \tag{3.18}$$

where $\langle R^*_{(j',j)}\mu^{S_{(j',j)}}, v\rangle$ *is defined as:*

$$\int_{[0,T]\times S_{(j',j)}} v(t, R_{(j',j)}(x))|\det(DR_{(j',j)})(x)|d\mu^{S_{(j',j)}}(t,x), \tag{3.19}$$

and $DR_{(j',j)}$ *is the Jacobian of* $R_{(j',j)}$*, then* $x \in spt(\mu^{S_{(j',j)}})$ *(*$x \notin spt(\mu^{S_{(j',j)}})$*) if and only if* $R_{(j',j)}(x) \in spt(\sigma)$ *(*$x \notin spt(\sigma)$*).*
Intuition: This lemma is the analogue of the change of variables theorem in calculus for measures.

Proof. This proof follows directly from [102, Theorem 263D]. □

As a result of this lemma, for any $t \in [0,T]$ the support of $R^*_{(j',j)}\mu^{S_{(j',j)}}(t,\cdot)$ characterizes exactly the reinitialization in mode j' after the application of the reset map $R_{(j',j)}$ of points arriving at the guard $S_{j',j}$ at time t. By splitting the initial measure in each mode into two types of measures this reinitialization can be accommodated:

$$\mu^j_i = \mu^j_0 + \sum_{(j,j')\in\Gamma} R^*_{(j,j')}\mu^{S_{(j,j')}} \tag{3.20}$$

with $\mu^j_0 \in \mathcal{M}(\{0\}\times X_j)$ and $\mu^{S_{(j,j')}} \in \mathcal{M}([0,T]\times S_{(j,j')})$.

With these two modifications, we can define an infinite dimensional LP, P, that maximizes the size of the BRS, modeled by $\sum_{j\in\mathcal{J}} \mathrm{spt}(\mu^j_0)$, for a given target set, modeled by $\mathrm{spt}(\mu^j_T)$ for each $j \in \mathcal{J}$. That is, define P as:

$$\begin{aligned}
p^\star = \sup \quad & \sum_{j\in\mathcal{J}} \mu^j_0(X_j) && (P)\\
\text{s.t.} \quad & \mathcal{L}'_j\mu^j = \mu^j_T + \sum_{(j',j)\in\Gamma}\mu^{S_{(j',j)}} - \mu^j_0 - \sum_{(j,j')\in\Gamma} R^*_{(j,j')}\mu^{S_{(j,j')}} && \forall j\in\mathcal{J},\\
& \mu^j_0 + \hat{\mu}^j_0 = \lambda_{n_j} && \forall j\in\mathcal{J},\\
& \sum_{j\in\mathcal{J}} \mu^j_T(X_{T_j}) = \sum_{j\in\mathcal{J}} \mu^j_0(X_j), &&\\
& \mu^j, \mu^j_0, \hat{\mu}^j_0, \mu^j_T \geq 0 && \forall j\in\mathcal{J},\\
& \mu^{S_e} \geq 0 && \forall e\in\Gamma,
\end{aligned}$$

where the given data are $\mathcal{H}$ and X_T and the supremum is taken over a tuple of measures $(\mu, \mu_0, \hat{\mu}_0, \mu_T, \mu_{\mathcal{S}}) \in \big(\mathcal{M}([0,T]\times\mathcal{D})\times\mathcal{M}(\{0\}\times\mathcal{D})\times\mathcal{M}(\{0\}\times\mathcal{D})\times\mathcal{M}(\{T\}\times X_T)\times\mathcal{M}([0,T]\times\mathcal{S})\big)$. For notational convenience, we denote the $j\in\mathcal{J}$ slice of μ using the super index j (i.e. for any $(t,x)\in[0,T]\times X_j$ set $\mu^j(t,x) = \mu(t,x,j)$) and applied a similar convention to $\mu_0, \hat{\mu}$, and μ_T. Similarly, we denote the $(j,j')\in\Gamma$ slice of $\mu_{\mathcal{S}}$ using the notation $\mu^{S_{(j,j')}}$. Implicitly, $\mathrm{spt}(\mu)\subset[0,T]\times\mathcal{D}$ which means μ is non-zero on $[0,T]\times\mathcal{D}$ and zero outside the $[0,T]\times\mathcal{D}$. Also, we have $\mathrm{spt}(\mu_0)\subset\mathcal{D}$, $\mathrm{spt}(\mu_T)\subset X_T$, and $\mathrm{spt}(\mu_{\mathcal{S}})\subset[0,T]\times\mathcal{S}$.

A pictorial version of P of a 1-dimensional hybrid system with 2 discrete modes is shown in Figure 3.3. Starting at $t = 0$, μ_0 is defined as the initial measure in mode 1. The measure flows via the dynamics through Liouville's equation in mode 1 until it hits the guard $S_{(2,1)}$, upon which the measure undergoes a reset map to become $R^{\star}_{(2,1)}\mu^{S_{(2,1)}}$ in mode 2. The "terminal" measure for mode 1 is defined by $\mu^{S_{(2,1)}}$. In mode 2, the measure flows via the dynamics through Liouville's equation in mode 2 until time $t = T$ ending at the terminal measure μ_T. Informally, P is tasked with maximizing $\sum_{j\in\mathcal{J}} \mu_0^j(X_j)$. There are two ways to maximize this sum: first, $\mu_0^j(X_j)$ can be scaled up. However, this scaling is limited by the constraint $\mu_0^j + \hat{\mu}_0^j = \lambda_{n_j}$, which limits how much μ_0^j can be scaled to the Lebesgue measure. Second, $\text{spt}(\mu_0^j)$ can grow in volume, and through Liouville's equation, $\text{spt}(\mu_T)$ grows. However, the growth of $\text{spt}(\mu_T)$ is constrained to X_T so $\text{spt}(\mu_0)$ is limited to the BRS of X_T.

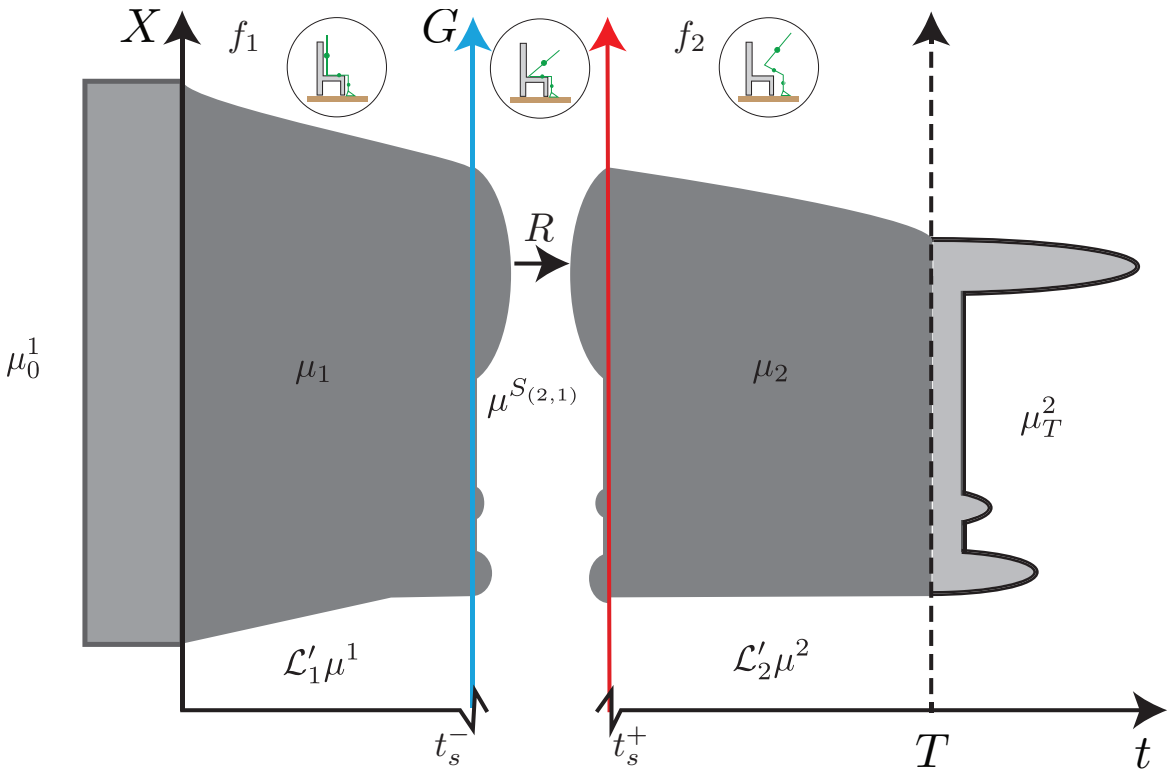

Figure 3.3: Pictorial View of Hybrid Occupation Measures.

The constraint $\sum_{j\in\mathcal{J}} \mu_T^j(X_{T_j}) = \sum_{j\in\mathcal{J}} \mu_0^j(X_j)$ ensures that the BRS computes only points arriving at the target set at time T rather than at any of the guards at time T. The slack measures (denoted with "hats") are introduced to impose the constraints $\lambda \geq \mu_0^j$ which ensures that the optimal value of P is the Lebesgue measure of the largest achievable BRS. These observations are summarized next:

Theorem 4: *The optimal value of P is equal to $\sum_{j\in\mathcal{J}}\lambda_{n_j}(\mathcal{X}_j)$, i.e. the sum of the Lebesgue measures of the BRS restricted to each domain of the hybrid system.*
Intuition: Theorem 4 proves that the optimal value of P is equal to the volume of $\mathcal{X}_j$ which is the BRS, converting the optimization over volume to a tractable closed-form equation.

Proof. Notice that for any initial condition in $x_0 \in \mathcal{X}$ there is a hybrid trajectory constructed via Algorithm 2 with $x(T) \in X_T$. As a result for any initial measure μ_0 with $\text{spt}(\mu_0) \subset \mathcal{X}$ there exists occupation measures $\hat{\mu}_0, \mu, \mu^T$, and μ_S such that the constraints of P are satisfied. Thus $p^* \geq \sum_{j\in\mathcal{J}}\lambda_{n_j}(\mathcal{X}_j)$.

To prove the other direction, notice that as a result of [34, Theorem 1], $p^* = \sum_{j\in\mathcal{J}}\lambda_{n_j}(\text{spt}(\mu_0^j))$. Suppose then for contradiction that $\exists j \in \mathcal{J}$ such that $\lambda_{n_j}(\text{spt}(\mu_0^j) \setminus \mathcal{X}_j) > 0$. Using [34, Lemma 3] there exists a family of trajectories generated via Algorithm 2 starting from μ_0^j generating the occupation measures μ^j and $\mu_T^j + \sum_{j',j}\mu^{S_{(j',j)}}$. If the trajectories arrive at X_T, then we have a contradiction, so suppose there exists some $j' \in \mathcal{J}$ such that the trajectories arrive at $S_{(j',j)}$. Using Lemma 3, we can reset these trajectories and reapply the same argument to extend the family of trajectories through modes of the system. Notice that due to Assumption 1 the times of transitions for this family of trajectories are strictly monotonic. If at the final time T the family of trajectories generated according to Algorithm 2 are in $\text{spt}(\mu_T)$, then we have a contradiction, so suppose that they are at a guard. In that instance $\sum_{j\in\mathcal{J}}\mu_T^j(X_{T_j}) < \sum_{j\in\mathcal{J}}\mu_0^j(X_j)$ which would violate a constraint in P, so we have a contradiction and $p^* = \sum_{j\in\mathcal{J}}\lambda_{n_j}(\text{spt}(\mu_0^j)) \leq \sum_{j\in\mathcal{J}}\lambda_{n_j}(\mathcal{X}_j)$. □

Next, lets define the dual program to P denoted D as:

$$
\begin{aligned}
d^\star = \inf \quad & \sum_{j\in\mathcal{J}}\int_{X_j} w_j(x)d\lambda_{n_j}(x) && (D)\\
\text{s.t.} \quad & \mathcal{L}_j v_j(t,x,u) \leq 0 && \forall (t,x,j,u) \in [0,T]\times\mathcal{D}\times U\\
& w_j(x) \geq v_j(0,x) + p + 1 && \forall (x,j) \in \mathcal{D},\\
& w_j(x) \geq 0 && \forall (x,j) \in \mathcal{D}\\
& v_j(T,x) \geq -p && \forall (x,j) \in X_T\\
& v_j(t,x) \geq v_{j'}(t, R_{(j',j)}(x)) && \forall (t,(x,(j',j))) \in [0,T]\times\mathcal{S}
\end{aligned}
$$

where the given data are $\mathcal{H}$ and X_T and the infimum is taken over the tuple $(v,w,p) \in \big(C^1([0,T]\times\mathcal{D}) \times C(\mathcal{D}) \times \mathbb{R}\big)$. As before, for notational convenience, we denote the $j \in \mathcal{J}$ slice of v using the subscript j (i.e. for every $(t,x) \in [0,T]\times X_j$ set $v_j(t,x) = v(t,x,j)$) and apply a similar convention to w. The next result verifies that there is no duality gap between the two programs:

Theorem 5: *There is no duality gap between P and D.*
Intuition: This theorem proves that the solution for problems P and D are equivalent. Often, solving one is easier than the other and this gives us options to choose which to solve.

Proof. To prove this theorem, P and D are converted to standard LP form, from which the theorem follows from [103, Theorem 3.10]. Let

$$\begin{aligned} C &:= \big(C([0,T]\times\mathcal{D})\times C(\{0\}\times\mathcal{D})\times C(\{0\}\times\mathcal{D})\times C(\{T\}\times X_T)\times C([0,T]\times\mathcal{S})\big) \\ M &:= \big(\mathcal{M}([0,T]\times\mathcal{D})\times \mathcal{M}(\{0\}\times\mathcal{D})\times \mathcal{M}(\{0\}\times\mathcal{D})\times \mathcal{M}(\{T\}\times X_T)\times \mathcal{M}([0,T]\times\mathcal{S})\big) \end{aligned} \tag{3.21}$$

and let K denote the positive cone of nonnegative continuous functions in C and K' denote the positive cone of nonnegative measures of M, which is the topological dual of K. The cone K' is equipped with the weak* topology (see...). P can be rewritten as:

$$\begin{aligned} p^\star = \sup \quad & \langle \gamma, c\rangle \\ \text{s.t.} \quad & A'\gamma = \beta \\ & \gamma \in K' \end{aligned} \tag{3.22}$$

where the supremum is over the vector $\gamma := (\mu, \mu_0, \hat{\mu}_0, \mu_T, \mu_{\mathcal{S}})$, the linear operator $A' : K' \to \big(C^1([0,T]\times\mathcal{D})'\times \mathcal{M}(\{0\}\times\mathcal{D})\times \mathcal{M}(\{0\}\times\mathcal{D})\times \mathcal{M}(\{T\}\times X_T)\times \mathcal{M}([0,T]\times\mathcal{S})\big)$ where

$$A'\gamma := \begin{bmatrix} \mathcal{L}_j'\mu^j - \mu_T^j - \sum_{(j',j)\in\Gamma}\mu^{S_{(j',j)}} + \mu_0^j + \sum_{(j,j')\in\Gamma} R^*_{(j,j')}\mu^{S_{(j,j')}} \\ \mu_0^j + \hat{\mu}_0^j \\ \sum_{j\in\mathcal{J}}\mu_T^j(X_{T_j}) - \sum_{j\in\mathcal{J}}\mu_0^j(X_j) \end{bmatrix} \tag{3.23}$$

, $\beta = [0,\lambda,0] \in \mathcal{M}([0,T]\times\mathcal{D})\times\mathcal{M}(0\times\mathcal{D})\times\mathbb{R}$, and $c = [0,1,0,0,0] \in C$. The objective function is $\langle\gamma, c\rangle = \sum_j \int_{X_j} d\mu_0^j = \sum_j \mu_0^j(X_j)$.

The dual problem to P can be interpreted as:

$$\begin{aligned} d^\star = \inf \quad & \langle \beta, z\rangle \\ \text{s.t.} \quad & A(z) - c \in K \end{aligned} \tag{3.24}$$

where the infimum is over $z := (v, w, p) \in \big(C^1([0,T]\times\mathcal{D})\times C(\mathcal{D})\times\mathbb{R}\big)$, and the linear operator $A : C^1([0,T]\in\mathcal{D})\times C(\mathcal{D})\times\mathbb{R}\to C$ is defined by

$$A(z) := \begin{bmatrix} \mathcal{L}_j v_j(t,x,u) \\ w_j(x) - v_j(0,x) - p \\ w_j(x) \\ v_j(T,x) + p \\ v_j(t,x) - v_{j'}(t, R_{(j',j)}(x)) \end{bmatrix} \tag{3.25}$$

. Notice that A and A' satisfy the adjoint relation $\langle A'\gamma, z\rangle = \langle\gamma, Az\rangle$ and P is the same as the problem in 3.22. By [103, Theorem 3.10], the LP problems P and D have no duality gap. □

Theorem 5 shows that the solution to P and D are equivalent and allows us to utilize the dual, which is simpler to compute numerically, to obtain outer approximations of the BRS:

Theorem 6: *For every $j \in \mathcal{J}$, $\mathcal{X}_j \subset \{x_0 \in X_j | w_j(x) \geq 1\}$ for any feasible w_j of D. Furthermore, there is a sequence of feasible solutions to D such that for each $j \in \mathcal{J}$, the w_j-component converges from above to $I_{\mathcal{X}_j}$ in the L^1 norm and almost uniformly.*
Intuition: This shows that the 1-levelset of w_j denotes an outer-approximation of the BRS, providing an *analytical* expression for the outer-approximation for the BRS.

Proof. To prove the first result, consider a feasible (v, w) in D. Given any $(x_0, j_0) \in \mathcal{X}$, there exists a u such that $u(t) \in U$ for all $t \in [0, T]$ and $x(T) \in X_T$ where $x : [0, T] \to \mathcal{D}$ is generated via Algorithm 2. Let $\{\tau_i\}_{i=0}^n \subset [0, T]$ be the strictly monotonic and finite sequence of transition times of the trajectory (which exists by Assumption 1) with $\tau_0 = 0$ and $\tau_n = T$ and $\{j_i\}_{i=0}^n \subset \mathcal{J}$ be the sequence of visited modes. Due to D's constraints:

$$\begin{aligned}
-p \leq v_{j_n}(T, x(T)) &= v_{j_{n-1}}(\tau_{n-1}, R_{(j_n, j_{n-1})}(x(\tau_{n-1}))) + \\
&+ \int_{\tau_{n-1}}^{\tau_n} \mathcal{L}_{j_n} v_{j_n}(t, x(t), u(t)) dt \\
&\leq v_{j_{n-1}}(\tau_{n-1}^-, x(\tau_{n-1}^-)) \\
&= v_{j_{n-2}}(\tau_{n-2}, R_{(j_{n-1}, j_{n-2})}(x(\tau_{n-2}))) + \\
&+ \int_{\tau_{n-2}}^{\tau_{n-1}} \mathcal{L}_{j_{n-1}} v_{j_{n-1}}(t, x(t), u(t)) dt \\
&\ldots \\
&\leq v_{j_0}(0, x_0) \leq w_{j_0}(x_0) - p - 1,
\end{aligned}$$

which proves the first statement since (x_0, j_0) was arbitrary. Next we prove the second result. By Theorem 4, the optimal solution to P is $I_{\mathcal{X}}$ where for general sets, $I_A(x)$ is the indicator function such that

$$I_A(x) = \begin{cases} 1 & x \in A \\ 0 & x \notin A \end{cases} \tag{3.26}$$

. Therefore, $p^\star = \sum_j \int_{X_j} I_{\mathcal{X}_j}(x) d\lambda(x)$ which also equates to the volume of $\mathcal{X}$. By Theorem 5, there is no duality gap and $p^\star = d^\star$ and there exists a sequence $(v_k, w_k, p_k) \in C^1([0, T] \in \mathcal{D}) \times C(\mathcal{D}) \times \mathbb{R}$ feasible such that:

$$p^\star = d^\star = \lim_{k \to \infty} \sum_j \int_{X_j} w_{j_k}(x) d\lambda(x) \tag{3.27}$$

where w_{j_k} is the component of w_k in mode j. Since $w_k \geq 1$ on $\mathcal{X}$ and $w_k \geq 0$ on $\mathcal{D}$, $w_k \geq I_{\mathcal{X}}$ on $\mathcal{D}$ for all k. Therefore, we have:

$$p^\star = \sum_j \int_{X_j} I_{\mathcal{X}_j}(x) d\lambda(x) = \lim_{k \to \infty} \sum_j \int_{X_j} w_{j_k}(x) d\lambda(x) \tag{3.28}$$

$$\lim_{k \to \infty} \sum_j \int_{X_j} \left(w_{j_k}(x) - I_{\mathcal{X}_j}(x) \right) d\lambda(x) = 0 \tag{3.29}$$

Since the integrand is non-negative, w_k converges to $I_{\mathcal{X}}$ in L^1 norm. From X, there exist a subsequence converging almost uniformly. □

Theorem 6 proves that the set $\{x_0 \in X_j | w_j(x) \geq 1\}$ is an outer-approximation of the BRS and that there is a sequence of solutions to D which converge almost uniformly to the optimal w.

3.4 Numerical Implementation

The infinite–dimensional problems P and D are not directly amenable to computation. However, a sequence of finite–dimensional approximations in terms of SDPs can be obtained by characterizing measures in P by their *moments*, and restricting the space of functions in D to polynomials. The solutions to each of the SDPs in this sequence can be used to construct outer approximations that converge to the solution of the infinite–dimensional LP. A comprehensive introduction to such *moment relaxations* can be found in [104].

For each $j \in \mathcal{J}$, measures on the set $[0,T] \times X_j$ are completely determined by their action (via integration) on a dense subset of the space $C^1([0,T] \times X_j)$ [70]. Since $[0,T] \times X_j$ is compact by assumption, the Stone–Weierstrass Theorem [70, Theorem 4.45] allows us to choose the set of polynomials as this dense subset. Every polynomial on $\mathbb{R}^n$, say $p \in \mathbb{R}[x]$, can be expanded in the monomial basis via:

$$p(x) = \sum_{\alpha \in \mathbb{N}^n} p_\alpha x^\alpha, \tag{3.30}$$

where $\alpha \in \mathbb{N}^n$ ranges over vectors of non-negative integers, $x^\alpha = \prod_{i=1}^n [x]_i^{[\alpha]_i}$, and $\text{vec}(p) = (p_\alpha)_{\alpha \in \mathbb{N}^n}$ is the vector of coefficients of p. By definition, the p_α are real and only finitely many are non-zero. We define $\mathbb{R}_k[x]$ to be those polynomials such that p_α is non-zero only for $\alpha \in \mathbb{N}^n_k$. The degree of a polynomial, $\deg(p)$, is the smallest k such that $p \in \mathbb{R}_k[x]$.

The moments of a measure $\mu \in \mathcal{M}(K)$ for $K \subset \mathbb{R}^n$ are:

$$y_\mu^\alpha = \int x^\alpha d\mu(x). \tag{3.31}$$

Integration of a polynomial with respect to a measure μ can be expressed as a linear functional of its coefficients:

$$\langle \mu, p \rangle = \int p(x) d\mu(x) = \sum_{\alpha \in \mathbb{N}^n} p_\alpha y_\mu^\alpha = \text{vec}(p)^T y_\mu. \tag{3.32}$$

Integrating the square of a polynomial $p \in \mathbb{R}_k[x]$, we obtain:

$$\int p(x)^2 d\mu(x) = \text{vec}(p)^T M_k(y_\mu) \text{vec}(p), \tag{3.33}$$

where $M_k(y_\mu)$ is the *truncated moment matrix* defined by

$$[M_k(y_\mu)]_{(\alpha,\beta)} = y_\mu^{\alpha+\beta} \tag{3.34}$$

for $\alpha, \beta \in \mathbb{N}^n_k$. Note that for any positive measure μ, the matrix $M_k(y_\mu)$ must be positive semidefinite. Similarly, given $h \in \mathbb{R}[x]$ one has:

$$\int p(x)^2 h(x) d\mu(x) = \mathrm{vec}(p)^T M_k(h, y_\mu)\mathrm{vec}(p), \tag{3.35}$$

where $M_k(h, y)$ is a *localizing matrix* defined by

$$[M_k(h, y_\mu)]_{(\alpha,\beta)} = \sum_{\gamma \in \mathbb{N}^n} h_\gamma y_\mu^{\alpha+\beta} \tag{3.36}$$

for all $\alpha, \beta \in \mathbb{N}^n_k$. Note that the positive semidefiniteness of a localizing matrix for a moment sequence allows us to guarantee the existence of a Borel measure on the semialgebraic set defined by h whose moments coincide with the given moment sequence [104, Theorem 3.8]. The localizing and moment matrices are symmetric and linear in the moments.

Approximating Problems

Finite dimensional SDPs approximating P can be obtained by replacing constraints on measures with constraints on moments. All of the equality constraints of P can be expressed as an infinite–dimensional linear system of equations which the moments of the measures appearing in P must satisfy. This linear system is obtained by restricting to polynomial test functions: $v(t, x) = t^\alpha x^\beta$ and $w(x) = x^\beta$, $\forall \alpha \in \mathbb{N}$ and $\forall \beta \in \mathbb{N}^n$. For example, Liouville's equation in P is obtained via:

$$\begin{aligned}\int_{[0,T]\times X_j \times U} \mathcal{L}_j v_j(t,x,u) d\mu^j(t,x,u) = &\int_{X_{T_j}} v_j(T,x) d\mu_T(x) + \\ + \sum_{(j',j)\in\Gamma} \int_{[0,T]\times S_{(j',j)}} v_j(t,x) d\mu^{S_{(j',j)}}(t,x) &- \int_{X_j} v_j(0,x) d\mu_0(x) - \\ + \sum_{(j,j')\in\Gamma} \int_{[0,T]\times S_{(j,j')}} v(t, R_{(j,j')}(x)) |\det(DR_{(j,j')}(x))| d\mu^{S_{(j,j')}}(t,x)&\end{aligned}$$

Notice in particular that $|\det(DR_{(j,j')}(x))|$ is a polynomial function by Definition 1.

A *finite–dimensional* linear system is obtained by truncating the degree of the polynomial test functions to $2k$. Let $\Xi_\mathcal{J} = \coprod_{j\in\mathcal{J}} \mu^j$, $\Xi_0 = \coprod_{j\in\mathcal{J}} \{\mu_0^j, \hat{\mu}_0^j\}$, $\Xi_\Gamma = \coprod_{e\in\Gamma} \mu^{S_e}$, and $\Xi_T = \coprod_{j\in\mathcal{J}} \mu_T^j$. Let $\mathbf{y}_k^\eta = (y_{k,\xi}) \subset \mathbb{R}$ be a vector of sequences of moments truncated to degree $2k$ for each $(\xi, j) \in \Xi_\eta$ and for each $\eta \in \{\mathcal{J}, 0, \Gamma, T\}$. The finite–dimensional linear system is then represented by the linear system:

$$A_k(\mathbf{y}_k^\mathcal{J}, \mathbf{y}_k^0, \mathbf{y}_k^\Gamma, \mathbf{y}_k^T) = b_k. \tag{3.37}$$

Constraints on the support of the measures also need to be imposed (see [104] for details). Let the k-th relaxed SDP representation of P, denoted P_k, be defined as:

$$
\begin{aligned}
\sup \quad & \sum_{j\in\mathcal{J}} y^0_{k,\mu^j_0} && (P_k)\\
\text{s.t.} \quad & A_k(\mathbf{y}^{\mathcal{J}}_k, \mathbf{y}^0_k, \mathbf{y}^{\Gamma}_k, \mathbf{y}^T_k) = b_k, \\
& M_k(y_{k,\xi}) \succeq 0 && \forall (\xi, j) \in \{\Xi_{\mathcal{J}}, \Xi_0, \Xi_{\Gamma}, \Xi_T\},\\
& M_{k_{X_{j_i}}}(h_{X_{j_i}}, y_{k,\xi}) \succeq 0 && \forall (i,\xi,j) \in \{1,\dots,n_{X_j}\}\times \Xi_{\mathcal{J}},\\
& M_{k_{X_{j_i}}}(h_{X_{j_i}}, y_{k,\xi}) \succeq 0 && \forall (i,\xi,j) \in \{1,\dots,n_{X_j}\}\times \Xi_{0},\\
& M_{k_{S_{e_i}}}(h_{e_i}, y_{k,\xi}) \succeq 0 && \forall (i,\xi,e) \in \{1,\dots,n_{e}\}\times \Xi_{\Gamma},\\
& M_{k_{T_{j_i}}}(h_{T_{j_i}}, y_{k,\xi}) \succeq 0 && \forall (i,\xi,j) \in \{1,\dots,n_{T_j}\}\times \Xi_{T},\\
& M_{k-1}(h_{\tau}, y_{k,\xi}) \succeq 0 && \forall (\xi, j) \in \{\Xi_{\mathcal{J}}, \Xi_{\Gamma}\},
\end{aligned}
$$

where the given data are $\mathcal{H}$ and X_T and the supremum is taken over the sequence of moments, $\mathbf{y}^{\mathcal{J}}_k, \mathbf{y}^0_k, \mathbf{y}^{\Gamma}_k, \mathbf{y}^T_k$, $h_\tau = t(T-t)$, $k_{X_{j_i}} = k - \lceil \deg(h_{X_{j_i}})/2 \rceil$, $k_{S_{e_i}} = k - \lceil \deg(h_{e_i})/2 \rceil$, $k_{T_{j_i}} = k - \lceil \deg(h_{T_{j_i}})/2 \rceil$, and $\succeq 0$ denotes positive semi-definiteness. For each $k \in \mathbb{N}$, p^*_k denote the supremum of P_k.

The dual of P_k can be constructed as a sums-of-squares (SOS) program denoted D_k for each $k \in \mathbb{N}$. It is obtained by restricting the optimization space in the D to the polynomial functions with degree truncated to $2k$ and replacing the non-negativity constraint D with an SOS constraint [36]. To make this explicit, for each $j \in \mathcal{J}$, let $Q_k(h_{X_{j_1}}, \dots, h_{X_{j_{n_{X_j}}}}) \subset \mathbb{R}_{2k}[x]$ be the set of polynomials $q \in \mathbb{R}_{2k}[x]$ (i.e. of total degree less than $2k$) expressible as:

$$
q = s_0 + \sum_{i=1}^{n_{X_j}} s_i h_{X_{j_i}}, \tag{3.38}
$$

for some polynomials $\{s_i\}_{i=0}^{n_{X_j}} \subset \mathbb{R}_{2k}[x]$ that are the sums of squares of other polynomials where $x \in X_j$. Every such polynomial is clearly non-negative on X_j. Similarly, for each $j \in \mathcal{J}$ and $e \in \Gamma$, define $Q_{2k}(h_\tau, h_{X_{j_1}}, \dots, h_{X_{j_{n_{X_j}}}}) \subset \mathbb{R}_{2k}[t,x]$, $Q_{2k}(h_{T_{j_1}}, \dots, h_{T_{j_{n_{T_j}}}}) \subset \mathbb{R}_{2k}[x]$, and $Q_{2k}(h_\tau, h_{T_{e_1}}, \dots, h_{T_{e_{n_e}}}) \subset \mathbb{R}_{2k}[t,x]$. Employing this notation, the k-th relaxed SDP

representation of D, denoted D_k, is defined as:

$$\begin{aligned}
\inf \quad & \sum_{j\in\mathcal{J}} l^T \mathrm{vec}(w_j) && (D_k)\\
\text{s.t.} \quad & -\mathcal{L}_j v_j \in Q_{2k}(h_\tau, h_{X_{j_1}}, \ldots, h_{X_{j_{n_{X_j}}}}) && \forall j \in \mathcal{J},\\
& w_j - v_j(0,\cdot) - p - 1 \in Q_{2k}(h_{X_{j_1}}, \ldots, h_{X_{j_{n_{X_j}}}}) && \forall j \in \mathcal{J},\\
& w_j \in Q_{2k}(h_{X_{j_1}}, \ldots, h_{X_{j_{n_{X_j}}}}) && \forall j \in \mathcal{J},\\
& v_j(T,\cdot) + p \in Q_{2k}(h_{T_{j_1}}, \ldots, h_{T_{j_{n_{T_j}}}}) && \forall j \in \mathcal{J},\\
& v_j - v_{j'} \circ (1, R_e) \in Q_{2k}(h_\tau, h_{T_{e_1}}, \ldots, h_{T_{e_{n_e}}}) && \forall e := (j', j) \in \Gamma,
\end{aligned}$$

where the given data are $\mathcal{H}$ and X_T, the infimum is taken over the vector of polynomials $(v, w, p) \in \coprod_{j\in\mathcal{J}} \mathbb{R}_{2k}[t,x] \times \coprod_{j\in\mathcal{J}} \mathbb{R}_{2k}[x] \times \mathbb{R}$, and l is a vector of moments associated with the Lebesgue measure (i.e. $\int_X w_j \, d\lambda = l^T \mathrm{vec}(w_j)$ for all $w_j \in \mathbb{R}_{2k}[x]$ and $j \in \mathcal{J}$). For notational convenience in the description of D_k we denote the $j \in \mathcal{J}$ slice of v using the subscript j (i.e. for every $(t,x) \in [0,T] \times X_j$ we let $v_j(t,x) = v(t,x,j)$) and apply a similar convention to w. For each $k \in \mathbb{N}$, let d_k^* denote the infimum of D_k. In fact, the following result holds:

Theorem 7: *For each $k \in \mathbb{N}$, there is no duality gap between P_k and D_k.*

Proof. By establishing that P_k is bounded due to the constraint $\mu_0 + \hat{\mu}_0 = \lambda$ and then arguing that the feasible set of the SDP, D_k, has an interior point which is sufficient to establish zero duality gap [105, Theorem 5]. A complete proof can be found in [34, Appendix D]. □

Convergence of Approximating Problems

Next, we prove the convergence properties of P_k and D_k. We begin by proving that the polynomial w_j approximates the indicator function on $\mathcal{X}_j$. As we increase k, this approximation gets tighter.

Theorem 8: *For each $k \in \mathbb{N}$ and $j \in \mathcal{J}$, let $w_{j_k} \in \mathbb{R}_{2k}[x]$ denote the j-slice of the w-component of the solution to D_k, and let $\bar{w}_{j_k}(x) = min_{i\le k} w_{j_i}(x)$. Then, w_{j_k} converges from above to $I_{\mathcal{X}_j}$ in the L^1 norm, and $\bar{w}_{j_k}(x)$ converges from above to $I_{\mathcal{X}_j}$ in the L^1 norm and almost uniformly.*

Intuition: This proof shows that the 1-super-levelset of the *polynomial* w_j converges to the BRS in L^1 and almost uniformly.

Proof. As each w_{j_k} is independent of the w polynomial in other modes, convergence needs only to be proven for a single mode. This proof is a straightforward extension of Theorem 5 in [34] we which reiterate here for completeness. From Theorem 5 and 6, for any j, k and $\epsilon > 0$ there exists a $(v_{j_k}, w_{j_k}, p_{j_k}) \in \left(C^1([0,T] \times \mathcal{D}) \times C(\mathcal{D}) \times \mathbb{R}\right)$ feasible such that $w_{j_k} \ge I_{\mathcal{X}_j}$

and $\int_{X_j}(w_{j_k} - I_{\mathcal{X}_j})d\lambda \leq \epsilon$. Let:

$$\begin{aligned} \widetilde{v}_{j_k}(t,x) &= v_{j_k}(t,x) - \epsilon t + (T+1)\epsilon \\ \widetilde{w}_{j_k}(x) &= w_{j_k}(x) + (T+3)\epsilon \end{aligned} \tag{3.39}$$

Following from these equations, $\mathcal{L}_j\widetilde{v}_{j_k} = \mathcal{L}_j v_{j_k} - \epsilon < 0$, $\widetilde{v}_{j_k}(T,x) = v_{j_k}(T,x) + \epsilon > 0$, and $\widetilde{w}_{j_k}(x) - \widetilde{v}_{j_k}(0,x) \geq 1 + 2\epsilon > 1$. Since v_{j_k} is a solution to P, the solution $(\widetilde{v}_{j_k}, \widetilde{w}_{j_k}(x), p_k)$ also satisfies the constraints in D and furthermore, the solution is strictly feasible with a margin of at least ϵ. Since $[0,T] \times X_j$ is compact, the Stone–Weierstrass Theorem [70, Theorem 4.45] allows us to choose polynomials $\hat{v}_{j_k}(t,x)$ and $\hat{w}_{j_k}$ of sufficiently high degree such that

$$\sup_{[0,T]\times X_j} |\widetilde{v}_{j_k} - \hat{v}_{j_k}| < \epsilon \tag{3.40}$$

$$\sup_{[0,T]\times X_j} |\widetilde{\mathcal{L}}_j v_{j_k} - \mathcal{L}_j \hat{v}_{j_k}| < \epsilon \tag{3.41}$$

$$\sup_{[0,T]\times X_j} |\widetilde{w}_{j_k} - \hat{w}_{j_k}| < \epsilon \tag{3.42}$$

Since the solution $(\widetilde{v}_{j_k}, \widetilde{w}_{j_k})$ has a margin of at least ϵ, the solution $(\hat{v}_{j_k}, \hat{w}_{j_k})$ is also strictly feasible in P. Integrating Equation 3.42 over X_j via the Lebesgue measure, we have

$$\int_{X_j} |\widetilde{w}_{j_k} - \hat{w}_{j_k}| d\lambda \leq \epsilon\lambda(X_j) \tag{3.43}$$

Consequently, we have:

$$\begin{aligned} \int_{X_j} |\hat{w}_{j_k} - w_{j_k}| d\lambda &\leq \int_{X_j} |\hat{w}_{j_k} - \widetilde{w}_{j_k}| + \int_{X_j} |\widetilde{w}_{j_k} - w_{j_k}| d\lambda && (3.44) \\ &\leq \epsilon\lambda(X_j) + (T+3)\epsilon\lambda(X_j) && (3.45) \\ &\leq \epsilon\lambda(X_j)(T+4) && (3.46) \end{aligned}$$

Therefore, we have

$$\int_{X_j} (\hat{w} - I_{\mathcal{X}_j}) d\lambda < \epsilon(1 + \lambda(X_j)(T+4)), \hat{w} \geq I_{\mathcal{X}_j} \tag{3.47}$$

Since X_j is compact, $\epsilon(1 + \lambda(X_j)(T+4)) < \infty$. Since j, k, ϵ were arbitrary, the first statement is proved. The second statement follows since $w_k \to I_{\mathcal{X}_j}$ in L^1 norm, there exist a subsequence $w_{j_{k_m}}$ that converges almost uniformly to $I_{\mathcal{X}_j}$ by X. By definition of $\bar{w}_{j_k}(x)$, $\bar{w}_{j_k}(x) \leq \min\{w_{j_{k_m}}(x) : k_m \leq k\}$ and $\bar{w}_{j_k}$ converges in L^1 norm and almost uniformly. □

As a result of Theorems 1 and 8 we have:

Corollary 1: *$\{d_k^*\}_{k=1}^{\infty}$ and $\{p_k^*\}_{k=1}^{\infty}$ converge monotonically from above to the optimal value of D and P.*

Proof. Monotonic convergence of $d_k^\star$ follows from Theorem 8 and from the fact that a higher order relaxation allows for a looser constraint set. From weak duality, we have $d_k^\star \geq p_k^\star$ and from Theorem 5 and 7, we have $p^\star = d^\star$. Therefore, we have $p_k^\star \geq p^\star$ and $p_{k+1}^\star \leq p_k^\star$ since a higher order relaxation k results in a tighter constraint set of the maximization problem as more moments are enforced. Therefore, $p_k^\star \to p^\star$ monotonically. □

Next, we prove that for each $j \in \mathcal{J}$ the 1-superlevel set of w_j converges in Lebesgue measure to $\mathcal{X}_j$.

Theorem 9: *For each $k \in \mathbb{N}$ and $j \in \mathcal{J}$, let $w_{j_k} \in \mathbb{R}_{2k}[x]$ denote the j-slice of the w-component of the solution to D_k, and let $\mathcal{X}_{j_k} := \{x \in \mathbb{R}^n | w_{j_k}(x) \geq 1\}$. Then,* $\lim_{k\to\infty} \lambda_{n_j}(\mathcal{X}_{j_k} \backslash \mathcal{X}_j) = 0$.

Intuition: This shows that the outer-approximation of the computed BRS converges to the true BRS in the limit.

Proof. Via Theorem 6 we see $w_{j_k} \geq I_{\mathcal{X}_{j_k}} \geq I_{\mathcal{X}_j}$. From Theorem 8, $w_{j_k} \to I_{\mathcal{X}_j}$ in the L^1 norm on X_j. Hence:

$$\lambda_{n_j}(\mathcal{X}_j) = \lim_{k\to\infty} \int_{X_j} w_{j_k} d\lambda_{n_j} \geq \lim_{k\to\infty} \int_{X_j} I_{\mathcal{X}_{j_k}} d\lambda_{n_j} = \lim_{k\to\infty} \lambda_{n_j}(\mathcal{X}_{j_k}).$$

Since $\mathcal{X}_j \subset \mathcal{X}_{j_k}$ for all k, $\lim_{k\to\infty} \lambda_{n_j}(\mathcal{X}_{j_k}) = \lambda_{n_j}(\mathcal{X}_j)$. □

3.5 Implementation and Examples

In this section, we describe the performance of our approach on three examples. The relaxed problems were prepared using SPOTLESS [106] and solved using MOSEK [107] on a machine with an Intel i7-4820k 3.70GHz processor with 32GB RAM. We briefly describe an extension of our algorithm to the case when our goal is to determine whether an initial condition is able to reach a target set within a pre-specified time T rather than exactly at T, which we refer to as the time-free backwards reachable set problem. This is done by allowing the support of $\mu_T \in \mathcal{M}([0,T] \times \mathcal{D})$ in P. Consequently, the only modification on the dual program D is that the non-negativity constraint on v is imposed for all $t \in [0,T]$. Each of the aforementioned corollaries, lemmas, and theorems extend with nearly identical proof and the numerical implementation extends in a straightforward manner. The measures are supported on variables corresponding to time, states and control inputs, totaling $(1+n+m)$ variables where n is the number of states and m is the number of control inputs. The total number of moments in the primal problem scales as $O((1+n+m)^k)$ for a fixed relaxation k and $O(k^{1+n+m})$ for a fixed n, m. Assuming a linear reset map, the number of variables in the dual problem scale as $O(\max(n_v n_{f_j}, n_v n_{g_j} n_u))$ where $n_v, n_{f_j}, n_{g_j}, n_u$ are the degrees of v, f_j, g_j, and u, respectively.

Rimless Wheel

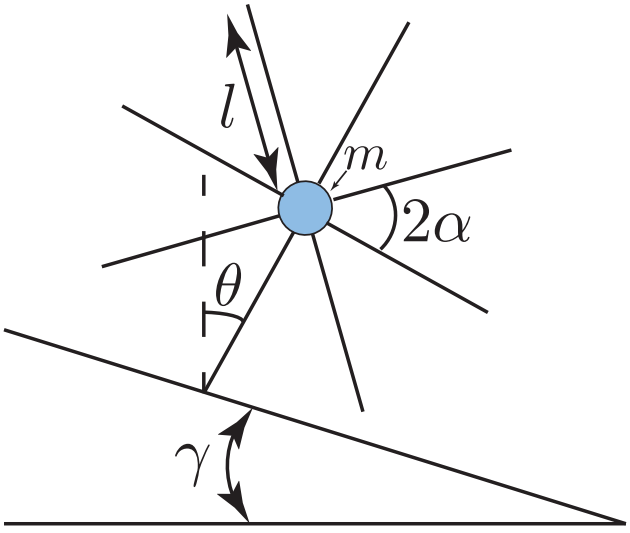

Figure 3.4: Rimless wheel system

The rimless wheel is a simple planar walking model illustrated in Figure 3.4. It consists of a single point mass with spokes radiating outward with dynamics given by an inverted pendulum $f(\theta, \dot{\theta}) = [\dot{\theta}; \sin(\theta)]$, where θ is the angle between the vertical and pinned spoke.

The front spoke hits the ground when $\theta = \alpha + \gamma$, upon which the system undergoes a reset where $[\theta^+, \dot{\theta}^+] := [2\gamma - \theta^-, \cos(2\alpha)\dot{\theta}^-]$.

The limit cycle and basin of attraction of this system have been studied analytically[108]. By choosing $\alpha = 0.4, \gamma = 0.2$, the rimless wheel has a stable limit cycle where the energy lost during ground impact is equal to the change in potential energy through the cycle. Figure 3.5 illustrates this limit cycle along with the phase portrait, with the guard shown in dotted red and the image of the reset map shown in solid red. We considered the task of determining the BRS of the limit cycle with $T = 10$ and for implementation we considered a third-order Taylor expansion of the dynamics and reset map. The result of our computation is illustrated in Figure 3.5. The time to compute the BRS for 6, 8, and 10 degrees took: 1.5s, 4.8s, 18s.

Of interest is the blue curve near the top of Figure 3.5. While the true BRS contains the initial conditions in red (look at Figure 8 in [62]), as the trajectories resulting from the initial conditions evolve *outside* the compact domain and thus not included in the computed BRS.

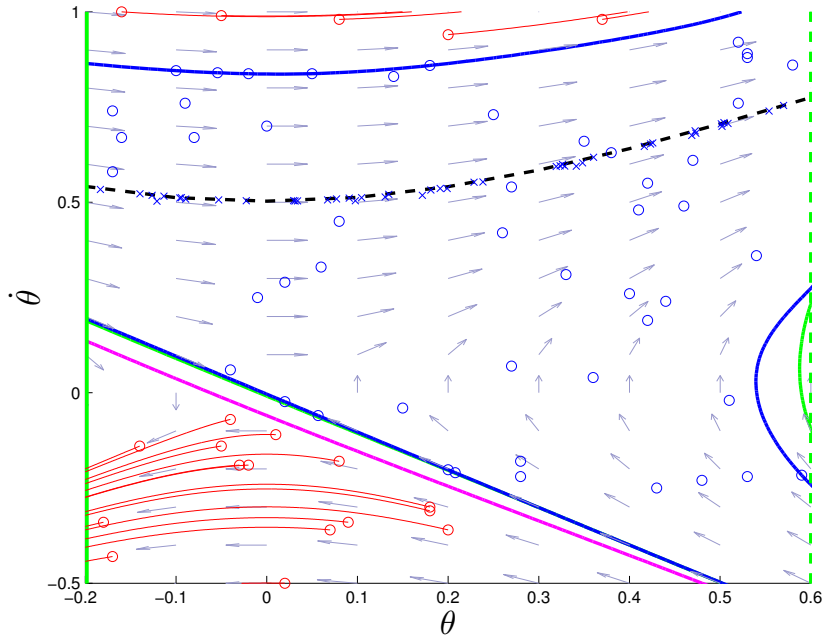

Figure 3.5: BRS of the Rimless Wheel. The limit cycle of the system is drawn in as a dotted black line. The magenta, green, and blue lines denote outer-approximations of the BRS degree 6, 8, and 10, respectively. 50 points were sampled drawn in blue circles within the degree 10 BRS, used as initial conditions, and evolved using the dynamics of the Rimless Wheel (not the Taylor approximation). Their final time state is plotted with the blue X. 20 points were sampled outside the BRS starting at the red circles and their evolutions are plotted.

Vehicle Dynamics

Next, we compute the forward reachable set of the vehicle illustrated in Figure 3.6. Motivated by [109] we model its dynamics as follows:

$$\begin{aligned} m\ddot{x}_1 &= m\dot{x}_2\dot{\psi} + 2F_{x_1f} + 2F_{x_1r} \\ m\ddot{x}_2 &= -m\dot{x}_1\dot{\psi} + 2F_{x_2f} + 2F_{x_2r} \\ I_z\ddot{\psi} &= 2aF_{x_2f} - 2bF_{x_2r} \end{aligned} \tag{3.48}$$

where $m = 2050$ and $I_z = 3344$ denote the vehicle mass and inertia, respectively, $a = 1.43$ and $b = 1.47$ denote the distances from the vehicle's center of gravity to the front and rear axles, respectively. The states $\dot{x}_1$ and $\dot{x}_2$ denote the vehicle's longitudinal and lateral velocities, respectively, and $\dot{\psi}$ denotes the vehicle's yaw rate about the center of gravity. F_{x_1f} and F_{x_2f} are the forces of the front tire in the longitudinal and lateral axis, respectively, and F_{x_1r} and F_{x_2r} are the forces of the rear tire in the longitudinal and lateral axis, respectively.

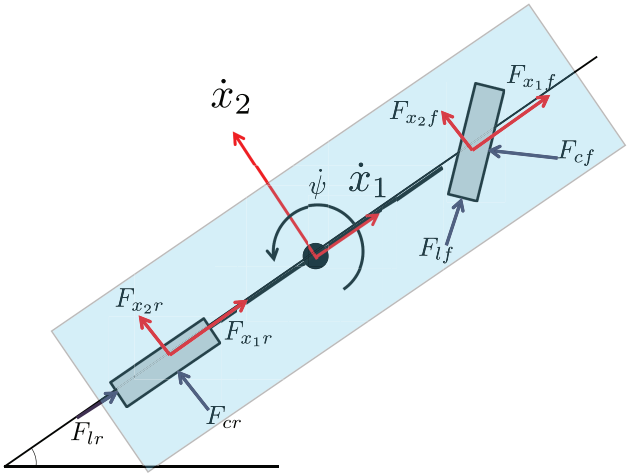

Figure 3.6: An illustration depicting the forces modeled in the vehicle body-fixed frame ($F_{x_1\star}$ and $F_{x_2\star}$), the forces in the tire-fixed frame ($F_{l\star}$ and $F_{c\star}$), and the rotational and translational velocities used in the vehicle model described in Equation (3.48).

The longitudinal and lateral tire force components in the vehicle body frame are modeled as:

$$\begin{aligned} F_{x_1\star} &= F_{l\star}\cos(u_\star) - F_{c\star}\sin(u_\star), \\ F_{x_2\star} &= F_{l\star}\sin(u_\star) + F_{c\star}\cos(u_\star), \end{aligned} \tag{3.49}$$

where $\star$ denotes f or r for the front and rear tire and $u_\star$ denotes the steering angle at the wheel. For this example, we assume only the front tire can be controlled, thus $u_f = u$ and $u_r = 0$. The longitudinal force in the tire frame is $F_{l\star} = 4269.125$. As described in [110], we model the dynamics as a hybrid system by splitting $F_{c\star}$,the force due to tire friction, into

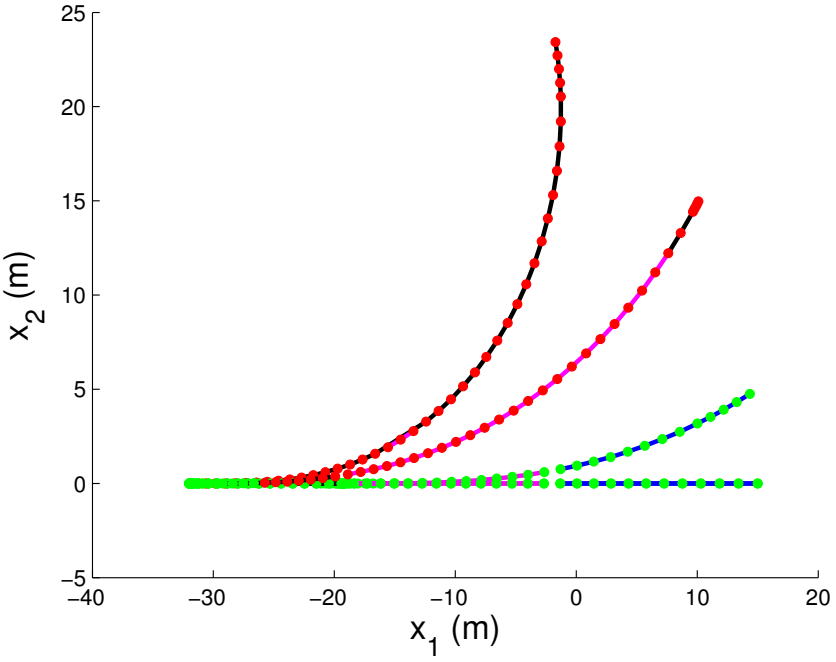

Figure 3.7: An illustration of four trajectories of the vehicle beginning at x_0 with constant input $-0.3, -0.2, -0.1$ and 0. The green dots on the trajectory denote states that when evaluated with respect to the computed w belonged to the 1-superlevel set. The red dots along the trajectory denote corresponding states that did not belong to the 1-superlevel set of w. Note that the trajectory with constant input 0.2 and 0.3, in contrast with the other two trajectories, has portions of its trajectory that are red. Portions of the trajectory drawn in black, magenta, and blue illustrate when the system was in mode 1, 2, and 3, respectively.

different zones depending upon the longitudinal velocity:

$$F_{c\star} = \begin{cases} -\frac{\dot{x}_2 + a\dot{\psi}}{18}, & \text{if } \dot{x}_1 \in [15, 21) \text{ - Mode 1} \\ -\frac{\dot{x}_2 + a\dot{\psi}}{24}, & \text{if } \dot{x}_1 \in [21, 27) \text{ - Mode 2} \\ -\frac{\dot{x}_2 + a\dot{\psi}}{30}, & \text{if } \dot{x}_1 \in [27, 33) \text{ - Mode 3} \end{cases}$$

For this example, we look at the forward reachable set of a vehicle beginning at x_0 which is equal to $x_1 = -32, x_2 = 0, \psi = 0, \dot{x}_1 = 15, \dot{x}_2 = 0$, and $\dot{\psi} = 0$ with the steering input u constrained to $[-0.1, 0.1]$. We use small angle approximations for the trigonometric terms in Equation (3.49). We compute the full forward reachable set, as illustrated in Figures 3.7 and 3.8, by running our degree 6 relaxation of our algorithm on the time-reversed dynamics and by solving the time-free backwards reachable set problem. Time to compute the BRS took 40min.

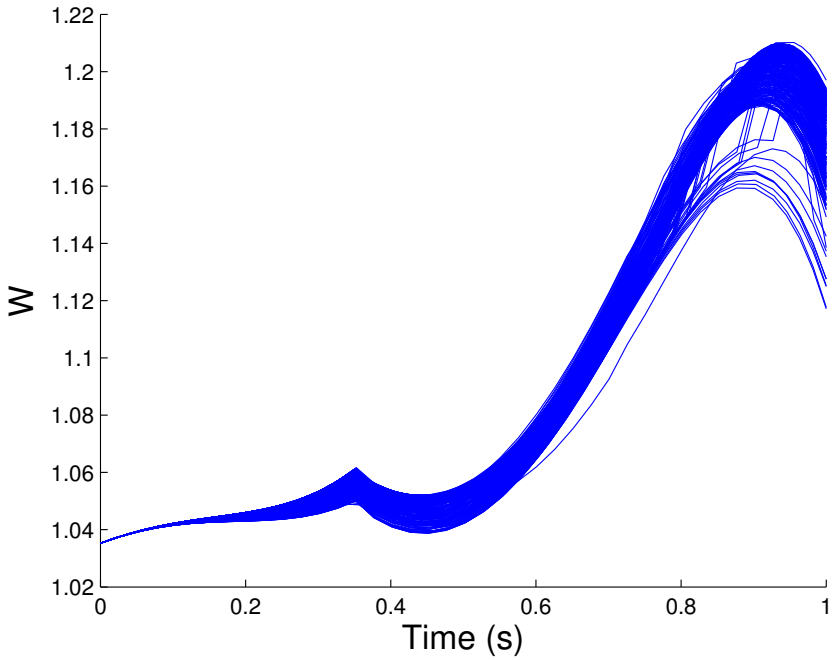

Figure 3.8: An illustration of the value of the computed w for different trajectories starting at x_0 with 200 distinct inputs all constrained to $[-0.1, 0.1]$. Notice that for all time, the value of w is greater than 1 indicating the trajectories lie in the forward reachable set.

Compass Gait

The compass gait (CG) walker is a simple model of legged locomotion consisting of two legs: one leg fixed to the ground called the stance leg, and one leg that swings called the swing leg and shown in Fig. 3.9. The CG is a one mode hybrid system in which the guard is reached

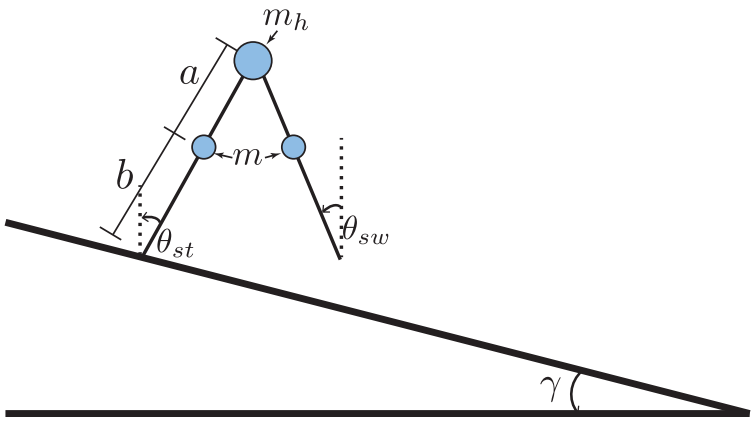

Figure 3.9: Schematic of the compass gait walker.

when the swing leg makes contact with the inclined plane, upon which the swing and stance leg switch. With different slopes and parameters, the CG has been found to reach a limit cycle consisting of 1, 2+ steps [111]. In this example, we consider a passive CG walker with no actuation. Let $\boldsymbol{\theta} = [\theta_{\text{sw}}, \theta_{\text{st}}]$ and $l = a + b$, the dynamics of the passive CG are given by:

$$M(\boldsymbol{\theta}, \dot{\boldsymbol{\theta}})\ddot{\boldsymbol{\theta}} + C(\boldsymbol{\theta}, \dot{\boldsymbol{\theta}})\dot{\boldsymbol{\theta}} + N(\boldsymbol{\theta}) = 0 \tag{3.50}$$

where

$$M(\boldsymbol{\theta}, \dot{\boldsymbol{\theta}}) = \begin{bmatrix} mb^2 & -mlb\cos(\theta_{\text{st}} - \theta_{\text{sw}}) \\ -mlb\cos(\theta_{\text{st}} - \theta_{\text{sw}}) & (m_h + m)l^2 + ma^2 \end{bmatrix} \tag{3.51}$$

$$C(\boldsymbol{\theta}, \dot{\boldsymbol{\theta}}) = \begin{bmatrix} 0 & mlb\sin(\theta_{\text{st}} - \theta_{\text{sw}})\dot{\theta}_{\text{st}} \\ mlb\sin(\theta_{\text{st}} - \theta_{\text{sw}})\dot{\theta}_{\text{sw}} & 0 \end{bmatrix} \tag{3.52}$$

$$N(\boldsymbol{\theta}) = \begin{bmatrix} mbg\sin(\theta_{\text{sw}}) \\ -(m_h l + ma + ml)g\sin(\theta_{\text{st}}) \end{bmatrix} \tag{3.53}$$

The guard is defined as when the swing leg hits the inclined slope and mathematically defined as:

$$G_{(1,1)} = \{(\boldsymbol{\theta}, \dot{\boldsymbol{\theta}}) \mid \theta_{\text{sw}} + \theta_{\text{st}} + 2\gamma = 0\}. \tag{3.54}$$

The reset map is given by:

$$R_{(1,1)}(\boldsymbol{\theta}^-, \dot{\boldsymbol{\theta}}^-) = \begin{bmatrix} \theta_{\text{st}} & \theta_{\text{sw}} & (Q_\alpha^+)^{-1} Q_\alpha^- \dot{\boldsymbol{\theta}}^- \end{bmatrix}' \tag{3.55}$$

where

$$Q_\alpha^- = \begin{bmatrix} -mab & -mab + (m_h l^2 + 2mal)\cos(2\alpha) \\ 0 & -mab \end{bmatrix} \tag{3.56}$$

$$Q_\alpha^+ = \begin{bmatrix} mb(b - l\cos(2\alpha)) & ml(l - b\cos(2\alpha)) + ma^2 + m_h l^2 \\ mb^2 & -mbl\cos(2\alpha) \end{bmatrix} \tag{3.57}$$

and $\alpha = \frac{\theta_{\text{sw}} - \theta_{\text{st}}}{2}$. The reset dynamics are derived using conservation of momentum resulting in a loss of kinetic energy. The loss of kinetic energy is recovered via change in potential energy as the CG walks down the slope.

Prior to [62] which presents an inner-approximation to the BRS, the BRS was limited to exhaustive simulation. However, [62] is limited to a small region and misses much of the BRS. For computation, we consider the 5th order Taylor approximation of the dynamics about the origin and a linearized reset map about the point where the limit cycle encounters the guard.

Figure 3.11 presents the polynomial degree 10 approximation to the backwards reachable set for the compass gait (with $\gamma = 0.05$) which is tasked with reaching within 0.001 of the limit cycle (in black) in $T = 1.5$ seconds with $m_h = 10$kg, $m = 5$kg, $a = b = 1$. Through simulation of 1.2 million randomly sampled points in the BRS, we find that 70% of the BRS reaches within 0.1 of the limit cycle.

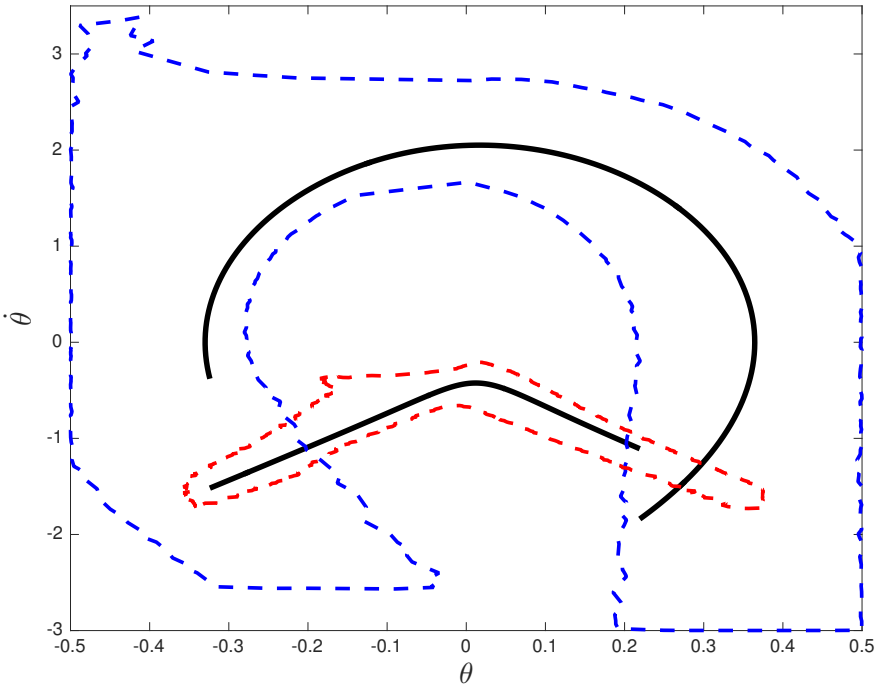

Figure 3.10: The finite time region of attraction for the compass gait's limit cycle shown in black (swing leg is the upper black cycle, stance leg is the lower black cycle). The blue region denotes the finite time region of attraction for the swing leg projected down to the $(\theta_{\text{sw}}, \dot{\theta}_{\text{sw}})$ domain. The red region denotes the finite time region of attraction for the stance leg projected down to the $(\theta_{\text{st}}, \dot{\theta}_{\text{st}})$ domain. The time horizon is 1.5s which allows trajectories to undergo two resets.

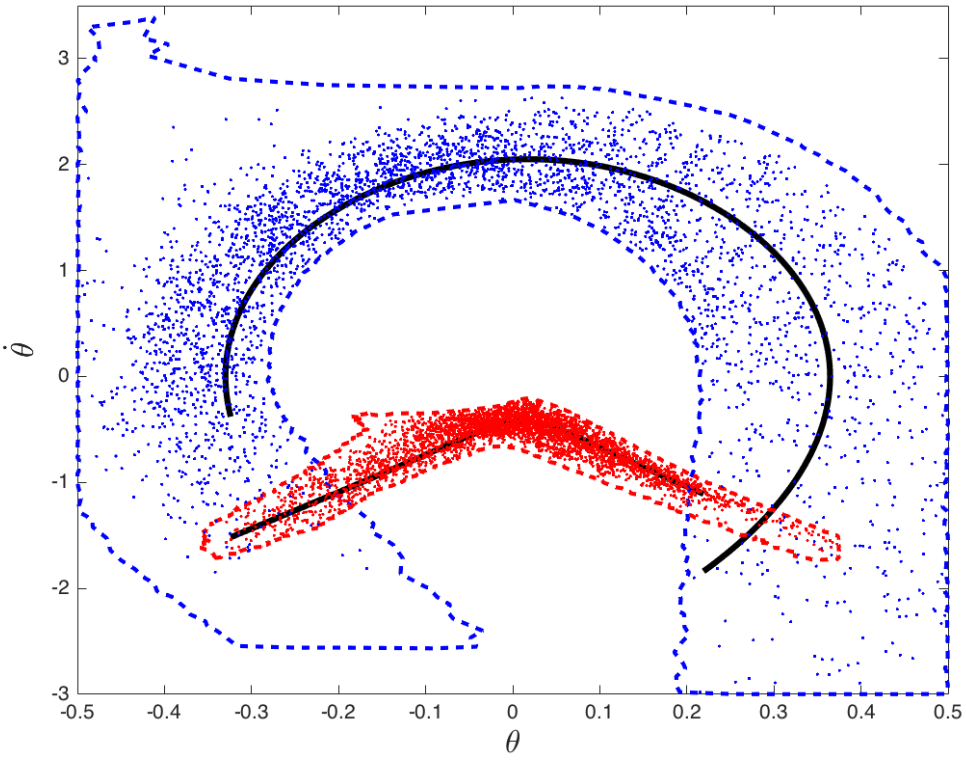

Figure 3.11: The finite time region of attraction for the compass gait with blue and red dots indicating sampled points which reach within 0.1 of the limit cycle after 1.5s. The blue region denotes the finite time region of attraction for the swing leg projected down to the $(\theta_{\text{sw}}, \dot{\theta}_{\text{sw}})$ domain. The red region denotes the finite time region of attraction for the stance leg projected down to the $(\theta_{\text{st}}, \dot{\theta}_{\text{st}})$ domain.

3.6 Conclusion

This chapter presents an approach for computing the BRS of a hybrid system using an infinite dimensional LP over the space of non-negative measures. Finite dimensional approximations to this LP in terms of SDPs were then constructed to obtain outer approximations of the BRS. In contrast to previous approaches relying on Lyapunov's stability criteria, our method is convex and does not require feasible initialization. The work in this chapter can be found in [63, 35]. Slight modifications to problem (D and D_k) were used to calculate the BRS for STS.

Chapter 4

Experiment

In this chapter, we describe the experimental protocol, data, and conduct a comparison to the existing biomechanical STS metric. All analysis was performed a system with an Intel Xeon E5-2680 2.70 GHz processor with 32 cores and 128GB RAM. The optimal control problem was solved using MATLAB's nonlinear solver *fmincon* [112]. The optimization problem (D) is solved using SPOTLESS [106] and MOSEK [107].

4.1 Experiments

From Chapter 3, we have an algorithm to determine the BRS or BOS for a dynamical system. In this section, we show how this algorithm is used to obtain the BOS for an individual's STS motion with the constructed controller. In order to test the utility of the BOS, there are certain properties the set must satisfy.

Property 1: *Slower motions are more stable than faster motions.*

Due to the time delay of the nervous system, many motor control researchers have hypothesized that the response of perturbations to fast motions is largely governed by reflex responses [113, 114]. Slower motions, in comparison, are long enough to allow a correcting response to perturbations. This hypothesis has been validated experimentally [115, 116, 117]. To validate Algorithm 1 experimentally, participating subjects were asked to perform STS in their natural manner, but at a fast and slow speed.

Property 2: *Quasi-static motions are more stable than momentum transfer motions.*

Property 2 is that the stability of the STS motion is governed by the strategy in which the subject stands. Two distinct methods of STS from a chair have been observed in the literature: momentum-transfer and quasi-static [118, 119, 120], shown in Figure 4.1. The momentum-transfer strategy consists of swinging one's trunk forward rapidly and undergoing a dynamically unstable transition phase to transfer the upper body forward momentum to stand up. The quasi-static strategy, in comparison, consists of moving one's center of mass (COM) over one's foot while sitting and using as little momentum as possible, then standing up. The motion is performed slowly and at any given point in time, the subject is statically stable. The momentum transfer strategy, in comparison, tends to be faster, requires more postural control [118], and uses less energy [121]. Therefore, we will evaluate the computed results from each stability metric as 'accurate' if the quasi-static strategy has a larger BOS than the dynamic strategy for the same individual. To validate Algorithm 1 experimentally, participating subjects were asked to perform STS quasi-statically and dynamically.

The trade-offs between each strategy are described below and summarized in Table 4.1. The momentum transfer strategy tends to be faster and more energy efficient, but is less stable. As a result, younger and healthier subjects typically stand up this way as they are able to easily adjust to perturbations. Due to the dynamic nature of the motion, the momentum transfer strategy requires fine postural and momentum control to ensure that the subject does not overshoot the standing position. On the other hand, by nature of moving one's COM over the BOS, the quasi-static strategy must be slower and is statically stable at

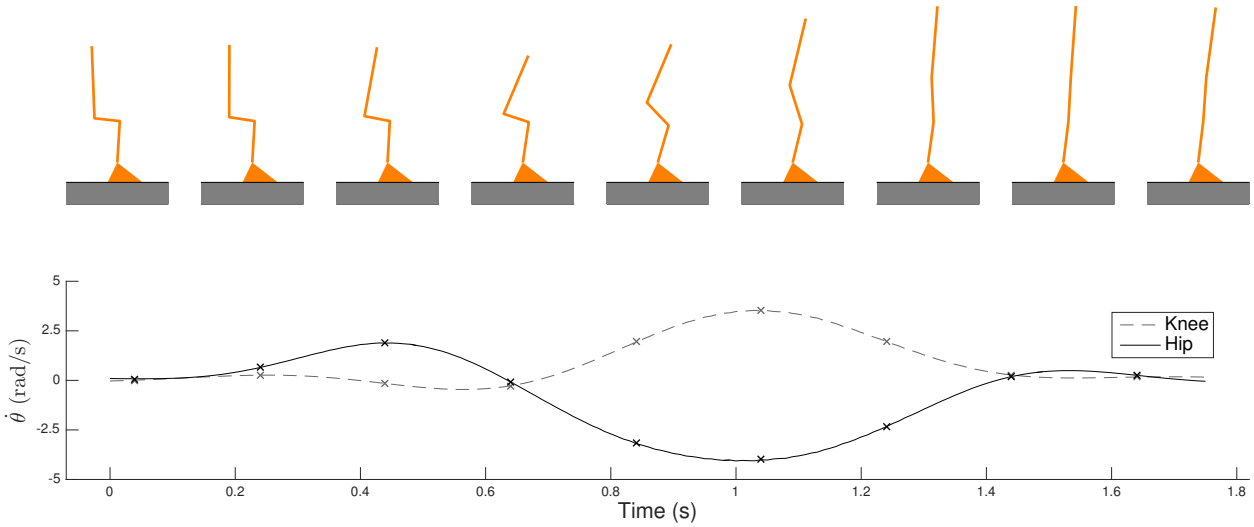

(a) Momentum Transfer STS Pictorially (orange) and velocity profile (bottom).

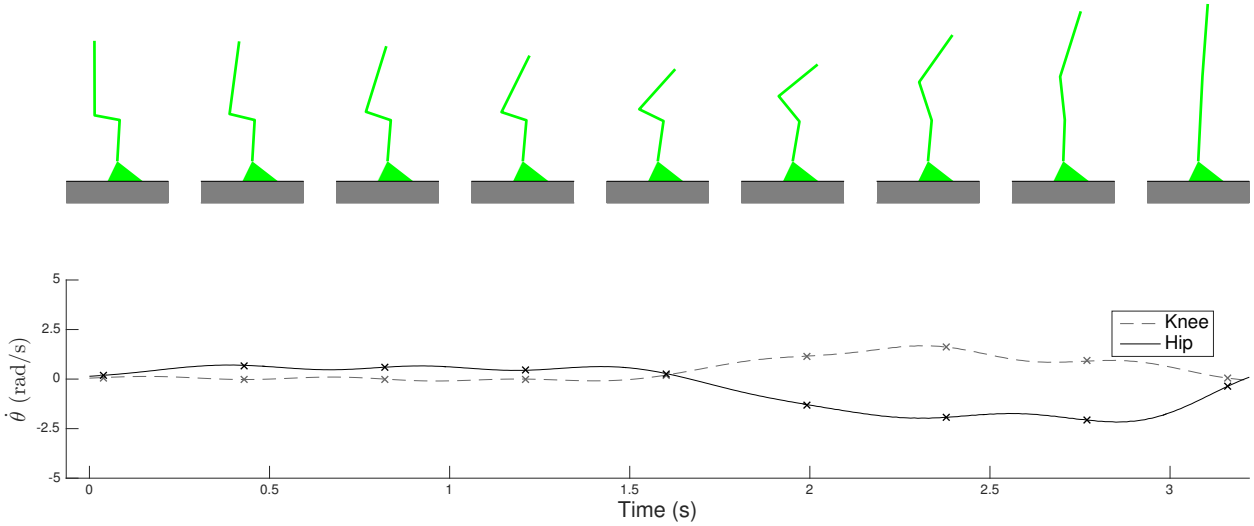

(b) Quasi-static STS Pictorially (green) and velocity profile (bottom).

Figure 4.1: Momentum-Transfer vs Quasi-Static STS Motions. Angular velocity of the ankle joint is negligible between the two motions and not shown.

all points in time. Among STS trials of an individual's motion, we expect the quasi-static strategy to have a larger BOS than the momentum transfer strategy.

Data Collection

Next we describe the data collection and experimental setup to verify both properties of our BOS. The experimental setup, shown in Figure 4.2, consists of an AMTI OPT464508

Momentum Transfer Strategy	Stabilization Strategy
Prioritizes energy efficiency	Prioritizes stability
Faster	Slower
Fast speed of trunk	Slow speed of trunk
Dynamically stable	Statically stable

Table 4.1: Comparison between STS strategies

force plate, 2 Microsoft HD webcams, and PhaseSpace Impulse X2 motion capture with 8 infrared cameras. Motion capture data was collected at 480Hz and the subject's skeleton was extracted using PhaseSpace's Recap2 software. All systems were time-synchronized using a Networked Time Protocol server running on the motion capture system. Ground reaction forces were collected at 2400Hz with the force place placed under the subject's foot[1]. Both the motion capture and force plate data were smoothed using a 4th-order Butterworth filter with a cut-off frequency of 2Hz. The chair height was adjusted such that the subject's thighs were parallel to the ground. Surrounding the chair were 6 inch memory foam mattresses as a safety precaution to cushion any falls.

Subjects wore a customized motion capture suit with 43 PhaseSpace markers placed on the suit according to the Recap2 software shown in Figure 4.3a. Subjects were asked to sit in a standardized posture with their trunk starting off vertical, thighs horizontal to the ground, arms crossed in front (constraining variability of the arms), and shank vertical to the ground.

We collected data from 2 cohorts[2]. The first cohort consisted of 10 young and healthy subjects with an average age of 26 and weight of 66kg. The second cohort consisted of 5 older and healthy subjects with an average age of 76 and weight of 71kg. Data for each subject is provided in Table 4.2. Subjects were asked to rise from the seat upon the researcher's command and asked to rise at a specific speed for the following STS strategies. Each STS strategy was performed 5 times consecutively.

1. Natural motion (untrained dataset)
2. Momentum transfer strategy (trained dataset)
3. Quasi-static strategy (trained dataset)
4. Starting off Bending (trained dataset)
5. Bordering Instability (called "unstable" for brevity)

[1]Force measurements were used to determine the start and end time of the STS motion

[2]This study was approved by the UC Berkeley Center for Protection of Human Subjects, Protocol #2015-07-7767

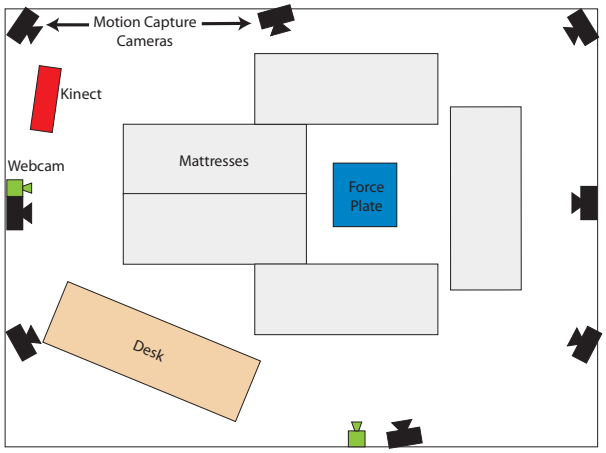

(a) Schematic of the room

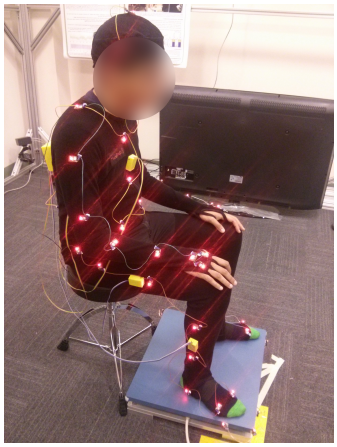

(b) Image with subject

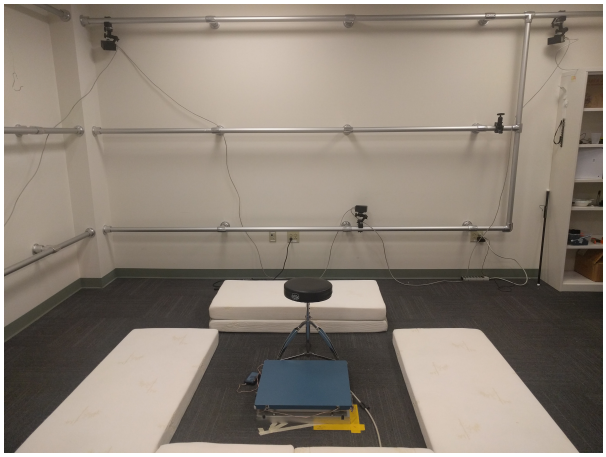

(c) View of chair from the front

(d) View of front room from the chair

Figure 4.2: Experimental Setup

To avoid biasing the subjects, we first asked the subjects to perform the STS motion naturally at a normal, fast, and slow speed. After, the subjects were asked to perform the momentum transfer and quasi-static in a random order. For consistency and to avoid individual interpretation of the motion, the subjects were shown videos demonstrating how to perform the momentum transfer and quasi-static strategy[3]. At the start and end of the experiment, the subjects were asked to perform a calibration phase which required them to rotate each joint, allowing the Recap software to fit an individualized skeleton to each subject.

[3]Videos can be found at: `www.w3id.org/people/vshia/jrsi/`

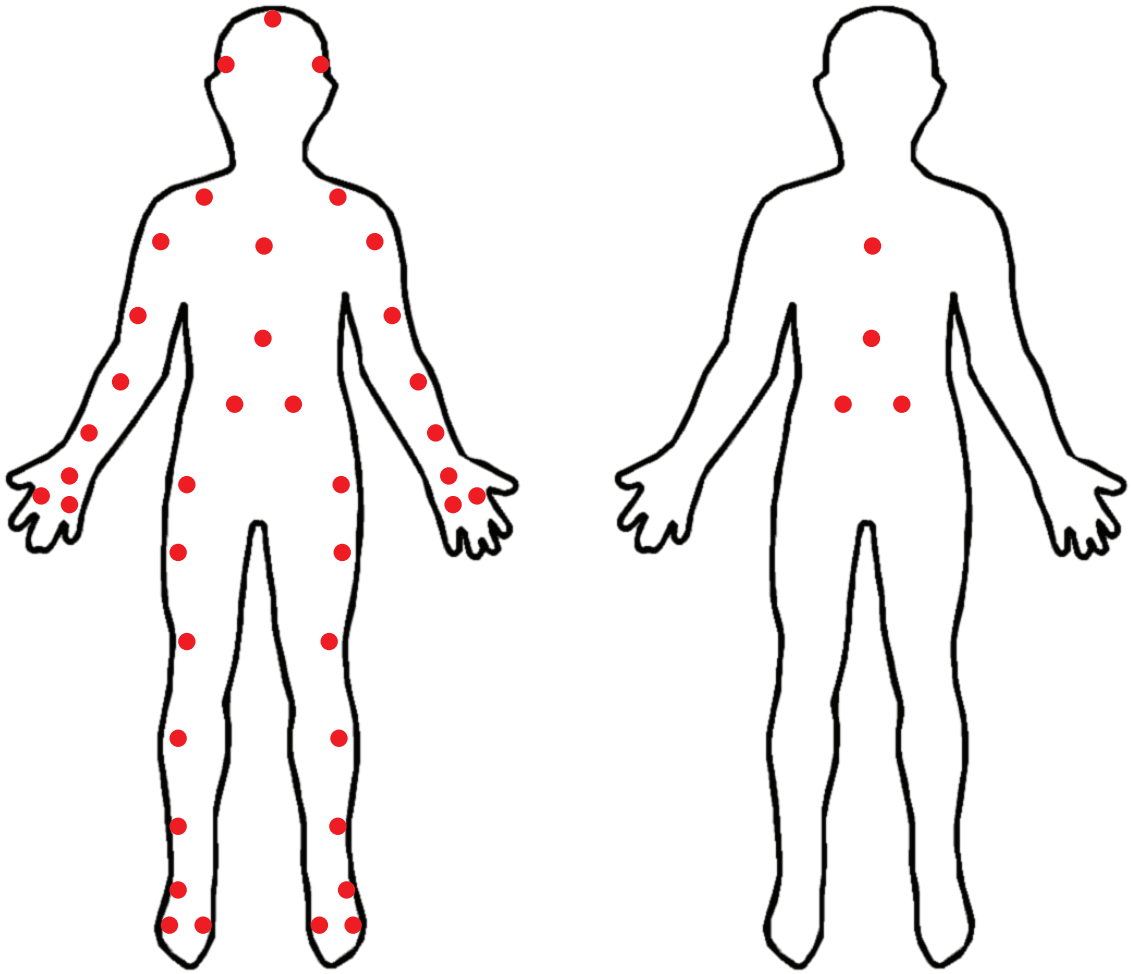

(a) Front View (b) Back View

Figure 4.3: Motion Capture Marker Placement

Group	ID	Gender	Age	Height (cm)	Weight (kg)
Young	1	F	23	153.7	70.3
	2	F	25	165.1	68.6
	4	M	37	184.2	74.0
	5	M	26	180.3	66.2
	6	F	22	165.1	58.7
	7	M	28	175.3	55.1
	8	M	29	175.3	79.8
	9	M	21	167.6	64.9
	14	F	25	160.0	54.2
	16	M	25	172.7	69.1
Older	3	F	84	162.6	65.3
	11	M	69	185.4	92.5
	12	M	77	170.2	66.2
	13	F	76	164.7	64.6
	15	M	74	175.3	69.1

Table 4.2: Data for each individual

	Natural (Untrained)	Momentum Transfer	Quasi-static	Bending	Unstable
Slow	x		x	x	
Normal	x	x	x	x	x
Fast	x	x		x	

Table 4.3: All STS motions and speeds collected

Type	Data type	Filename
Raw	Force plate	ForcePlate_XXX.mat
	Motion Capture	Mocap_XXX
	Kinect 2.0	kinect_XXX.txt
	Accelerometer	datalogXXX.csv
	Video	vid_XXX_*.mp4
Processed	C3D Motion Capture file	Mocap_XXX.c3d
	BVH Recap2 Skeleton	Mocap_XXX.bvh
	Kinect 2 Skeleton	kinect_XXX.mat

Table 4.4: Filenames for STS data where XXX denotes the STS motion.

1	2	3	4	5	6	7	8
Voltage high	Acc X	Acc Y	Acc Z	Moment X	Moment Y	Moment Z	Voltage low

Table 4.5: Force Plate Data Structure

4.2 STS Data

Here, we explain the raw and processed data which is generic and can be used by anyone interested in the data. Next, we explain how the data is processed for use in the framework.

The raw data is split up into 4 files and processed motion capture data into 2 files described in Table 4.4.

Generic Data

In this section, we describe the experimental data[4].

The force plate data is a MATLAB file consisting of the timestamps and data. The timestamps are in the MATLAB datenum time format[5]. Data is a $N \times 8$ array with the column descriptions listed in Table 4.5.

The motion capture data is saved in a text file delimited by spaces consisting of XYZ positions of 43 LED markers with the last two columns representing the timestamps in epoch time.

The kinect data consists of data to be processed by the MATLAB function: *get_skeleton_kinect2.m* which outputs a structure with the kinect data and timestamps.

The IMU data is stored in a csv file consisting of 37 columns: 36 columns of data and 1 column with timestamps shown in Table 4.6. The data consists of the XYZ readings from 4 gyroscope, accelerometer, and compass sensors. The timestamp is also in the MATLAB datenum time format.

The video data is saved as a standard mp4 video file.

[4]Data can be found on `www.w3id.org/people/vshia/jrsi/`

[5]`http://www.mathworks.com/help/matlab/ref/datenum.html`

Sensor 1									...	Sensor 4	Timestamp
Gyro			Acc			Compass					
X	Y	Z	X	Y	Z	X	Y	Z			

Table 4.6: Inertial Measurement Unit Data Structure

The C3D file is a standard processed motion capture file used and used with PhaseSpace Recap2 software. The BVH file is a standard skeleton filed outputted by the Recap2 software. The Kinect Matlab file is the processed Kinect data consisting of a structure array with all of the data.

Framework Data

First, we time synchronize the various forms of data based on the timestamps from all of the data. Next, we separate each STS trial using the event segmentation proposed in [122] and shown in Figure 4.4.

The STS motion in the sagittal plane is segmented into 6 events: Initiation, Counter, Seat-off, Vertical Peak, Rebound, and Standing. The STS motion begins with the initiation phase, which is defined at the point the subject begins to lean forward. The Initiation phase is followed by the Counter, which is when the subject's feet slightly lift off the ground. The Counter is followed by Seat-off which is when the subject's buttocks leaves the seat. The Vertical Peak is when the subject exerts the maximum downward force, which is followed by the Rebound, when the subject is fully extended with upward velocity, and ends with Standing. Each STS trial is defined by the Initiation to Standing events and is saved in a separate file containing all sensor data for the time duration of the STS trial.

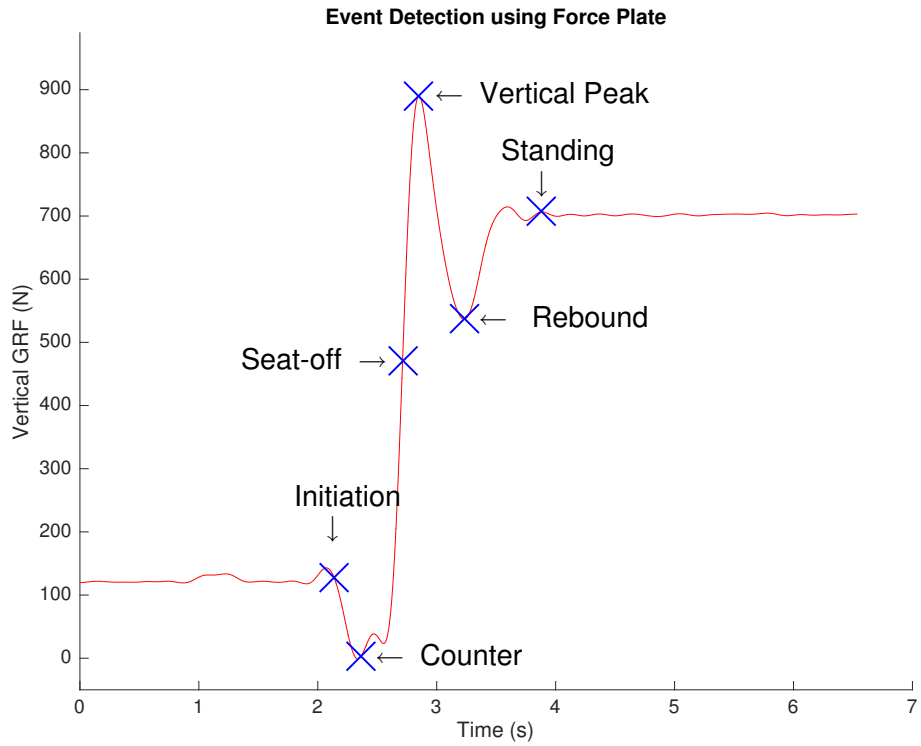

Figure 4.4: Force Plate Data with a single STS action.

4.3 Results using an existing stability metric

In this section, we will show the utility of looking at the trajectory of the STS motion by comparing the analysis to the metric proposed by Fujimoto et al [20]. Specifically, we analyze the ability of the STS volumes to quantify the BOS of slow vs fast and quasi-static vs momentum-transfer STS motions. Analysis was performed on a system with an Intel Core i7 processor and 32 GB RAM.

The model-based stability method proposed by Fujimoto et al consists of of two types of stability metrics [20]. These methods were chosen as they are the only-known model based method for determining the BOS of STS. The first metric, shown in Figure 4.5 called Region of Stability based on Velocity (ROSv), considers the normalized position and velocity of the patient's COM at the instance the patient lifts off the chair[6]. Points to the left (right) of the solid (dotted) line indicate initial positions and velocities in which it is infeasible for the subject to exert any type of torque to stand up. Specifically, points to the left of the solid line indicate initial conditions where the subject should fall backwards and points to the right of the dotted line, fall forwards. The second metric, shown in Figure 4.6 and called Region of Stability based on Acceleration (ROSa), considers the normalized position of the patient's COM at the instance the patient lifts off the chair and maximum normalized acceleration before the patient lifts off the chair[7].

The region of stability is defined as the region between the solid and dotted black line in Figures 4.5 and denotes all possible initial states where the patient theoretically can provide enough torque to stand up. If the subject's initial state lies left of the black line (right of the dotted line), the subject is guaranteed to fall backward (forward) unless he takes a step. The developers of the ROSv and ROSa metric correlate this distance with the likelihood of falling. The smaller the distance, the more likely the subject is to fall forward.

Figure 4.5 shows the average ROSv for subjects 1 to 16 summarized in Table 4.7. Figure 4.6 shows the average ROSa for subjects 1 to 16 summarized in Table 4.8. Notice that there are some initial conditions where the points lie to the left of the solid line yet all subjects were able to stand up successfully.

However, there are a few issues with this method. First, while the authors relate distance to the dotted line to the likelihood of falling forward, points closer to the solid line would be considered more stable and points to the left of the solid line should be considered very stable. However, this does not follow intuition as points left of the solid line should theoretically not be able to stand up. Rather, points of "maximum" stability should be located between the solid and dotted line. More importantly, summarizing the trajectory with a single feature loses information about the stability of the motion. To illustrate this issue, we look specifically at a subject in the young cohort (subject with ID 7) and in the older cohort (subject with ID 11) Figures 4.7 and 4.8 shows this analysis the individual in the young and elderly cohort[8]. Specifically, the younger subject slow natural STS has a smaller ROSv value

[6]Position normalized to the subject's foot length and velocity normalized to pendulum length / second
[7]Position normalized to the subject's foot length and acceleration normalized to pendulum length / second^2
[8]Figures for all subjects can be found at `www.w3id.org/people/vshia/jrsi`

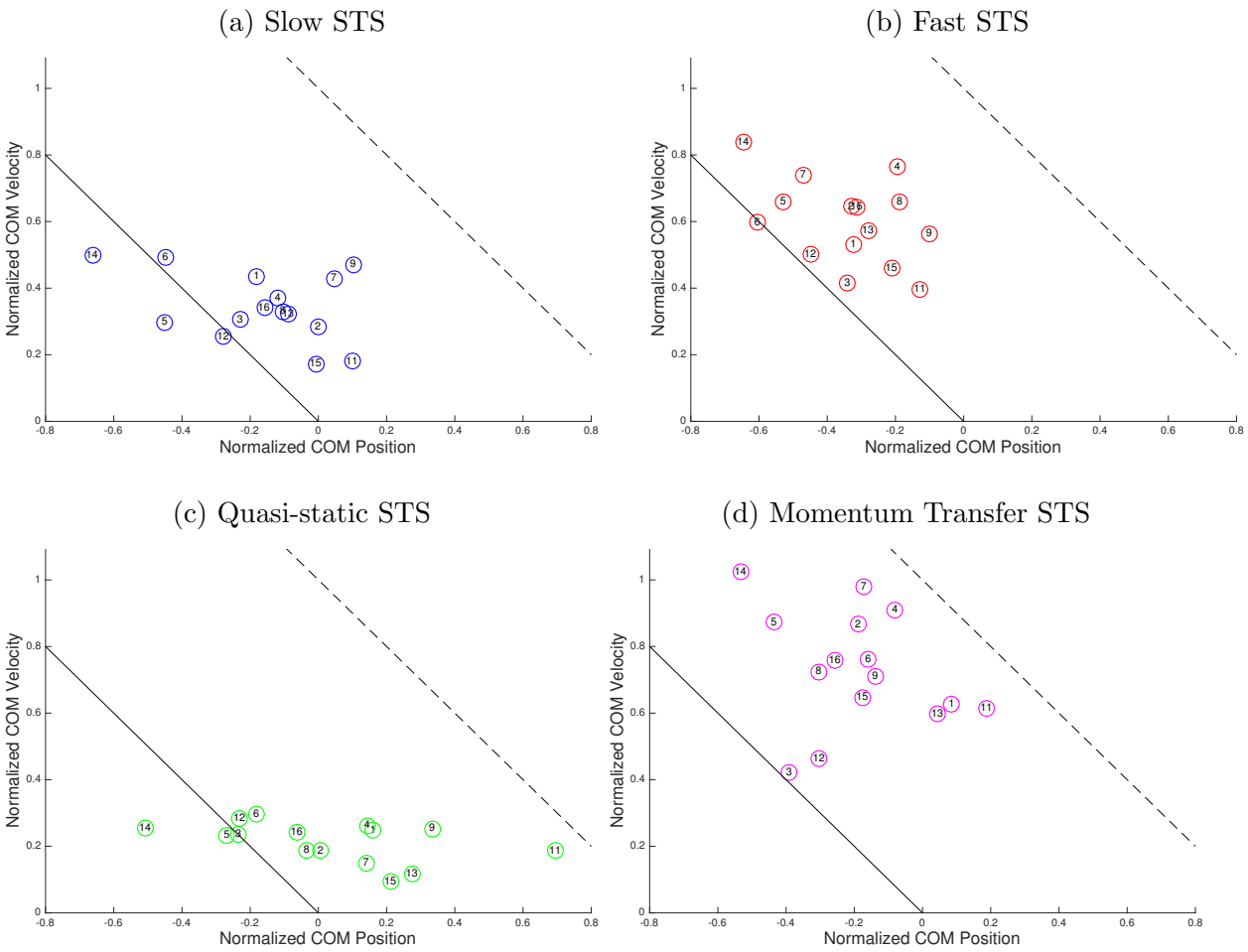

Figure 4.5: Median ROSv (across 5 trials per STS action) per subject. The subject ID is found in the circle. The BOS is the region between the solid and dotted black line.

than fast natural STS, indicating that slow natural STS is "less" stable than fast natural STS. For the older subject, the quasi-static STS has a smaller ROSv and ROSa value than momentum-transfer STS, indicating that quasi-static STS is "less" stable than momentum-transfer STS. Intuitively, this doesn't match what we expect to be true as slower motions should be more stable and able to handle larger perturbations than faster motions.

According to Table 4.7, ROSv shows that in the young cohort, the quasi-static method of standing is more stable than momentum transfer and that slow standing is more stable than fast standing. For all other categories, ROSv and ROSa are not consistent with what we expect to be true. These results, summarized in Table 4.17, highlight the deficiencies of summarizing the motion to a single feature.

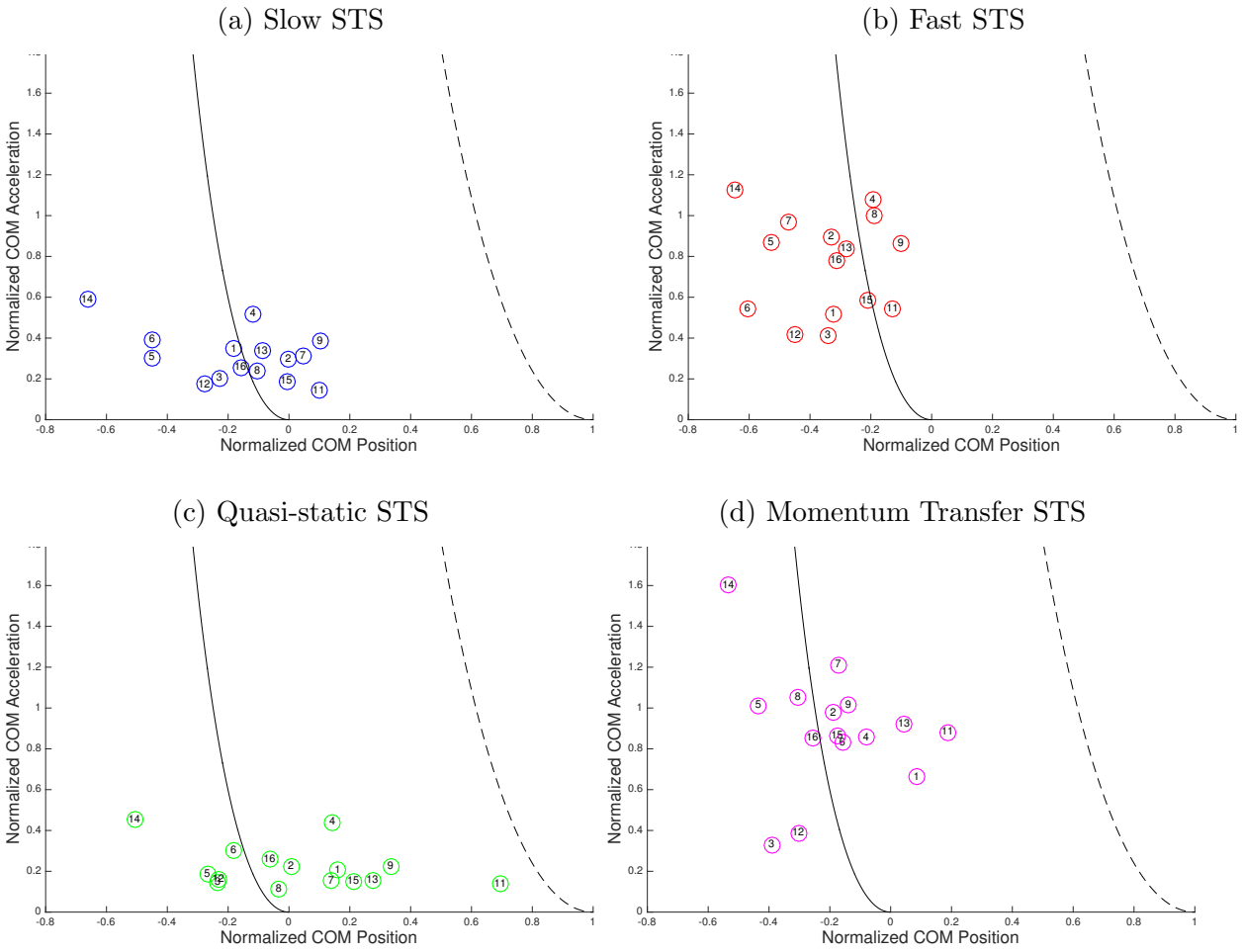

Figure 4.6: Median ROSa (across 5 trials per STS action) per subject. The subject ID is found in the circle. The BOS is the region between the solid and dotted black line.

Group	ID	Untrained Motion		Trained STS Strategy	
		Slow	Fast	Quasi-static	Momentum
Young	1	0.72	0.81	0.56	0.35
	2	0.74	0.70	0.81	0.30
	4	0.70	0.44	0.62	0.11
	5	1.13	0.85	1.03	0.64
	6	0.86	1.00	0.81	0.52
	7	0.56	0.72	0.68	0.23
	8	0.76	0.52	0.81	0.63
	9	0.45	0.48	0.43	0.47
	14	1.24	0.73	1.20	0.51
	16	0.82	0.67	0.86	0.50
Older	3	0.89	0.94	1.03	0.97
	11	0.73	0.73	0.12	0.20
	12	1.02	0.93	0.92	0.78
	13	0.75	0.71	0.62	0.32
	15	0.78	0.74	0.66	0.51

Table 4.7: Median ROSv value for each type of STS action for each subject. The ROSv value is the distance from the point in Figure 4.5 to the dotted line. The red cells highlight results contrary intuition.

Group	ID	Untrained Motion		Trained STS Strategy	
		Slow	Fast	Quasi-static	Momentum
Young	1	0.94	0.96	0.73	0.87
	2	0.72	0.75	0.61	0.72
	4	0.90	0.82	0.36	0.64
	5	0.86	0.95	1.07	1.01
	6	0.95	0.92	0.71	0.59
	7	0.64	0.90	0.43	0.70
	8	0.87	0.85	0.80	0.85
	9	0.73	0.71	0.43	0.57
	14	1.16	0.78	1.04	0.57
	16	0.99	0.78	0.90	0.74
Older	3	0.95	0.98	1.09	1.07
	11	0.80	0.84	0.14	0.57
	12	0.94	1.03	0.90	0.98
	13	0.77	0.96	0.43	0.81
	15	0.76	0.76	0.35	0.58

Table 4.8: Median ROSa value for each type of STS action for each subject. The ROSa value is the distance from the point in Figure 4.6 to the dotted curve. The red cells highlight results contrary to intuition.

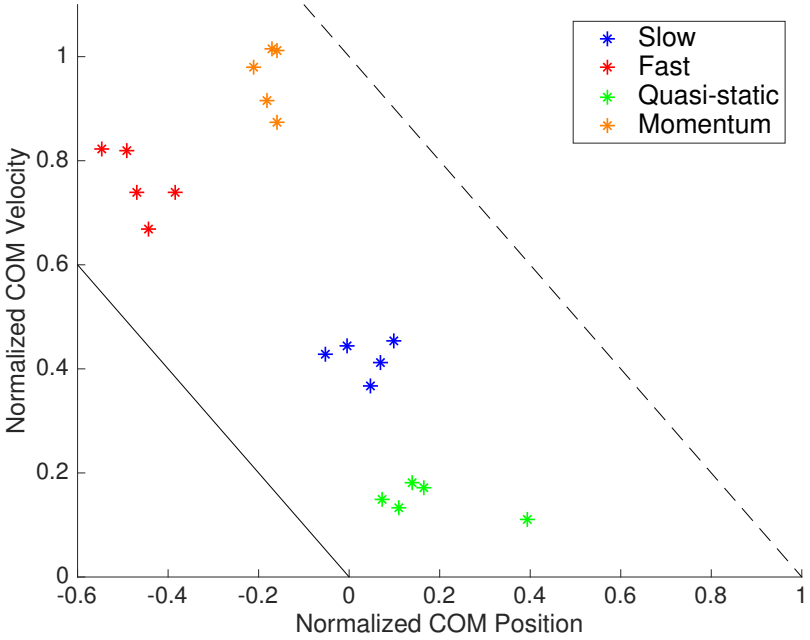

(a) ROSv - Young subject

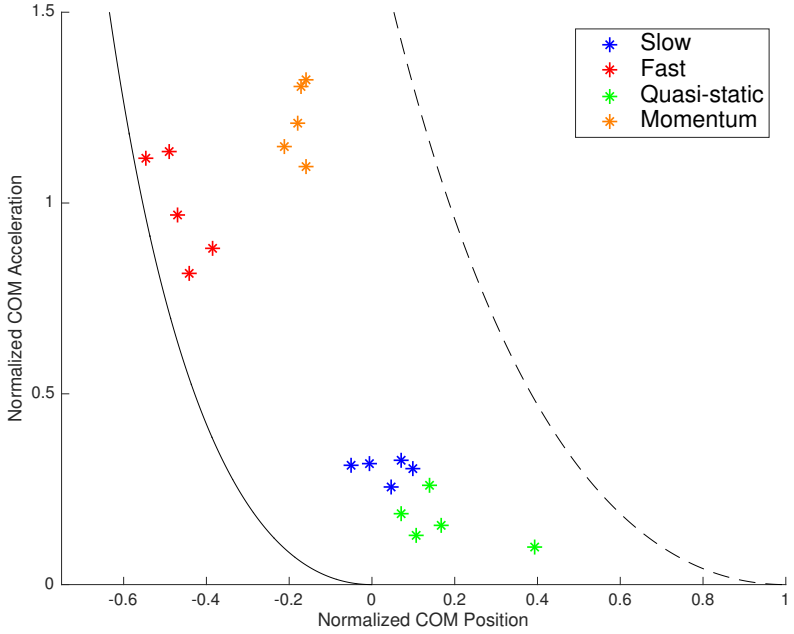

(b) ROSa - Young subject

Figure 4.7: ROSv and ROSa for different STS actions for a specific subject in the young cohort (ID 7). The stars denote the individual trials for each motion.

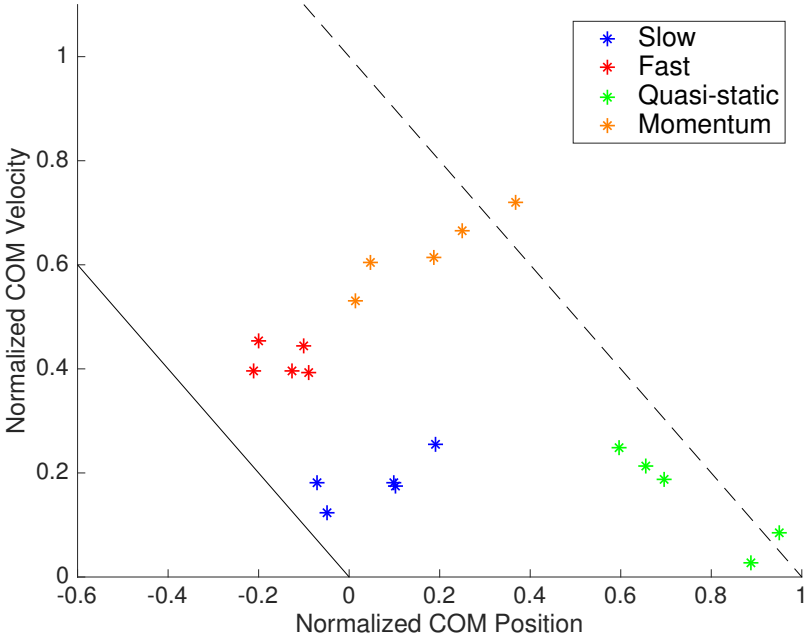

(a) ROSv - Older subject

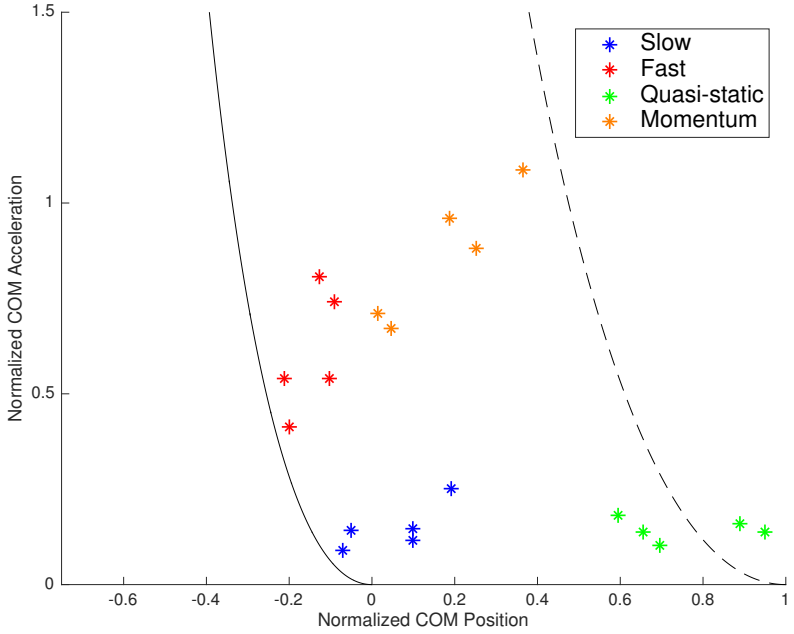

(b) ROSa - Older subject

Figure 4.8: ROSv and ROSa for different STS actions for a specific subject in the older cohort (ID 11). The stars denote the individual trials for each motion.

4.4 Reachability results for IPM

Using the proposed method in Chapter 2, the BOS for each individual's motion is computed for the IPM model. The purpose of this method is to quantify the amount of disturbance that a subject can handle and still stand up. The more disturbances the subject can handle, the more "stable" the subject is said to be. The model dynamics was approximated with a 5^{th} order Taylor expansion centered about the origin. The open loop feedback identification via optimal control was performed using 101 timesteps with a polynomial input of degree 6 and the optimization problem (D) was solved with a degree 14 polynomial. The computation time for entire pipeline for a single action was on average 211 seconds. To compare volumes of the computed BOS for trajectories of different time lengths, the computed volume is normalized with the volume of the domain. For example, 100% indicates that the entire domain (or all possible states and disturbances) is in the BOS and 0% indicates that the BOS is empty.

The median and maximum volumes for the computed BOS for all subjects are shown in Tables 4.9 and 4.10 and the proposed method correctly identifies stable and unstable motions according to the intuition developed in Section 4.1. As expected, motions that are intuitively more "stable" have a larger BOS volume demonstrating that these motions are more robust to perturbations. More importantly, these regions quantify the *amount* of perturbation the subject can reject to stand up.

Group	ID	Untrained Motion		Trained STS Strategy	
		Slow	Fast	Quasi-static	Momentum
Young	1	35.5	22.8	36.2	20.8
	2	43.1	17.1	46.7	16.7
	4	38.6	17.0	30.6	13.9
	5	37.7	18.2	38.1	19.7
	6	40.6	9.6	44.9	8.6
	7	31.3	16.7	37.5	14.9
	8	37.3	21.9	37.5	17.2
	9	35.4	18.7	38.5	14.4
	14	37.7	16.7	35.1	11.6
	16	36.1	10.7	39.1	8.8
Older	3	38.9	26.1	42.5	23.6
	11	40.4	21.1	45.9	14.6
	12	35.5	19.2	34.4	20.9
	13	51.3	23.1	52.9	10.1
	15	46.3	16.8	41.2	11.9

Table 4.9: **Median** percentage of the **computed** BOS for each type of STS action for the Inverted Pendulum Model.

Group	ID	Untrained Motion		Trained STS Strategy	
		Slow	Fast	Quasi-static	Momentum
Young	1	37.5	24.7	38.4	22.8
	2	44.2	24.7	49.6	34.0
	4	40.9	22.5	39.1	23.3
	5	38.8	24.1	40.6	21.0
	6	41.5	11.6	50.0	19.6
	7	31.8	20.6	38.6	16.2
	8	39.1	23.8	39.0	24.1
	9	36.6	19.3	42.0	16.7
	14	53.9	17.8	44.2	16.9
	16	36.5	11.8	39.5	14.2
Older	3	41.2	26.3	43.5	31.5
	11	47.3	21.7	46.2	20.9
	12	37.9	19.9	39.6	27.5
	13	52.2	36.0	53.4	22.1
	15	46.7	20.7	44.1	18.7

Table 4.10: **Maximum** percentage of the **computed** BOS for each type of STS action across the 5 trials for the Inverted Pendulum Model.

To compute the extent of the outer-approximation, we also found the BOS via simulation with results shown in Tables 4.11 and 4.12. The "true" BOS for each action matched intuition for every STS motion. The simulated BOS was on average 52% percentage smaller (11% std dev) than the computed BOS confirming that the computed BOS is indeed an outer-approximation.

Group	ID	Untrained Motion		Trained STS Strategy	
		Slow	Fast	Quasi-static	Momentum
Young	1	11.3	9.3	19.4	6.2
	2	16.0	7.4	34.3	8.3
	4	10.6	7.6	17.3	7.5
	5	15.9	7.5	25.9	8.7
	6	14.6	4.5	31.4	4.2
	7	13.7	7.8	27.4	7.8
	8	22.5	9.9	24.2	8.5
	9	18.0	8.6	28.0	7.2
	14	14.7	6.2	18.7	4.8
	16	18.1	4.8	28.0	5.4
Older	3	26.1	13.5	31.5	13.5
	11	27.4	9.4	33.2	7.1
	12	18.6	9.1	20.1	10.9
	13	29.0	10.4	42.3	5.9
	15	30.1	6.7	28.3	6.6

Table 4.11: **Median** percentage of the **simulated** BOS for each type of STS action for the Inverted Pendulum Model.

Group	ID	Untrained Motion		Trained STS Strategy	
		Slow	Fast	Quasi-static	Momentum
Young	1	18.3	10.6	28.1	9.3
	2	30.7	8.5	37.3	14.3
	4	18.3	9.4	23.9	10.2
	5	24.5	10.3	27.6	10.3
	6	21.2	5.3	35.5	7.0
	7	18.1	9.9	28.7	8.0
	8	23.0	11.3	26.7	11.1
	9	20.5	9.2	29.5	8.5
	14	16.2	6.5	23.4	5.8
	16	24.4	6.0	29.5	7.1
Older	3	27.2	13.9	31.5	17.2
	11	29.0	10.6	35.7	10.8
	12	20.7	10.1	25.1	12.5
	13	35.5	12.8	43.9	9.2
	15	31.8	7.6	32.8	8.6

Table 4.12: **Maximum** percentage of the **simulated** BOS for each type of STS action for the Inverted Pendulum Model.

To illustrate the utility of this metric, we consider the computed BOS for the same subjects presented in Section 4.3. Figure 4.9 shows the computed BOS of the younger subject, subject with ID 7. Figure 4.10 shows the computed BOS of the older subject, subject with ID 11. Both figures show that slow STS and quasi-static STS are able to handle more perturbations than fast STS and momentum-transfer STS, respectively.

(a) Young subject - Slow

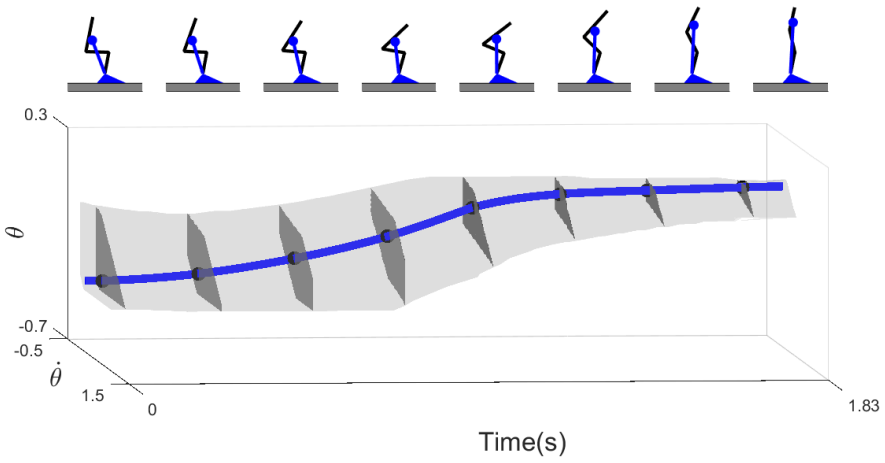

(b) Young subject - Fast

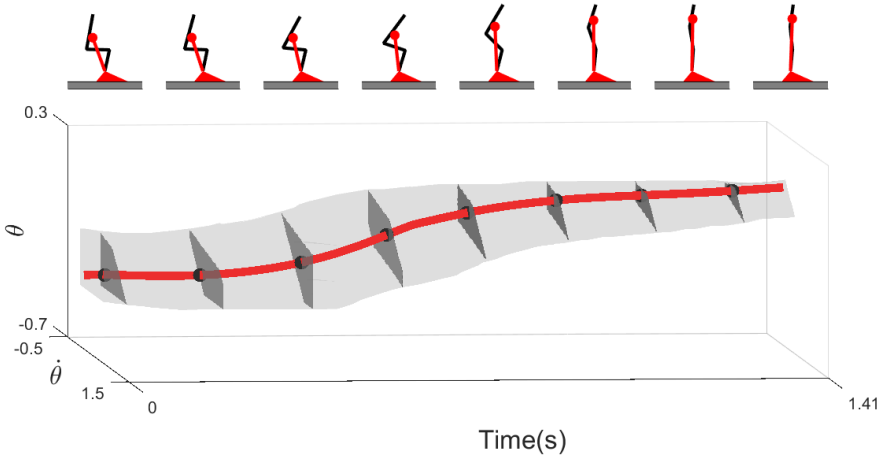

(c) Young subject - Quasi-static

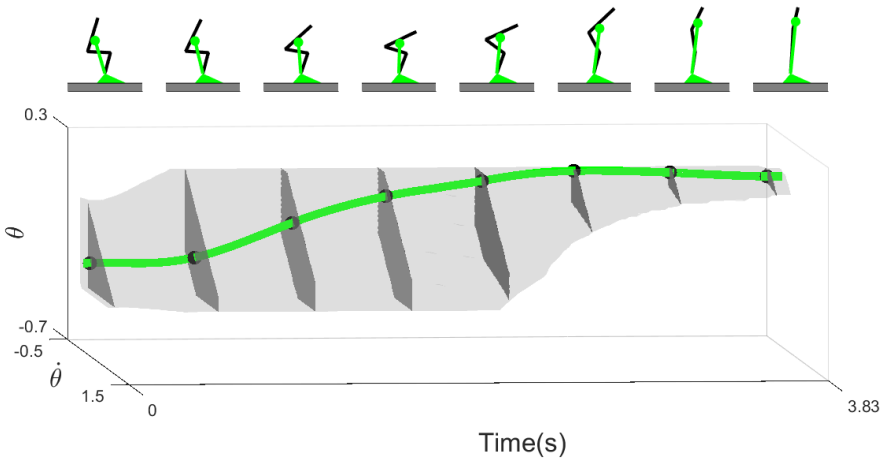

(d) Young subject - Momentum Transfer

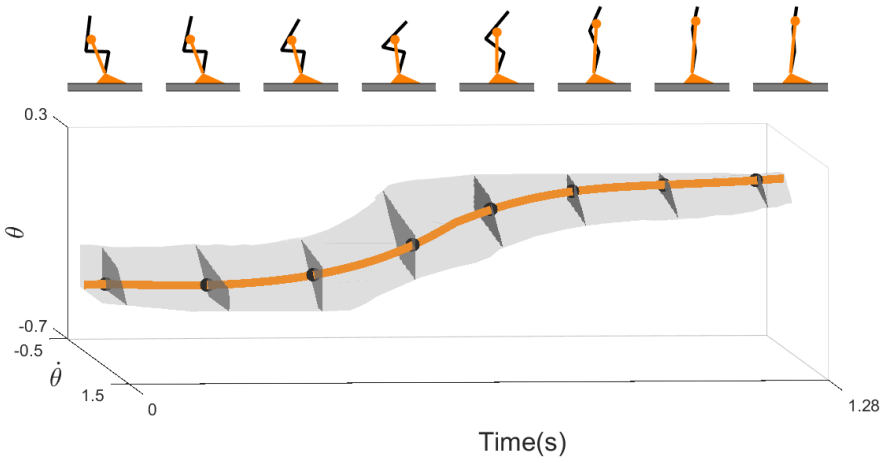

Figure 4.9: Proposed method for stability of different STS methods for subject 7. The gray skeleton represents the skeleton of the subject from the sagittal plane and non-gray color represents the IPM. The thick lines denote the observed trajectory ($y_{\text{obs}}(t)$) of the STS motion. The gray region denotes the computed BOS with time slices in dark gray with the intersection between the trajectory and slice in black and the corresponding position of the model above. Time is on the X-axis, angle from foot to COM on the Y-axis, and angular velocity on the Z-axis.

(a) Older subject - Slow

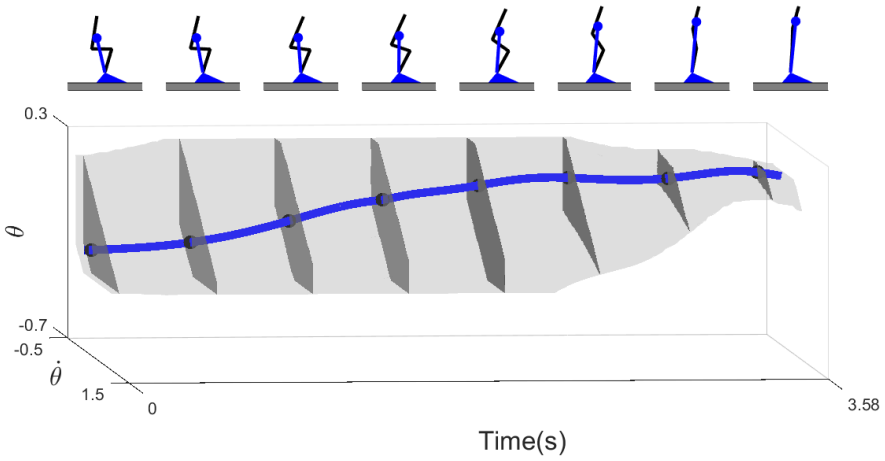

(b) Older subject - Fast

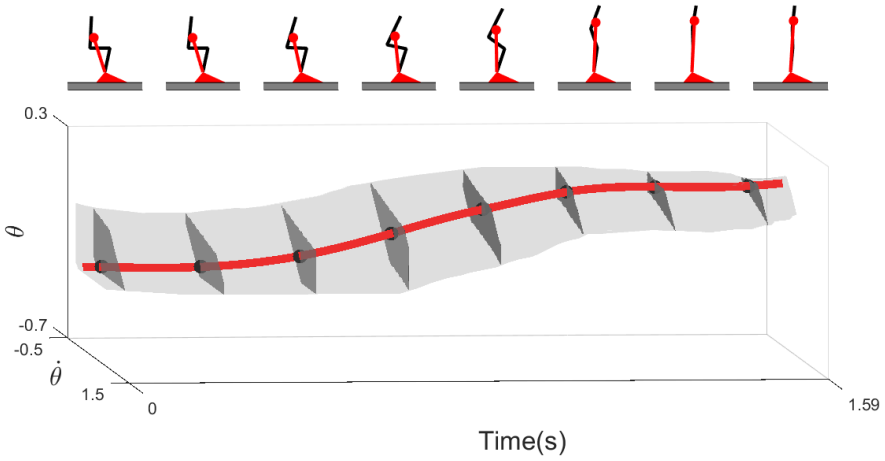

(c) Older subject - Quasi-static

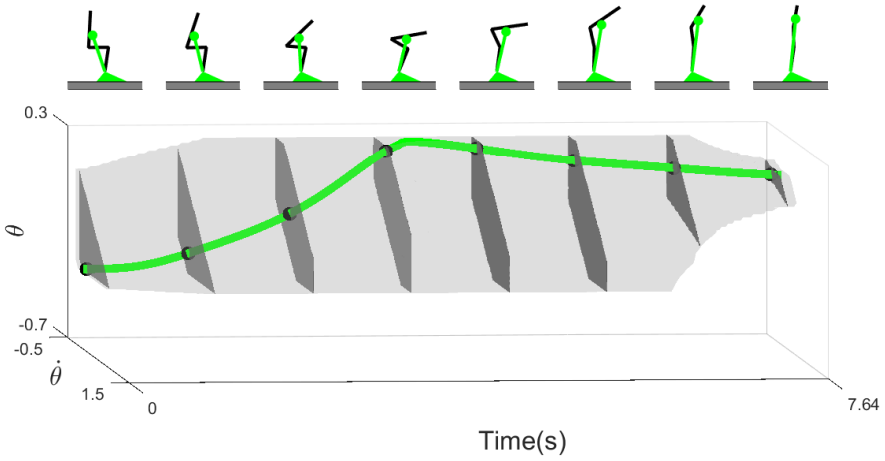

(d) Older subject - Momentum Transfer

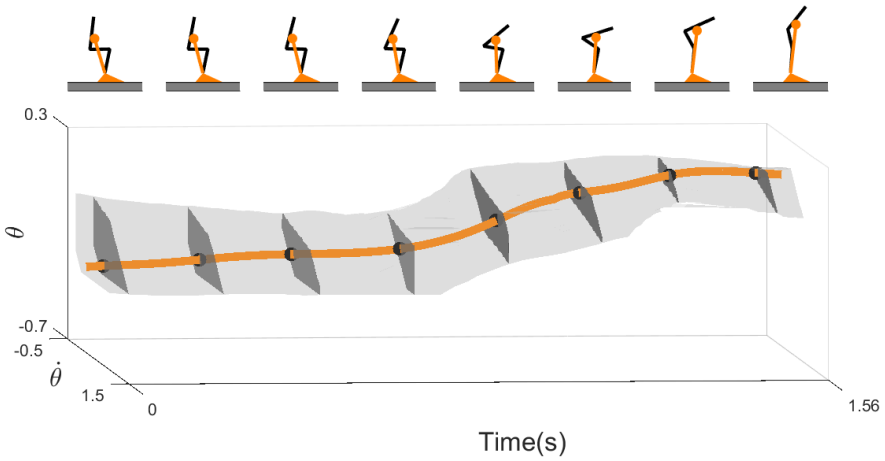

Figure 4.10: Proposed method for stability of different STS methods for subject 11. The gray skeleton represents the skeleton of the subject from the sagittal plane and non-gray color represents the IPM. The thick lines denote the observed trajectory ($y_{\text{obs}}(t)$) of the STS motion. The gray region denotes the computed BOS with time slices in dark gray with the intersection between the trajectory and slice in black and the corresponding position of the model above. Time is on the X-axis, angle from foot to COM on the Y-axis, and angular velocity on the Z-axis.

The IPM model itself is not without limitations however. First, the IPM assumes the STS can be modeled via the center of mass while sitting and standing. Second, while Patton et al used theoretical values for the input bounds [18], it is unknown how to convert strength values from the full body to input bounds for the model. Third, only the sagittal plane is considered. Finally, this assumes that foot placement is static and the feet are not moved to position underneath the chair in a more stable manner. Despite these limitations, we believe these results are promising for demonstrating the utility of the BOS. To address a few of these limitations, a higher order model is required and in the next section, the results for the double pendulum model are presented.

4.5 Reachability results for DPM

In this section, the BOS for each individuals motion is computed for the DPM model to determine the effect of using a model that more accurately reflects the morphology of an individual. The model dynamics were approximated with a 4^{th} order Taylor expansion. The optimal control was performed using 101 timesteps with a polynomial input of degree 4 and the optimization problem (D) was solved with a degree 8 polynomial. The computation time for entire pipeline for a single action was on average 4130 seconds.

The median and maximum volumes for the computed BOS for all subjects are shown in Tables 4.13 and 4.14 and show that the proposed method correctly identifies stable and unstable motions. As expected, motions that are intuitively more "stable" have a larger BOS volume demonstrating that these motions are more "robust" to perturbations. More importantly, these regions quantify the *amount* of perturbation the subject can reject to stand up. The red cells in Table 4.14 corresponds to volumes which are contrary to expectation which, when looking at the simulated BOS, is a result of the outer-approximation of the method.

Group	ID	Untrained Motion		Trained STS Strategy	
		Slow	Fast	Quasi-static	Momentum
Young	1	16.9	11.4	20.8	11.1
	2	20.2	10.1	26.1	16.5
	4	12.0	9.4	15.3	10.0
	5	9.9	7.9	14.0	8.0
	6	17.3	15.7	23.0	12.4
	7	17.5	11.5	18.9	12.2
	8	11.3	7.6	13.8	6.5
	9	21.2	15.8	25.1	19.7
	14	25.1	12.8	26.1	11.7
	16	13.4	8.3	15.3	10.7
Older	3	35.9	29.6	33.0	27.2
	11	23.5	20.1	28.2	26.3
	12	8.4	5.8	9.4	6.6
	13	17.6	15.2	26.3	12.9
	15	21.9	10.6	19.5	10.4

Table 4.13: **Median** percentage of the **computed** BOS for each type of STS action for the Double Pendulum Model.

Group	ID	Untrained Motion		Trained STS Strategy	
		Slow	Fast	Quasi-static	Momentum
Young	1	17.5	12.6	23.9	12.7
	2	23.7	19.7	29.0	24.1
	4	14.0	10.8	16.1	14.1
	5	13.4	8.9	16.5	8.1
	6	19.9	20.5	24.7	12.9
	7	19.3	16.8	20.8	12.8
	8	18.7	8.6	16.0	8.2
	9	27.7	20.0	27.9	21.3
	14	26.3	20.0	27.6	13.9
	16	16.8	10.0	17.4	12.4
Older	3	38.2	32.6	36.8	31.6
	11	37.7	33.2	28.6	28.8
	12	9.8	8.2	17.0	6.9
	13	19.9	20.7	27.7	16.7
	15	26.5	17.0	21.0	12.9

Table 4.14: **Maximum** percentage of the **computed** BOS for each type of STS action for the Double Pendulum Model.

To compute the extent of the outer-approximation, we also found the BOS (via a simulation of 175k points sampled uniformly) with results shown in Tables 4.15 and 4.16. The "true" BOS for each action matches intuition for every STS motion. The simulated BOS was on average 41% percentage smaller (16% std dev) than the computed BOS confirming that the computed BOS is indeed an outer-approximation.

Group	ID	Untrained Motion		Trained STS Strategy	
		Slow	Fast	Quasi-static	Momentum
Young	1	9.0	3.8	11.7	4.1
	2	14.8	4.4	20.4	8.6
	4	6.6	3.3	10.2	4.6
	5	4.8	1.1	6.5	1.6
	6	6.9	3.9	15.2	2.5
	7	7.8	2.3	9.4	2.0
	8	6.3	2.3	7.7	1.8
	9	10.0	5.7	13.0	7.5
	14	13.0	3.2	16.5	2.8
	16	9.7	3.0	10.7	4.4
Older	3	17.5	9.9	16.5	6.9
	11	12.7	6.0	13.8	8.1
	12	3.2	1.0	3.6	1.7
	13	13.7	4.9	18.7	3.5
	15	15.1	3.6	12.3	3.8

Table 4.15: **Median** percentage of the **simulated** BOS for each type of STS action for the Double Pendulum Model.

Group	ID	Untrained Motion		Trained STS Strategy	
		Slow	Fast	Quasi-static	Momentum
Young	1	9.4	4.6	12.9	5.0
	2	19.4	9.4	22.2	10.4
	4	7.9	3.9	10.6	8.0
	5	5.2	2.2	8.1	1.8
	6	13.8	4.9	17.2	4.5
	7	9.7	5.9	11.2	4.1
	8	9.7	2.5	9.2	2.6
	9	15.3	6.7	14.2	9.3
	14	14.9	4.4	17.1	4.5
	16	11.3	4.1	13.3	5.2
Older	3	18.2	12.3	17.6	9.4
	11	23.1	14.9	15.1	12.9
	12	3.4	1.8	7.0	2.2
	13	15.0	8.3	19.7	5.2
	15	16.2	6.0	14.0	5.1

Table 4.16: **Maximum** percentage of the **simulated** BOS for each type of STS action for the Double Pendulum Model.

To illustrate the utility of this metric, we consider the computed BOS of subjects 7 and 11, the same subjects presented in Section 4.3[9]. Figure 4.11 shows the computed BOS of the younger subject, subject 7. Figure 4.12 shows the computed BOS of the older subject, subject 11. Both figures show that slow STS and quasi-static STS are able to handle more perturbations than fast STS and momentum-transfer STS, respectively.

The DPM model itself is also not without limitations however. While the DPM improves upon the IPM by separating the body center of mass into the upper and lower body masses, the model collapses the shank and thigh (lower and upper leg) into one link. However, by separating the upper body, the model is able to account for the fact that the upper body is more stable when the subject is sitting down and the input bounds for the upper body correlate more with actual physical limits. Second, only the sagittal plane is considered. Finally, this assumes that foot placement is static and the feet are not moved to position underneath the chair in a more stable manner.

[9]Figures for all subjects can be found at `www.w3id.org/people/vshia/jrsi/`.

(a) Young subject - Slow

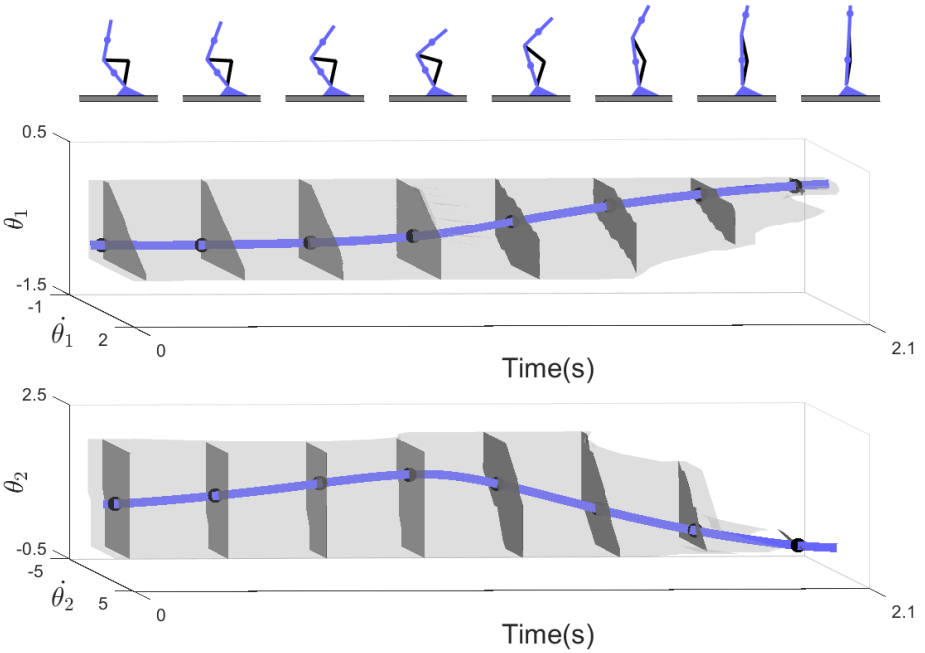

(b) Young subject - Fast

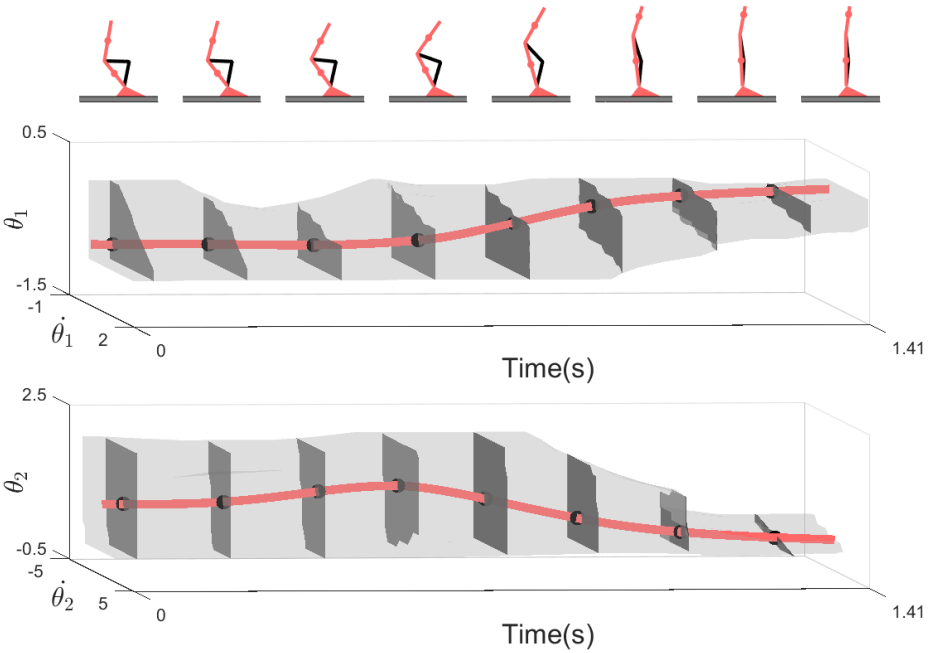

(c) Young subject - Quasi-static

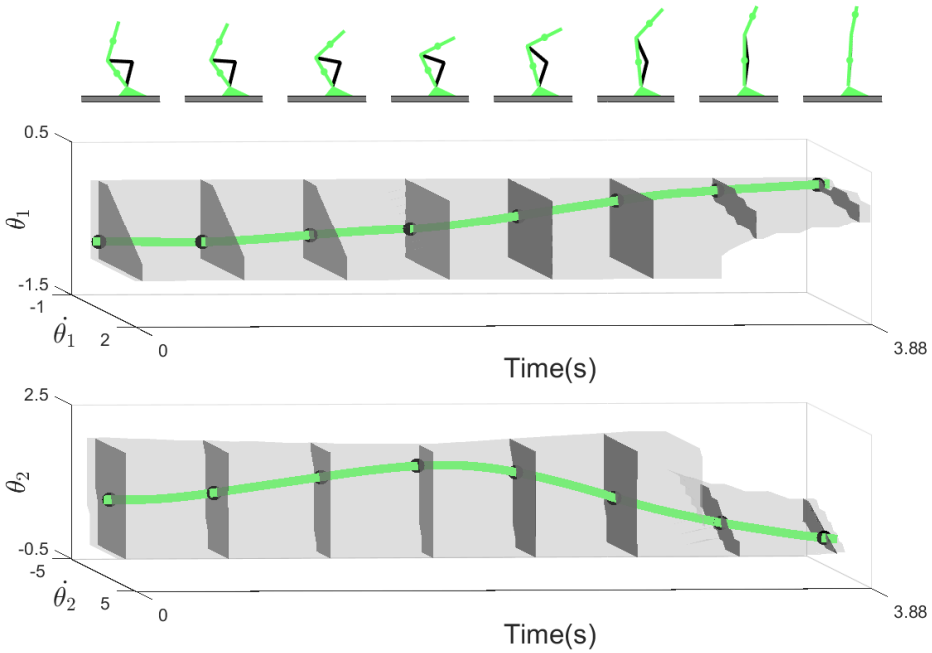

(d) Young subject - Momentum Transfer

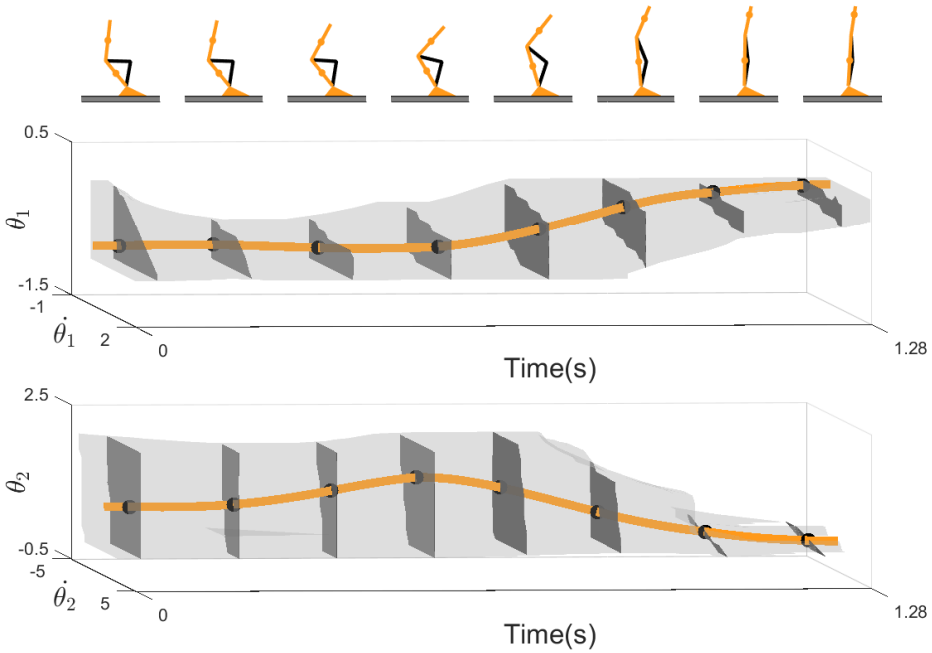

Figure 4.11: Proposed method for stability of different STS methods for subject 7. The gray skeleton represents the skeleton of the subject from the sagittal plane and non-gray color represents the DPM. The thick lines denote the observed trajectory ($y_{\text{obs}}(t)$) of the STS motion. The gray region denotes the computed BOS with time slices in dark gray with the intersection between the trajectory and slice in black and the corresponding position of the model above. Time is on the X-axis, angle from foot to COM on the Y-axis, and angular velocity on the Z-axis.

(a) Older subject - Slow

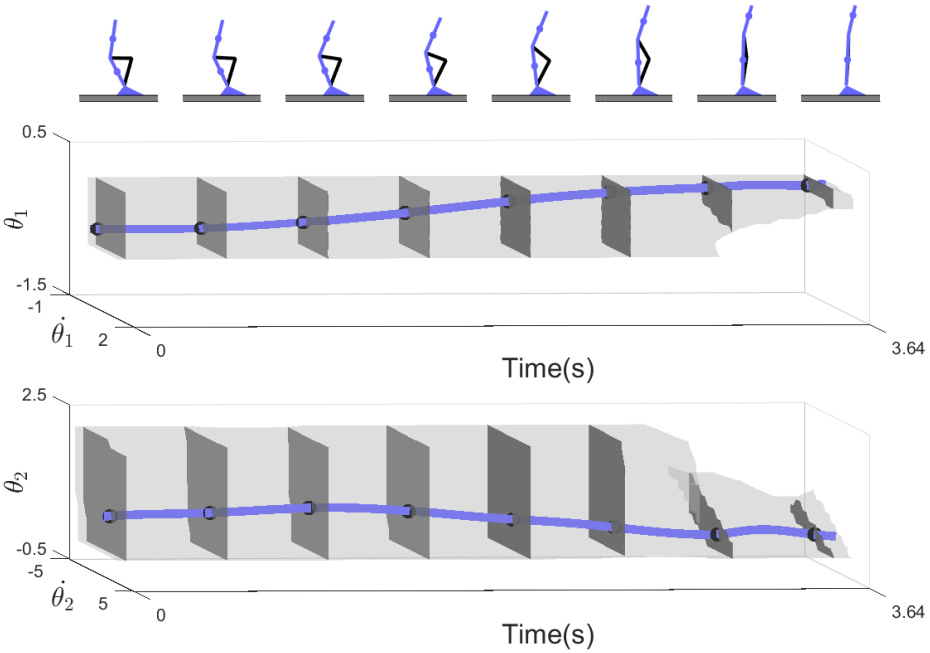

(b) Older subject - Fast

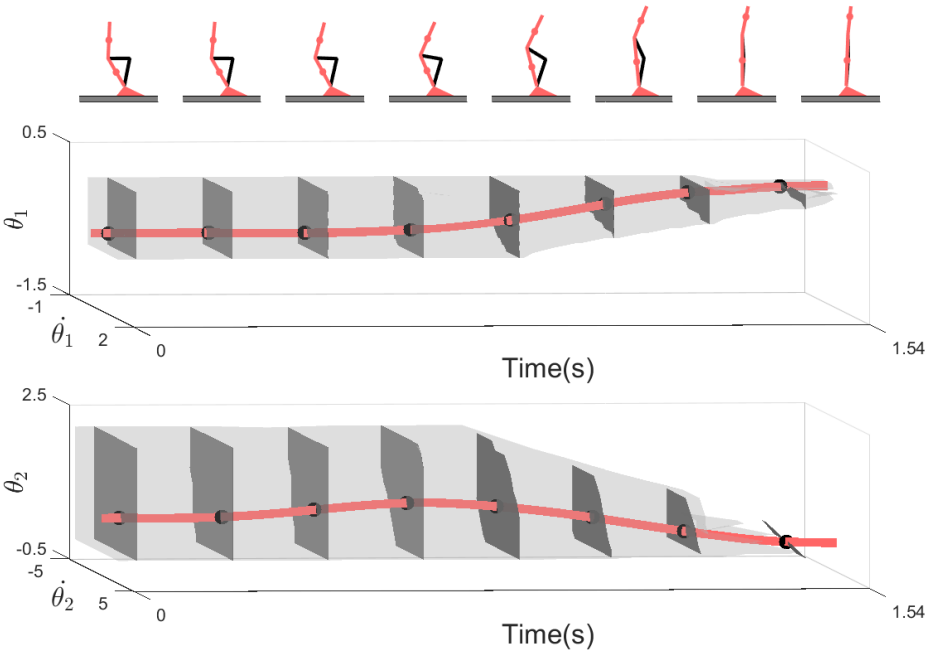

(c) Older subject - Quasi-static

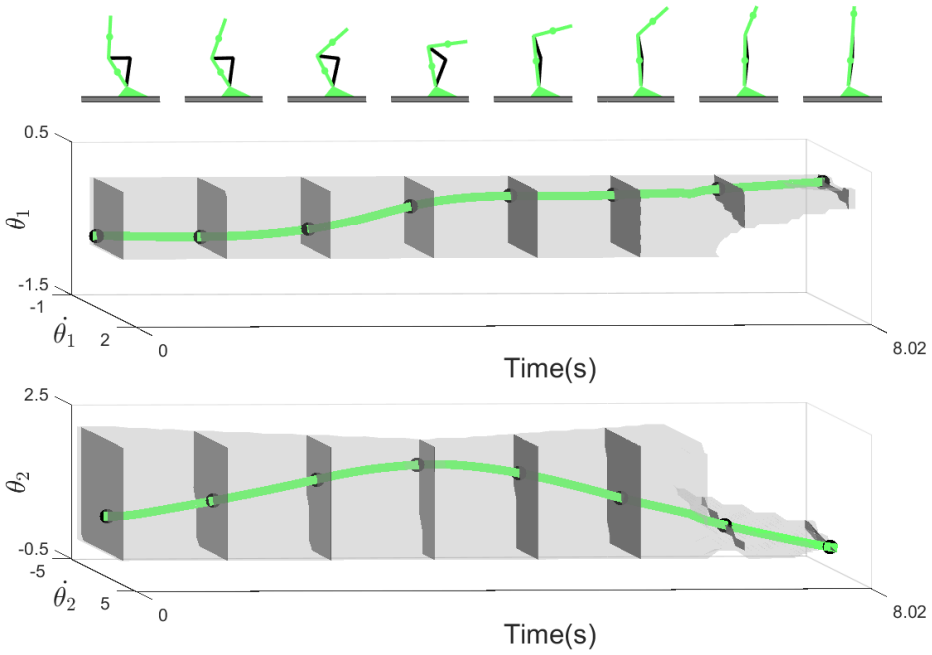

(d) Older subject - Momentum Transfer

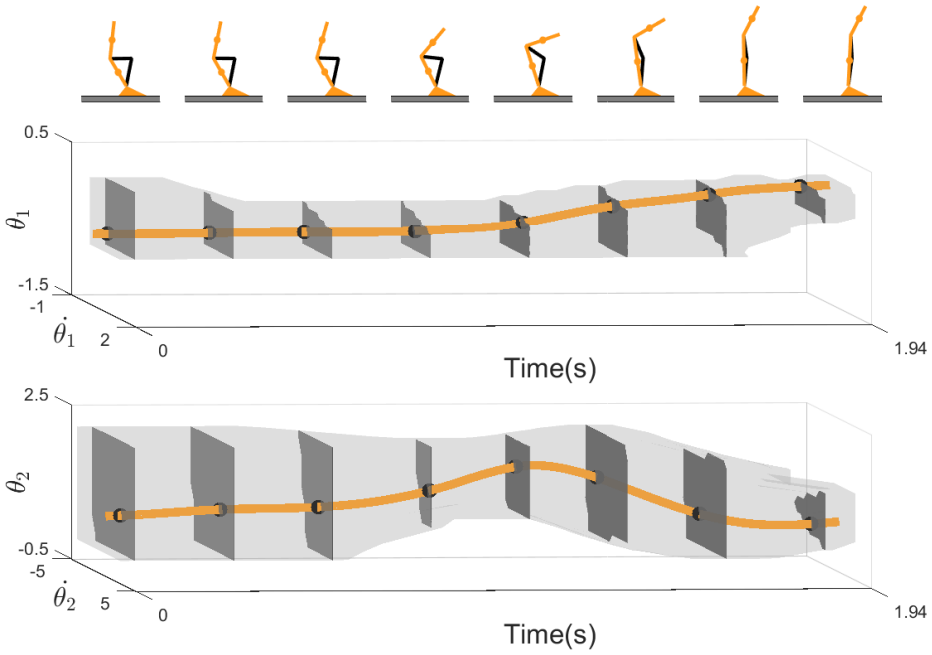

Figure 4.12: Proposed method for stability of different STS methods for subject 11. The gray skeleton represents the skeleton of the subject from the sagittal plane and non-gray color represents the DPM. The thick lines denote the observed trajectory ($y_{\text{obs}}(t)$) of the STS motion. The gray region denotes the computed BOS with time slices in dark gray with the intersection between the trajectory and slice in black and the corresponding position of the model above. Time is on the X-axis, angle from foot to COM on the Y-axis, and angular velocity on the Z-axis.

Comparison of metrics and models

In this subsection, we compare the metrics and the models. According to Table 4.17, the metric in [20] is unable to distinguish the expected stability characteristics for each motion. On the other hand, our proposed metric correctly distinguishes the expected stability results for each motion 95% or higher. For each subject, according to Tables 4.9 and 4.13, the computed BOS for slow standing is larger than fast standing and the BOS for the quasi-static method is larger than the momentum-transfer method.

Table 4.18 and 4.19 shows the side-by-side comparison of Fujimoto's metric and the proposed metric for subjects 7 and 11, the younger and older subject respectively. According to Fujimoto's method, for subject 7 in Figure 4.7a and 4.7b, the slow STS motion is less stable than the fast STS motion (highlighted red in Table 4.18). In addition, for subject 7, the proposed metric shows that for both models the slow STS (Figure 4.9a) is more stable than the fast STS (Figure 4.9b), shown in green in Table 4.18. In addition, for subject 11 in Figure 4.8a and 4.8b, the quasi-static method is less stable as the momentum-transfer method (highlighted red in Table 4.19). However, for subject 11, the proposed metric for both models correctly shows the quasi-static method (Figure 4.10c) as more stable than the momentum transfer method (Figure 4.10d), shown green in Table 4.19.

Method	Type	Slow > Fast		Stable > Momentum	
		Young	Older	Young	Older
Fujimoto	ROSv	6/10	4/5	9/10	4/5
	ROSa	6/10	2/5	4/10	0/5
Proposed	IPM	10/10	5/5	10/10	5/5
	DPM	10/10	5/5	10/10	5/5

Table 4.17: Summary of comparison of the various metrics for Slow vs Fast, Quasi-static vs Momentum-Transfer using the median values.

	Slow	Fast	Stable	Momentum
ROSv	0.55	0.71	0.67	0.22
ROSa	0.71	0.89	0.48	0.69
IPM	25.2	16.7	37.5	14.9
DPM	17.5	11.5	18.9	12.2

Table 4.18: Comparison of ROSv and ROSa vs the proposed method for subject ID 7. Expected results shown in green; unexpected results shown in red.

These results suggest that the proposed method can distinguish stable from unstable actions by characterizing the set of disturbances one can handle during standing. Specifically, the IPM and DPM models are able to accurate determine stable from unstable motions for all subjects.

	Slow	Fast	Stable	Momentum
ROSv	0.76	0.73	0.09	0.20
ROSa	0.82	0.84	0.16	0.57
IPM	39.8	21.1	45.9	14.6
DPM	23.5	20.1	28.2	26.3

Table 4.19: Comparison of ROSv and ROSa vs the proposed method for subject ID 11. Expected results shown in green; unexpected results shown in red.

Chapter 5

Conclusion

5.1 Conclusion

In this thesis, a personalized computational framework to model, identify and analyze the stability of an individual's STS motion by computing the basin of stability of the observed motion is described. To the author's best knowledge, this is the first framework to analytically compute an individual's BOS. The experimental analysis leads us to propose that the basin of stability of a locomotor pattern can be used to distinguish stable and unstable STS motions. Rather than reducing the STS motion to a single feature, the entire trajectory is analyzed to provide a more informative metric of stability. Where other methods fails, our proposed method successfully is able to show that the BOS of slow and quasi-static standing is large compared to fast and momentum-transfer standing.

In Chapter 2, we lay out the conceptual and implementable framework for this work. First we define notation and the hybrid system of interest. Then we describe how to synthesize a controller that tracks the observed human motion. Finally we present the problem to compute the BOS.

In Chapter 3, we delve deeper into the BOS computation. First we describe the theoretical background of occupations measures and present intuition for the method. Second we present the numerical implementation. We conclude with the BOS for 3 systems: rimless wheel, vehicle dynamics, and compass gait walker.

In Chapter 4, we verify the proposed framework on experimental data obtained via motion capture. First we describe the STS model used, the experimental protocol and the data collected from our sit to stand experiments. Second we present issues with the existing methods: ROSv and ROSa. Finally we present our BOS computation for two STS models and show that the proposed method successfully distinguishes stable from not-as-stable STS motions.

One question naturally arises: is it possible to simulate the volume of the BOS via direct simulation and not use the optimization problem defined in Chapter 3? While this is possible for systems with few states (i.e. IPM), direct simulation suffers from exponential scaling in the number of states. For example, for the DPM, a 2-link pendulum, a sparse simulation of the BOS consists of 175k randomly sampled points takes over 8 hours to compute. To simulate the BOS for a more representative human model such as a 3-link pendulum or higher would take days or weeks and is not practically feasible. While the optimization problem in Chapter 3 also suffers from exponential scaling with respect to the number of states, we are looking into ways to improve the optimization program itself.

By using modeling and dynamics to study human locomotor patterns, we can use numerical tools to compute basin of stability of locomotion without the need to perform extensive perturbation experiments. While there are many causes for falling, many of which are unrelated to perturbation response, this framework can help therapists identify those at-risk of falling due to muscle weakness by computing the subject's BOS while standing up. In addition, this framework can calculate the optimal trajectory or parameter change to increase one's BOS.

This framework may also be used to evaluate gait stability by quantifying the amount of

perturbation one can handle and continue walking, thereby opening new avenues to study the stability of human locomotion from a control-theoretic point of view.

5.2 Future Work

In this section, we describe the deficiencies of the current implementation and outline ideas for future work.

Improved Human Models

Here, we describe simple extensions to improve on the human modeling portion of this framework.

- The first step to improving the human model is to use an improved human skeletonization algorithm and to obtain accurate estimates of masses and inertias of each body segment. This thesis uses estimated limb segment masses from [92] and Recap [74], which utilizes a proprietary algorithm to determine the skeleton The framework would benefit by using work in [123] to obtain a more accurate skeleton and estimates of the limb masses and inertias. This would yield a more accurate human model and thus, more accurate stability results. As part of this work, more accurate torque bounds could be obtained also.
- The STS action is inherently an autonomous hybrid system with discrete mode 1 defined when the subject is sitting down and mode 2 when the subject is standing. Each state should be modeled differently: at minimum, state 1 modeled using a single inverted pendulum to model the torso and state 2 modeled using a triple inverted pendulum to model the entire body shown in Figure 5.1. This can be easily modeled with a hybrid system with the guard defined as the point where the vertical velocity of the hip joint is positive, indicating that the person's hip is raising off the chair, and analyzed with the stability algorithm presented in Chapter 3.

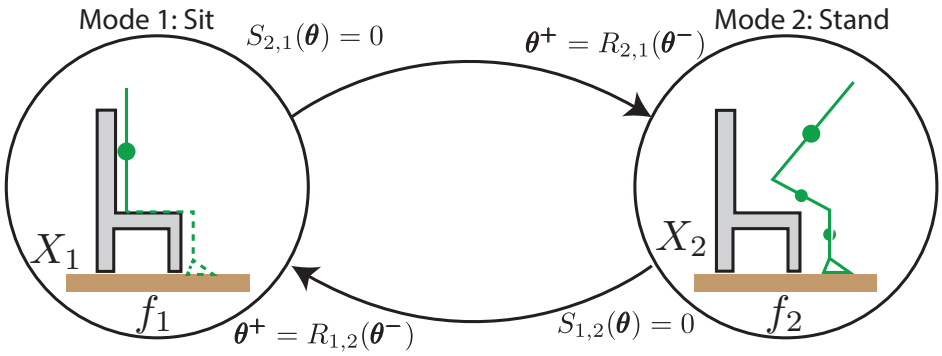

Figure 5.1: Hybrid Model for STS

- People don't stand up with their arms crossed. Rather, people usually either push off their legs using their arms to propel themselves up or hold onto arm rests to stand up. This system is inherently a closed chain with holonomic constraints. Additional work needs to be conducted to model the behavior of the arm and study its influence on stability.
- To bring this system out of the research environment and into clinics, the experimental setup needs to be inexpensive. Work needs to be done to study the accuracy and trade-offs of cheaper devices such as the Microsoft Kinect [76], accelerometers and the Nintendo Wii board [124][1].

Improved Control Synthesis

In this work, we assumed that individuals track a nominal trajectory with a PD controller. However, it is still has not been confirmed if this is indeed what people use. Future work involves synthesizing the controller that subjects use that is consistent with the various trials of the same STS motion. Currently the dataset has 5 trials of each STS motion which can be used to construct or verify a controller. Perturbation experiments would also need to be conducted to obtain trajectories which deviate from the nominal trajectory and for validation. Work from the computer graphics community to synthesize human-like controllers [125] may serve as an inspiration to develop these controllers.

Improved Reachable Set / Basin of Stability Calculations

At the moment, the limitation of the algorithm presented in Chapter 3 is a dynamical system with 8 states, 3 inputs, and degree 4 relaxation of the $v(t,x)$ and $w(x)$ polynomials. With a trigonometric system such as a 3-link pendulum, this quickly becomes infeasible as a 3-link pendulum requires with 6 states, or 12 states using standard trigonometric reductions, each with dynamics of degree 5. To study more complex systems, a more scalable approach needs to be developed to study STS and gait. Promising work by Jacobs [126] may serve as a good beginning for this work.

In addition, the current method enforces torque bounds manually by verifying that controller values in the BOS stay within input bounds. A more rigorous method of enforcing torque bounds in the dynamics would be to add the input as a state u with the dynamics of u governed by $\frac{\partial u}{\partial t}$. By adding the torque as a state, the torque becomes subject to domain restrictions.

$$\begin{aligned} \dot{x} &= f(t,x) + g(t,x)u_x \\ \dot{u}_x &= u(t) \end{aligned} \tag{5.1}$$

Finally, while the outer-approximation provides guarantees when the subject will definitely fall over, the inner-approximation provides guarantees when the subject will not fall

[1] In this thesis, Kinect data and accelerometry was also collected but not analyzed

over and is equally, if not more, useful. Occupation measures may also be used to compute the inner-approximation [35, 127]. In addition, for lower-dimensional systems, such as the single and 2-link pendulum, recent advances with the Hamilton-Jacobi formulation for decoupled systems may also be used [128].

Perturbation Experiments

To validate the BOS for human motion, perturbation experiments should be done. After computing the BOS for a subject, the subject should be called to a second experiment to test the subject's response to perturbations at different points in the STS trajectory. The IRB required for these types of experiment limits these experiments to labs with specialized harnesses and equipment for protection.

Intra-individual or Intra-cohort Comparisons

At the moment, the BOS of an individual's STS motion was compared to other actions from the same individual and not to other subjects and cross-cohort comparison was not done. To do individual-individual or cohort-cohort comparison, many more subjects would be required to conduct a thorough analysis on how and why the BOS varies between subjects and cohorts.

Comparisons to Other Sit-to-Stand Metrics

In order to gain acceptance by the clinical community, in addition to cheaper equipment, the BOS needs to be compared to existing STS metrics such as the BERG balance test, Timed Up and Go, and Stops Walking when Talking tests. To accomplish this, collaborations with rehabilitation centers and physical therapists need to be established to establish the relationship between existing metrics and the BOS.

Friction Analysis

Additional work could be done to study the effect of friction on STS. Using work in [35], the BOS can be computed over uncertain friction coefficients (μ_{fric}) and slip conditions, giving insight into how stable a subject's STS action is to floor conditions. This would require modeling the horizontal and vertical ground reaction forces ($f_{\text{grf},x}(\theta)$, $f_{\text{grf},y}(\theta)$) with slippage occurring when the horizontal ground reaction force exceeds the friction force. Figure 5.2 shows pictorial hybrid system definition of the model. The guard is mathematically defined as:

$$G(\theta) = \{(\theta, \dot{\theta}) \mid f_{\text{grf},x}(\theta) - \mu_{\text{fric}} f_{\text{grf},y}(\theta) > 0\} \tag{5.2}$$

with an identity reset map $R(\theta, \dot{\theta}) = [\theta; \dot{\theta}]$.

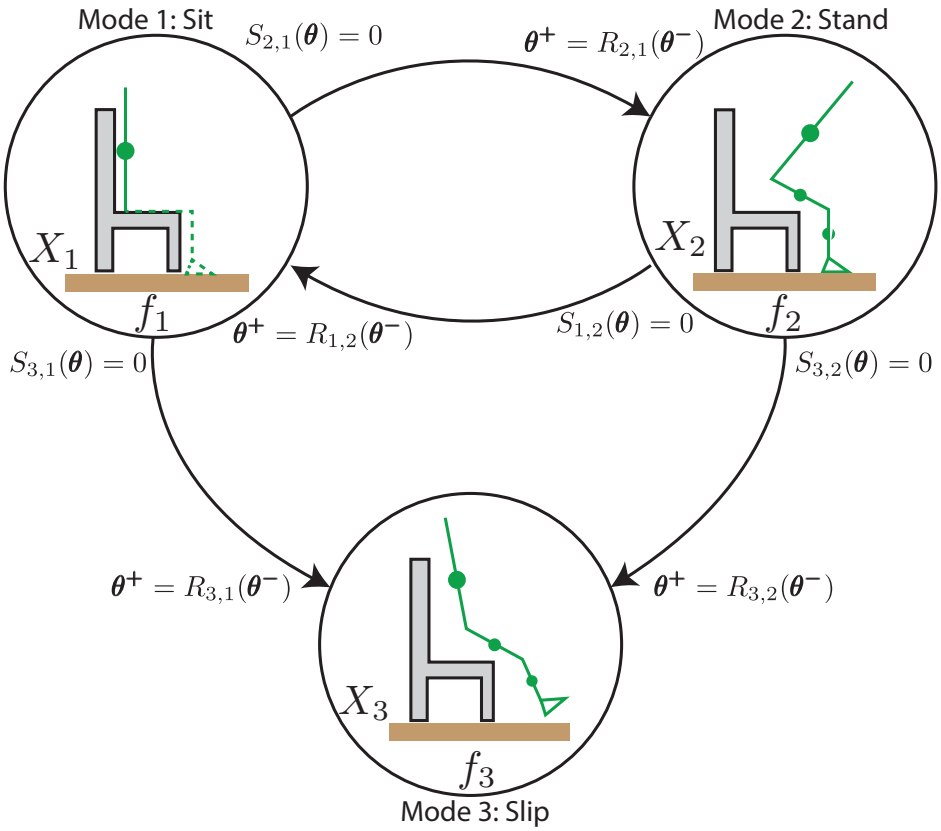

Figure 5.2: Hybrid Model for STS with Friction

Gait Analysis

The same framework and extensions presented in this thesis can be extended to studying the stability of one's gait. In fact, gait stability was the original impetus for this work. The first step is to develop a representative model for gait that includes ground contact constraints needs to be developed. As each individual's gait cycle may be different, the optimal control algorithm must be able to distinguish the discrete modes of an individual's gait cycle [82]. Because any meaningful gait model for the lower body includes 6+ states with trigonometric dynamics, work by Jacobs [126] or equivalent must be used to compute the BOS.

Robotics Applications

Finally, this framework is not limited to studying human motion. The BOS computation for human motion can be extended to studying the stability of exoskeletons, prosthetics or bipedal robots. Studying these systems may be simpler than studying human motion due to the deterministic nature of robots. In addition, this framework could be used to develop controllers to maximize the stability of the robot using work in [68].

5.3 Concluding Remarks

This thesis hopefully is only the start of bringing advances in dynamical systems and control theory to study the stability of human motion. While there is much work to be done and this thesis lays out several avenues to pursue, the path is by no means straight. However, if successful, this work could advance quantitative medicine, improving diagnostic capabilities for physicians and physical therapists, as well as improve controller design for robotic systems.

Bibliography

[1] US CDC. *Important Facts about Falls*.

[2] Administration on Aging. *Projections of Future Growth of the Older Population*.

[3] M C. Robertson. "Effectiveness and economic evaluation of a nurse delivered home exercise programme to prevent falls. 1: Randomised controlled trial". In: *BMJ* 322.7288 (Mar. 2001), pp. 697–697.

[4] Fay B Horak. "Postural orientation and equilibrium: what do we need to know about neural control of balance to prevent falls?" In: *Age and Ageing* 35 Suppl 2.suppl_2 (Sept. 2006), pp. ii7–ii11.

[5] Stephen R. Lord et al. "Differing Risk Factors for Falls in Nursing Home and Intermediate-Care Residents Who Can and Cannot Stand Unaided". In: *Journal of the American Geriatrics Society* 51.11 (Nov. 2003), pp. 1645–1650.

[6] Mary Tinetti. "Preventing Falls in Elderly Persons". In: *New England Journal of Medicine* 348 (2003), pp. 42–49.

[7] A.B. Zoss, H. Kazerooni, and A. Chu. "Biomechanical design of the Berkeley lower extremity exoskeleton (BLEEX)". In: *Transactions on Mechatronics* 11.2 (Apr. 2006), pp. 128–138.

[8] Elisabetta Papa and Aurelio Cappozzo. "Sit-to-stand motor strategies investigated in able-bodied young and elderly subjects". In: *Journal of Biomechanics* 33.9 (Sept. 2000), pp. 1113–1122.

[9] M. W. Rogers et al. "Step Training Improves the Speed of Voluntary Step Initiation in Aging". In: *The Journals of Gerontology Series A: Biological Sciences and Medical Sciences* 58.1 (Jan. 2003), pp. M46–M51.

[10] A.S. Pollock et al. "What is balance?" In: *Clinical Rehabilitation* 14.4 (Aug. 2000), pp. 402–406.

[11] Katherine Berg. "Measuring balance in the elderly: preliminary development of an instrument". en. In: *Physiotherapy Canada* 41.6 (Nov. 1989), pp. 304–311.

[12] Susan L Whitney et al. "Clinical Measurement of Sit-to-Stand Performance in People With Balance Disorders: Validity of Data for the Five-Times-Sit-to-Stand Test". In: *Physical Therapy* 85.10 (Oct. 2005), pp. 1034–1045.

[13] L Lundin-Olsson, L Nyberg, and Y Gustafson. “”Stops walking when talking” as a predictor of falls in elderly people.” In: *Lancet* 349.9052 (Mar. 1997), p. 617.

[14] Diane Podsiadlo and Sandra Richardson. “The Timed ”Up & Go”: A Test of Basic Functional Mobility for Frail Elderly Persons”. In: *Journal of the American Geriatrics Society* 39.2 (Feb. 1991), pp. 142–148.

[15] Lillemor Lundin-Olsson, Lars Nyberg, and Yngve Gustafson. “Attention, Frailty, and Falls: The Effect of a Manual Task on Basic Mobility”. In: *Journal of the American Geriatrics Society* 46.6 (June 1998), pp. 758–761.

[16] Yi-Chung Pai and James Patton. “Center of mass velocity-position predictions for balance control”. In: *Journal of Biomechanics* 30.4 (Apr. 1997), pp. 347–354.

[17] Elisabetta Papa and Aurelio Cappozzo. “A telescopic inverted-pendulum model of the musculo-skeletal system and its use for the analysis of the sit-to-stand motor task”. In: *Journal of Biomechanics* 32 (1999), pp. 1205–1212.

[18] James L Patton, Yi-Chung Pai, and Wynne A Lee. “Evaluation of a model that determines the stability limits of dynamic balance”. In: *Gait & Posture* 9.1 (Mar. 1999), pp. 38–49.

[19] Y-C Pai et al. “Role of feedforward control of movement stability in reducing slip-related balance loss and falls among older adults.” In: *Journal of Neurophysiology* 90.2 (Aug. 2003), pp. 755–62.

[20] Masahiro Fujimoto and Li Shan Chou. “Region of Stability Derived by Center of Mass Acceleration Better Identifies Individuals with Difficulty in Sit-to-Stand Movement”. In: *Annals of Biomedical Engineering* 42.4 (2013), pp. 1–9.

[21] Linda D Bogle Thorbahn and Roberta A Newton. “Use of the Berg Balance Test to Predict Falls in Elderly Persons”. In: *Physical Therapy* 76.6 (June 1996), pp. 576–583.

[22] Teresa M Steffen, Timothy A Hacker, and Louise Mollinger. “Age- and Gender-Related Test Performance in Community-Dwelling Elderly People: Six-Minute Walk Test, Berg Balance Scale, Timed Up & Go Test, and Gait Speeds”. In: *Physical Therapy* 82.2 (Feb. 2002), pp. 128–137.

[23] Susan W Muir et al. “Use of the Berg Balance Scale for predicting multiple falls in community-dwelling elderly people: a prospective study.” In: *Physical Therapy* 88.4 (Apr. 2008), pp. 449–59.

[24] Anne Shumway-Cook, Sandy Brauer, and Marjorie Woollacott. “Predicting the Probability for Falls in Community-Dwelling Older Adults Using the Timed Up & Go Test”. In: *Physical Therapy* 80.9 (Sept. 2000), pp. 896–903.

[25] A. M. Lyapunov. “The general problem of the stability of motion”. en. In: *International Journal of Control* 55.3 (Mar. 1992), pp. 531–534.

[26] Ufuk Topcu, Andrew Packard, and Peter Seiler. "Local stability analysis using simulations and sum-of-squares programming". In: *Automatica*. Vol. 44. 10. IEEE, 2008, pp. 2669–2675.

[27] Colas Le Guernic. *Reachability Analysis of Hybrid Systems with Linear Continuous Dynamics*. en. Oct. 2009.

[28] Goran Frehse, Colas Le Guernic, and A Donzé. "SpaceEx: Scalable verification of hybrid systems". In: *Computer Aided Verification* (2011), pp. 379–395.

[29] A.B. Kurzhanski and P. Varaiya. "On Ellipsoidal Techniques for Reachability Analysis. Part I: External Approximations". en. In: *Optimization Methods and Software* 17.2 (Jan. 2002), pp. 177–206.

[30] A.B. Kurzhanski and P. Varaiya. "Ellipsoidal techniques for reachability analysis: internal approximation". In: *Systems & Control Letters* 41.3 (Oct. 2000), pp. 201–211.

[31] S. Prajna. "Barrier certificates for nonlinear model validation". In: *42nd IEEE International Conference on Decision and Control (IEEE Cat. No.03CH37475)*. Vol. 3. IEEE, 2003, pp. 2884–2889.

[32] Ian Mitchell and Claire J Tomlin. "Overapproximating reachable sets by Hamilton-Jacobi projections". In: *Journal of Scientific Computing* 19 (2003), pp. 323–346.

[33] Ian M Mitchell, Alexandre M Bayen, and Claire J Tomlin. "A time-dependent Hamilton-Jacobi formulation of reachable sets for continuous dynamic games". In: *IEEE Transactions on Automatic Control* 50.7 (July 2005), pp. 947–957.

[34] Didier Henrion, Milan Korda, and Draft August. "Convex computation of the region of attraction of polynomial control systems". In: *IEEE Transactions on Automatic Control* 59.2 (2013), pp. 1–1.

[35] Shankar Mohan, Victor Shia, and Ram Vasudevan. "Convex Computation of the Reachable Set for Hybrid Systems with Parametric Uncertainty". In: (Jan. 2016), p. 25. arXiv: `1601.01019`.

[36] Pablo A. Parrilo. *Structured semidefinite programs and semialgebraic geometry methods in robustness and optimization*. May 2000.

[37] Antonis Papchristodoulou et al. "Robust Stability Analysis of Nonlinear Hybrid Systems". In: *IEEE Transactions on Automatic Control* 54.5 (May 2009), pp. 1035–1041.

[38] John N Maidens et al. "Lagrangian methods for approximating the viability kernel in high-dimensional systems". In: *Automatica* 49.7 (2013), pp. 2017–2029.

[39] Rajeev Alur et al. "Hybrid automata: An algorithmic approach to the specification and verification of hybrid systems". In: *Hybrid Systems*. Ed. by Robert L. Grossman et al. Vol. 736. Lecture Notes in Computer Science. Berlin, Heidelberg: Springer Berlin Heidelberg, 1993, pp 209–229.

[40] Panos J. Antsaklis, James A. Stiver, and Michael Lemmon. "Hybrid system modeling and autonomous control systems". In: *Hybrid Systems*. Ed. by Robert L. Grossman et al. Berlin, Heidelberg: Springer Berlin Heidelberg, 1993, pp 366–392.

[41] Anil Aswani et al. "Energy-Efficient Building HVAC Control Using Hybrid System LBMPC". In: (Apr. 2012). arXiv: `1204.4717`.

[42] C. Tomlin, G.J. Pappas, and S. Sastry. "Conflict resolution for air traffic management: a study in multiagent hybrid systems". In: *IEEE Transactions on Automatic Control* 43.4 (Apr. 1998), pp. 509–521.

[43] C.J. Tomlin, J. Lygeros, and S. Shankar Sastry. "A game theoretic approach to controller design for hybrid systems". In: *Proceedings of the IEEE* 88.7 (July 2000), pp. 949–970.

[44] Anouck R. Girard and J. Karl Hedrick. "Formation control of multiple vehicles using dynamic surface control and hybrid systems". en. In: *International Journal of Control* 76.9-10 (Jan. 2003), pp. 913–923.

[45] Francesco Borrelli. *Constrained Optimal Control of Linear and Hybrid Systems*. Springer, 2003, p. 206.

[46] Francesco Borrelli et al. "Dynamic programming for constrained optimal control of discrete-time linear hybrid systems". In: *Automatica* 41.10 (Oct. 2005), pp. 1709–1721.

[47] E.R. Westervelt, J.W. Grizzle, and D.E. Koditschek. "Hybrid zero dynamics of planar biped walkers". In: *IEEE Transactions on Automatic Control* 48.1 (Jan. 2003), pp. 42–56.

[48] B. Morris and J.W. Grizzle. "Hybrid Invariant Manifolds in Systems With Impulse Effects With Application to Periodic Locomotion in Bipedal Robots". In: *IEEE Transactions on Automatic Control* 54.8 (Aug. 2009), pp. 1751–1764.

[49] John Lygeros, Claire Tomlin, and Shankar Sastry. *Hybrid Systems and Control*.

[50] M.S. Branicky. "Stability of switched and hybrid systems". In: *Proceedings of 1994 33rd IEEE Conference on Decision and Control*. Vol. 4. IEEE, 1994, pp. 3498–3503.

[51] Michael S Branicky. "Stability of Hybrid Systems : State of the Art". In: *IEEE Conference on Decision and Control*. December. 1997, pp. 120–125.

[52] D. Liberzon and A.S. Morse. "Basic problems in stability and design of switched systems". In: *IEEE Control Systems Magazine* 19.5 (1999), pp. 59–70.

[53] Anthony N Michel and Bo Hu. "Towards a stability theory of general hybrid dynamical systems". In: *Automatica* 35.May 1998 (1999), pp. 371–384.

[54] John Lygeros et al. "Continuity and invariance in hybrid automata". In: *Proceedings of the 40th IEEE Conference on Decision and Control*. Vol. 1. IEEE, 2001, pp. 340–345.

[55] John Lygeros et al. "Dynamical properties of hybrid automata". In: *IEEE Transactions on Automatic Control* 48.1 (Jan. 2003), pp. 2–17.

[56] Robert Shorten et al. "Stability Criteria for Switched and Hybrid Systems". In: *SIAM Review* 49.4 (Jan. 2007), pp. 545–592.

[57] Hai Lin and Panos J. Antsaklis. "Stability and Stabilizability of Switched Linear Systems: A Survey of Recent Results". In: *IEEE Transactions on Automatic Control* 54.2 (Feb. 2009), pp. 308–322.

[58] R. Goebel, R.G. Sanfelice, and A. Teel. "Hybrid dynamical systems". In: *IEEE Control Systems* 29.2 (Apr. 2009), pp. 28–93.

[59] Rafal Goebel, Ricardo G. Sanfelice, and Andrew R. Teel. *Hybrid Dynamical Systems: Modeling, Stability, and Robustness*. Princeton University Press, 2012, p. 232.

[60] S. Prajna and A. Papachristodoulou. "Analysis of switched and hybrid systems - beyond piecewise quadratic methods". In: *Proceedings of the 2003 American Control Conference, 2003.* Vol. 4. IEEE, 2003, pp. 2779–2784.

[61] Amir Ali Ahmadi and Pablo A. Parrilo. "Non-monotonic Lyapunov functions for stability of discrete time nonlinear and switched systems". In: *2008 47th IEEE Conference on Decision and Control*. IEEE, 2008, pp. 614–621.

[62] Ian R. Manchester et al. "Regions of attraction for hybrid limit cycles of walking robots". In: *Arxiv preprint arXiv:1010.2247*. 2010, pp. 1–8. arXiv: `arXiv:1010.2247v1`.

[63] Victor Shia et al. "Relaxing Global Decrescence Conditions for Hybrid Systems Using SOS". 2014.

[64] Colas Le Guernic and Antoine Girard. "Reachability Analysis of Hybrid Systems Using Support Functions". In: *Computer Aided Verification* 5643 (2009), pp. 540–554.

[65] Alex Kurzhanskiy and Pravin Varaiya. "Ellipsoidal Techniques for Hybrid Dynamics: the Reachability Problem". In: *New Directions and Applications in Control Theory*. Ed. by Wijesuriya Dayawansa, Anders Lindquist, and Yishao Zhou. Vol. 321. Lect. Notes Control. Berlin/Heidelberg: Springer-Verlag, 2005, pp 193–205.

[66] Stephen Prajna, Ali Jadbabaie, and George J Pappas. "A Framework for Worst-Case and Stochastic Safety Verification Using Barrier Certificates". In: *IEEE Transactions on Automatic Control* 52.8 (2007), pp. 1415–1428.

[67] Kostas Margellos and John Lygeros. "Hamilton-Jacobi Formulation for Reach-Avoid Differential Games". In: *IEEE Transactions on Automatic Control* 56.8 (Aug. 2011), pp. 1849–1861.

[68] Anirudha Majumdar et al. "Convex Optimization of Nonlinear Feedback Controllers via Occupation Measures". In: *The International Journal of Robotics Research* 33.9 (June 2014), pp. 1209–1230.

[69] Victor Shia et al. "Convex Computation of the Reachable Set for Controlled Polynomial Hybrid Systems". In: *IEEE Conference on Decision and Control*. 2014.

[70] Gerald Folland. *Real Analysis: Modern Techniques and Their Applications*. Wiley, 1999, p. 408.

[71] Robert Full and Daniel E Koditschek. "Templates and anchors: neuromechanical hypotheses of legged locomotion on land". In: *Journal of Experimental Biology* 202.23 (Dec. 1999), pp. 3325–3332.

[72] Scott L Delp et al. "OpenSim: open-source software to create and analyze dynamic simulations of movement." In: *IEEE Transactions on Biomedical Engineering* 54.11 (Nov. 2007), pp. 1940–50.

[73] J P Aubin and H Frankowska. *Set-Valued Analysis*. Birkhauser Boston, 2008.

[74] PhaseSpace. *Recap2 User's Guide*. Tech. rep. PhaseSpace, 2010.

[75] Natural Point. *OptiTrack API*. Tech. rep. 2010.

[76] Zhengyou Zhang. "Microsoft Kinect Sensor and Its Effect". English. In: *IEEE Multimedia* 19.2 (Feb. 2012), pp. 4–10.

[77] Bart Koopman, Henk J. Grootenboer, and Henk J. de Jongh. "An inverse dynamics model for the analysis, reconstruction and prediction of bipedal walking". In: *Journal of Biomechanics* 28.11 (Nov. 1995), pp. 1369–1376.

[78] Donald E. Kirk. *Optimal Control Theory: An Introduction*. Courier Corporation, 2012, p. 464.

[79] C. R. Hargraves and S. W. Paris. "Direct trajectory optimization using nonlinear programming and collocation". en. In: *Journal of Guidance, Control, and Dynamics* 10.4 (July 1987), pp. 338–342.

[80] S. Hedlund and A. Rantzer. "Optimal control of hybrid systems". English. In: *Proceedings of the 38th IEEE Conference on Decision and Control (Cat. No.99CH36304)*. Vol. 4. IEEE, 1999, pp. 3972–3977.

[81] M. Shahid Shaikh and Peter E. Caines. "On the Hybrid Optimal Control Problem: Theory and Algorithms". In: *IEEE Transactions on Automatic Control* 52.9 (Sept. 2007), pp. 1587–1603.

[82] Ramanarayan Vasudevan et al. "Consistent Approximations for the Optimal Control of Constrained Switched Systems—Part 2: An Implementable Algorithm". en. In: *SIAM Journal on Control and Optimization* 51.6 (Jan. 2013), pp. 4484–4503.

[83] T Flash and N Hogan. "The coordination of arm movements: an experimentally confirmed mathematical model." In: *The Journal of Neuroscience* 5.7 (July 1985), pp. 1688–703.

[84] Y. Uno, M. Kawato, and R. Suzuki. "Formation and control of optimal trajectory in human multijoint arm movement". In: *Biological Cybernetics* 61.2 (June 1989).

[85] Mitsuo Kawato. "Internal models for motor control and trajectory planning". In: *Current Opinion in Neurobiology* 9.6 (Dec. 1999), pp. 718–727.

[86] Emanuel Todorov and Michael I Jordan. "Optimal feedback control as a theory of motor coordination." In: *Nature Neuroscience* 5.11 (Nov. 2002), pp. 1226–35.

[87] Joseph P Cusumano and Jonathan B Dingwell. "Movement variability near goal equivalent manifolds: fluctuations, control, and model-based analysis." In: *Human movement science* 32.5 (Oct. 2013), pp. 899–923.

[88] Dan Liu and Emanuel Todorov. "Evidence for the flexible sensorimotor strategies predicted by optimal feedback control." In: *The Journal of Neuroscience* 27.35 (Aug. 2007), pp. 9354–68.

[89] Jonathan B Dingwell, Joby John, and Joseph P Cusumano. "Do humans optimally exploit redundancy to control step variability in walking?" In: *PLoS Computational Biology* 6.7 (Jan. 2010), e1000856.

[90] Jonathan B Dingwell, Rachel F Smallwood, and Joseph P Cusumano. "Trial-to-trial dynamics and learning in a generalized, redundant reaching task." In: *Journal of Neurophysiology* 109.1 (Jan. 2013), pp. 225–37.

[91] Masahiro Fujimoto and Li Shan Chou. "Dynamic balance control during sit-to-stand movement: An examination with the center of mass acceleration". In: *Journal of Biomechanics* 45.3 (2012), pp. 543–548.

[92] Michael J. Pavol, Tammy M. Owings, and Mark D. Grabiner. "Body segment inertial parameter estimation for the general population of older adults". In: *Journal of Biomechanics* 35.5 (May 2002), pp. 707–712.

[93] PhaseSpace. *Impulse X2*. Tech. rep.

[94] Oskar Von Stryk. "Numerical Solution of Optimal Control Problems by Direct Collocation". In: *Optimal Control*. Ed. by R. Bulirsch et al. Basel: Birkhäuser Basel, 1993, pp 129–143.

[95] Frank M. Callier and Charles A. Desoer. *Linear System Theory*. Springer New York, 1994, p. 509.

[96] Russ Tedrake et al. "LQR-trees: Feedback Motion Planning via Sums-of-Squares Verification". In: *The International Journal of Robotics Research* 29.8 (2010), pp. 1038–1052.

[97] A.B. Alexander B. Kurzhanski et al. "Ellipsoidal techniques for reachability analysis". In: *Hybrid Systems: Computation and Control*. Lecture Notes in Computer Science 41.3 (Oct. 2000). Ed. by Nancy Lynch and Bruce H. Krogh, pp. 202–214.

[98] Ashish Tiwari. "Approximate reachability for linear systems". In: *Hybrid Systems: Computation and Control*. Springer, 2003, pp. 514–525.

[99] Michael Posa, Mark Tobenkin, and Russ Tedrake. "Lyapunov analysis of rigid body systems with impacts and friction via sums-of-squares". In: *Proceedings of the 16th international conference on Hybrid systems: computation and control - HSCC '13*. ACM. New York, New York, USA: ACM Press, Apr. 2013, p. 63.

[100] Stephen Prajna and Ali Jadbabaie. "Safety Verification of Hybrid Systems Using Barrier Certificates". In: *Hybrid Systems: Computation and Control* (2004), pp. 477–492.

[101] V I Arnold. *Mathematical Methods of Classical Mechanics*. Vol. 60. Springer, 1989.

[102] David Heaver Fremlin. *Measure Theory*. Vol. 2. Torres Fremlin, 2000.

[103] E J Anderson and P Nash. *Linear Programming in Infinite-Dimensional Spaces: Theory and Applications*. Wiley, 1987.

[104] Jean-Bernard Lasserre. *Moments, Positive Polynomials and Their Applications*. Imperial College Press Optimization Series, 2009, p. 385.

[105] Maria Trnovská. "Strong Duality Conditions in Semidefinite Programming". In: *Journal of Electrical Engineering* 56 (2005), pp. 87–89.

[106] *SPOTLESS*.

[107] A.P.S. Mosek. *The MOSEK optimization software*.

[108] Michael J Coleman. "A stability study of a three-dimensional passive- dynamic model of human gait". PhD thesis. Cornell University, 1998.

[109] Rajesh Rajamani. "Vehicle Dynamics and Control, 1st ed." In: *Springer US* (Oct. 2005).

[110] Giovanni Palmieri et al. "A Robust Lateral Vehicle Dynamics Control". In: *International Symposium on Advanced Vehicle Control*. 2010.

[111] Ambarish Goswami, Benoit Thuilot, and Bernard Espiau. "A Study of the Passive Gait of a Compass-Like Biped Robot: Symmetry and Chaos". In: *The International Journal of Robotics Research* 17.12 (Dec. 1998), pp. 1282–1301.

[112] The MathWorks. *MATLAB: Optimization Toolbox User Guide*. Tech. rep. The MathWorks, Inc., 2015.

[113] Robert J Full et al. "Quantifying dynamic stability and maneuverability in legged locomotion." In: *Integrative and comparative biology* 42.1 (Feb. 2002), pp. 149–57.

[114] J C Spagna et al. "Distributed mechanical feedback in arthropods and robots simplifies control of rapid running on challenging terrain." en. In: *Bioinspiration & biomimetics* 2.1 (Mar. 2007), pp. 9–18.

[115] Brian E Maki and William E McIlroy. "The Role of Limb Movements in Maintaining Upright Stance: The "Change-in-Support" Strategy". In: *Physical Therapy* 77.5 (May 1997), pp. 488–507.

[116] P. Wand, A. Prochazka, and K.-H. Sontag. "Neuromuscular responses to gait perturbations in freely moving cats". In: *Experimental Brain Research* 38.1 (Jan. 1980).

[117] A L Hof, S M Vermerris, and W A Gjaltema. "Balance responses to lateral perturbations in human treadmill walking." In: *The Journal of Experimental Biology* 213.Pt 15 (Aug. 2010), pp. 2655–64.

[118] M A Hughes et al. "Chair rise strategies in the elderly." In: *Clinical Biomechanics* 9.3 (May 1994), pp. 187–92.

[119] R. Aissaoui and J. Dansereau. "Biomechanical analysis and modelling of sit to stand task: a literature review". In: *IEEE International Conference on Systems, Man, and Cybernetics* 1 (1999), pp. 141–146.

[120] F Bahrami et al. "Biomechanical analysis of sit-to-stand transfer in healthy and paraplegic subjects." In: *Clinical Biomechanics* 15.2 (Feb. 2000), pp. 123–133.

[121] Masaya Anan et al. "The Clarification of the Strategy during Sit-to-Stand Motion from the Standpoint of Mechanical Energy Transfer". In: *Journal of Physical Therapy Science* 24.3 (June 2012), pp. 231–236.

[122] Bruce Etnyre and David Q Thomas. "Event standardization of sit-to-stand movements." In: *Physical Therapy* 87 (2007), pp. 1651–1666.

[123] Robert Peter Matthew. "Individualized Human Modelling and Assistive Device Design". PhD thesis. University of California, Berkeley, 2016.

[124] Nintendo. "Wii Balance Board". 2008.

[125] Kai Ding et al. "Learning reduced-order feedback policies for motion skills". In: *Symposium on Computer Animation*. New York, New York, USA: ACM Press, Aug. 2015, pp. 83–92.

[126] Henry Jacobs and Ram Vasudevan. "Computing the Time Limited Backwards Reachable Set Using Half-Densities".

[127] Milan Korda, Didier Henrion, and CN Colin Jones. "Inner approximations of the region of attraction for polynomial dynamical systems". In: *arXiv preprint arXiv:1210.3184* (2012), pp. 1–35.

[128] Mo Chen and Claire J. Tomlin. "Exact and efficient Hamilton-Jacobi reachability for decoupled systems". In: *2015 54th IEEE Conference on Decision and Control (CDC)*. IEEE, Dec. 2015, pp. 1297–1303.